The University of Sheffield

Department of Chemical & Biological Engineering

Fluidized Bed:

Online Monitoring of the Particle Temperature

Feng Li

PhD Thesis

March 2020

<u>Under the supervision of:</u>

Prof. Agba Salman

Prof. Jim Litster

Acknowledgement

I would like to express my appreciation first to Prof. Agba Salman, Prof. Jim Litster, and Prof. Mike Hounslow for their support and guidance. I am also deeply grateful that my parents and Miss Yan Zhou supported and helped me a lot.

Feng Li

Abstract

In a fluidized bed, the online temperature of the particles is important for monitoring the process and for monitoring the process and understanding the heat transfer mechanisms. In order to minimize the influence of the air on the particle temperature measurement, thermal cameras were recently used to determine the particle temperature non-invasively.

When using a thermal camera to monitor the particles in a fluidized bed, especially in an ordinary fluidized bed, it is expected that some the particles in the thermal images will be blurry. The blurry particles can be caused by the particle movement and the thermal camera focus. In order to measure the particle temperature accurately, the clear particles and the blurry particles in the thermal images should be considered separately. In this thesis, based on the calibrated particle size and shape, only the pixels that represent the clear particles in the thermal images were identified and correlated to the particle temperature.

Using this technique, the online temperature of the particles was measured together with the temperatures of the air and the fluidized bed wall. It was found that higher inlet air velocity and higher loaded particle mass can accelerate the heating process of the particles more than the heating process of the fluidized bed wall.

At the temperature steady state, a two-compartment model was developed to correlate the heat transfer coefficients between the air and the particles and between the particles and the fluidized bed wall. It was found that the relationship between them depends on how the void fraction and the particle Reynolds number are related to the contact area between the particle and the zones (hot and cold) and the time that the particle spent in the zones.

Table of Contents

List of Figures

List of Symbols

A	Area of the pixel cluster	$(pixels)$
A_{ap}	Contact area between the air and the particles	(m^2)
A_{as}	Contact area between the air and the solid surface	(m^2)
A_{bed}	Fluidized bed wall area	(m^2)
A_C^*	Heat transfer area between the cold zone and the particle	(m^2)
A_H^*	Heat transfer area between the hot zone and the particle	(m^2)
A_{in}	Cross-sectional area of fluidized bed air distributor	(m^2)
A_{lost}	Outside surface area of the fluidized bed wall	(m^2)
A_{max}	Maximum area of the pixel cluster	$(pixels)$
A_{min}	Minimum area of the pixel cluster	$(pixels)$
Ar	Archimedes number $Ar = \frac{\rho_a(\rho_p - \rho_a)gD^3}{\mu^2}$	$(-)$
C	Circularity of the pixel cluster $C = 4\pi A/P^2$	$(-)$
c_1	A constant, 3.7418×10^8	$(-)$
c_2	A constant, 14387.9	$(-)$
C_D	Drag coefficient	$(-)$
C_{max}	Maximum circularity of a pixel cluster	$(-)$
C_{min}	Minimum circularity of a pixel cluster	$(-)$
$C_{p,a}$	Specific heat capacity of air	$(J/kg \cdot K)$
$C_{p,p}$	Specific heat capacity of particle	$(J/kg \cdot K)$
$C_{p,w}$	Specific heat capacity of fluidized bed wall	$(J/kg \cdot K)$
D	Particle diameter	(m)
D^*	$D^* = D\left[\frac{\rho_a(\rho_p - \rho_a)g}{\mu^2}\right]^{1/3}$	$(-)$
D_{max}	Maximum particle diameter	(m)

D_{mean}	Mean particle diameter	(m)
D_{min}	Minimum particle diameter	(m)
$E_b(T)$	Total radiation emitted from an object at a specific temperature	(W/m^2)
E_{input}	Total energy input from the air to particles and the fluidized bed wall	(J)
E_{lost}	Energy lost	(J)
E_p	Energy that increases the particle temperature	(J)
E_w	Energy that increases the fluidized bed wall temperature	(J)
F	Set of all pixels in an image	
$F_1, F_2, \dots, F_n$	Connected subsets of F	
$F_{define}(\ )$	A uniformity (homogeneity) predicate defined on groups of connected pixels	
$F_{particle}(\ )$	Definition of a particle in the thermal image that is defined on the pixel clusters $(F_1, F_2, \dots, F_n)$	
$e(\lambda)$	Emissivity at a wavelength λ and can vary in the range 0 to 1	$(-)$
g	gravitational acceleration	(m/s^2)
h_{as}	Heat transfer coefficient between air and solid material	$(W/m^2 \cdot K)$
h_{ap}	Heat transfer coefficient between air and the particles	$(W/m^2 \cdot K)$
H_{bed}	Bed height	(m)
h_{bw}	Heat transfer coefficient between the particle bed and the fluidized bed wall	$(W/m^2 \cdot K)$
h_C^*	Heat transfer coefficient between the cold zone and a particle	$(W/m^2 \cdot K)$
$H_{falling}$	Falling height of the particle in the unit of pixels	$(pixels)$
h_H^*	Heat transfer coefficient between the hot zone and a particle	$(W/m^2 \cdot K)$

$H_{image-distributor}$	Distance between the thermal image bottom and the fluidized bed bottom	(mm)
h_{lost}	Heat transfer coefficient between the fluidized bed wall and the ambient air	$(W/m^2 \cdot K)$
h_{pw}	Heat transfer coefficient between the particles and the fluidized bed wall	$(W/m^2 \cdot K)$
I	Thermal image visualized from a signal matrix	
$IFOV$	Instantaneous field of view	$(mrad)$
I_n	A grey value in the thermal image	
I_{otsu}	An optimal grey value obtained using the Otsu's threshold method	
I_{xy}	A pixel in the thermal image with coordinate (x, y) and colour value $I(x, y)$.	
I_{xy}^*	One of the pixels that represent the particles in the thermal image	
k	Any grey level in an image	
k^*	The threshold in the Otsu's thresholding method (Otsu, 1979)	
k_a	Thermal conductivity of air	$(W/m \cdot K)$
k_p	Thermal conductivity of particle	$(W/m \cdot K)$
k_s	Thermal conductivity of solid material	$(W/m \cdot K)$
k_w	Thermal conductivity of fluidized bed wall	
L	Distance between the focused plane and the lens	(mm)
l_{pixel}	Pixel size	(mm)
m_p^*	Mass of a particle	(kg)
m_p	Loaded particle mass	(kg)
m_w	Mass of fluidized bed wall	(kg)
N	Particle number	$(-)$
n_i	Number of the pixels with grey level i	
N_{img}	Total number of pixels in the image	

Nu_{ap}	Nusselt number for particles in air, $Nu_{ap} = \frac{h_{ap}D}{k_a}$	$(-)$
Nu_{bw}	Nusselt number for the particle bed contacted with the fluidized bed wall, $Nu_{bw} = \frac{h_{bw}D}{k_a}$	$(-)$
P	Perimeter of a pixel cluster	$(pixels)$
Δp	Pressure drop	(Pa)
p_i	Probability of the pixels with grey level i,	
Pr	Prandtl number $Pr = \frac{\mu C_{p,a}}{k_a}$	$(-)$
q_{ap}	Overall heat flux between the air and the particles	(W)
q_{cond}	Conduction heat flux per area	(W/m^2)
q_{conv}	Convection heat flux	(W)
q_{pw}	Overall heat flux from the particles to the fluidized bed wall	(W)
Re_p	Particle Reynolds number, $Re_p = \frac{UD\rho_a}{\mu}$	$(-)$
$Re_{p,mf}$	Particle Reynolds number at the incipient fluidization	$(-)$
S	A signal matrix obtained from the thermal camera	$(raw\ count)$
S_{max}	Maximum value in the signal matrix S	$(raw\ count)$
S_{min}	Minimum value in the signal matrix S	$(raw\ count)$
S_{xy}	An element in the signal matrix with coordinate (x,y) and signal value $S(x,y)$	$(raw\ count)$
S_{xy}^*	The element in the signal matrix that is corresponded to an identified pixel (I_{xy}^*)	$(raw\ count)$
t	Heating time	(s)
t_H	The residence time of a particle in the hot zone	(s)
t_C	The residence time of a particle in the cold zone	(s)
T	Temperature	(K)

T^*	Instantaneous particle temperature	(K)
T_a	Air temperature	(K)
$T_{amb.}$	Ambient temperature at the heating time t	(K)
T_{bg}	The temperature of the pixels representing the background used by Patil et al. (2015)	(K)
T_C	Temperature of the cold zone	(K)
T_{C1}^*	Temperature of a particle enters the cold zone	(K)
T_{C2}^*	Temperature of a particle leaves the cold zone	(K)
T_{cal}	Calibrated particle temperature	(K)
T_{ex}	Exit air temperature	(K)
T_g	The air temperature used by Brown and Lattimer (2013)	
T_H	Temperature of the hot zone	(K)
T_{H1}^*	Temperature of a particle enters the hot zone	(K)
T_{H2}^*	Temperature of a particle leaves the hot zone	(K)
T_{in}	Inlet air temperature	(K)
T_{uncal}	Uncalibrated particle temperature measured from the thermal camera	(K)
T_{thr}	Threshold used by Patil et al. (2015)	(K)
$\langle T_p \rangle_{pix}$	Mean temperature of the pixels representing the particles used by Patil et al. (2015)	(K)
$T_{p,s}$	The particle temperature used by Brown and Lattimer (2013)	(K)
T_p	Particle temperature	(K)
T_w	Fluidized bed wall temperature	(K)
T_{xy}^*	The temperature of the particle represented by (S_{xy}^*) in the signal matrix and (I_{xy}^*) in the thermal image	(K)
ΔT_{as}	Characteristic temperature difference between the air and the solid	(K)
ΔT_{ap}	Mean temperature difference between the air and the particles	(K)

ΔT_{pw}	Mean temperature difference between the particles and the fluidized bed wall	(K)
$\dfrac{\Delta T_s}{dx}$	Temperature gradient through a solid material	(K/m)
U	Superficial air velocity	(m/s)
U_{in}	Inlet air velocity	(m/s)
U_{mc}	Maximum velocity required for the particles to be clear in the thermal image	(m/s)
U_{mf}	Minimum fluidization velocity	(m/s)
U_p	Particle velocity	(m/s)
U_t	Particle terminal velocity	(m/s)
U_t^*	$U_t^* = U_t \left[\dfrac{\rho_a^2}{\mu(\rho_p - \rho_a)g} \right]^{1/3}$	$(-)$
V_{bed}	Volume of the particle bed	(m^3)
$V_{particles}$	Volume of the loaded particles	(m^3)
$W(\lambda, T)$	Radiance for a wavelength λ in μm and a temperature T in Kelvin (K)	$(W \cdot m^{-2} \cdot sr^{-1} \cdot \mu m^{-1})$
(x, y)	Coordinate of a pixel in the thermal image, an element in the signal matrix, or a particle in the thermal camera detection area	
Z	Grey level in an image	

ε	Void fraction of the particle bed	$(-)$
ε_{mf}	Void fraction of the particle bed at the incipient fluidization	$(-)$
η	Ratio between the heat transfer coefficient from the air to the particles and the heat transfer coefficient from the particles to the fluidized bed wall, $\eta = \frac{h_{ap}}{h_{bw}}$	$(-)$
θ	Dimensionless, $\theta = \frac{T_p - T_w}{T_a - T_w}$	$(-)$
θ_{gp}	A dimensionless term introduced by Brown and Lattimer (2013), $\theta_{gp} = \frac{T - min(T_{p,s}, T_g)}{max(T_{p,s}, T_g) - min(T_{p,s}, T_g)}$	
κ_A	Ratio of the contact areas between the particle and the hot zone, and between the particle and the cold zone	
κ_t	Ratio of the residence times for a particle in the hot zone and in the cold zone	
κ_h	Ratio of the heat transfer coefficients between the particle and the hot zone, and between the particle and the cold zone	
μ	Viscosity of air	$(Pa \cdot s)$
$\mu_1(k)$	Class mean grey level of the pixels in the grey level class $[1, 2, \ldots, k]$	
$\mu_2(k)$	Class mean grey level of the pixels in the grey level class $[k+1, k+2, \ldots, Z]$	
ξ	A defined item, $\xi = \frac{\ln\left(\frac{T_{H2}^* - T_H}{T_{H1}^* - T_H}\right)}{\ln\left(\frac{T_{C2}^* - T_C}{T_{C1}^* - T_C}\right)}$	
ρ_a	Density of air	(kg/m^3)
ρ_p	Density of particles	(kg/m^3)
ρ_w	Density of the fluidized bed wall	(kg/m^3)
σ	Stefan-Boltzmann constant, $\sigma = 5.670 \times 10^{-8}$	$(W/m^2 \cdot K^4)$
$\sigma_B^2(k)$	A between-class variance evaluate the goodness of the grey value k as a threshold (Otsu, 1979)	
λ_{max}	Peak wavelength of the spectral blackbody emissive power distribution	$(J/kg \cdot K)$

ϕ_s	Sphericity of the particles	$(-)$
$\omega_1(k)$	Sum of the probability distribution of the pixels in the grey level class $[1, 2, \ldots, k]$	
$\omega_2(k)$	Sum of the probability distribution of the pixels in the grey level class $[k + 1, k + 2, \ldots, Z]$	

1 Introduction

1.1 Background of the thesis

Fluidized bed is a device that has air continuously introduced and allows the solid particles within it to move like a fluid. It is widely used in many industries for different applications including drying, coating and granulation, due to its favourable heat transfer characteristics.

The fluidization behaviour of the particles is dependent on their density and size and is indicated by the pressure drop. In order to fluidize the particles and allow the particles to circulate, the air velocity should be higher than the minimum fluidization velocity and lower than the particle terminal velocity.

When hot air is introduced from the bottom of the fluidized bed, both the particles and fluidized bed wall are heated. The online temperatures of the air, the particles and the fluidized bed wall are important for monitoring the heating process and understanding the heat transfer mechanisms.

In the past, temperature probes were widely used by researchers to measure the particle temperature in ordinary (e.g. column, tube, cylindrical) fluidized beds. Generally, when the measured position was closer to the top of the fluidized bed or closer to the fluidized bed wall, the measured temperature was decreased (Malek & Lu, 1964).

The concept of temperature probes can be expressed as:

$$T = f(Z) \hspace{4cm} \text{Eq. (1)}$$

Where T represents the measured temperature, and Z represents the signal given by the temperature probes.

The main advantage of temperature probes is that the correlation between the device signal and the measured temperature can be obtained easily. The main disadvantage is that direct contact between the temperature probes and the particles is required, while the contact between the temperature probes and the air surround the particles cannot be prevented.

From the Planck's law, it is known that the radiation (including gamma rays, x-rays, ultraviolet, visible, infrared, and microwaves) emitted from an object is correlated to its temperature. Therefore, the temperature of a particle can be determined non-invasively from its emitted radiation.

Thermal camera is a device that can receive the infrared radiation emitted from its detection area and generate a signal matrix to represent the intensity of the received infrared radiation. It is a system mainly composed of a lens, an infrared sensor and a digital signal processor. As shown in Figure 1, there are several steps involved in taking a temperature measurement with a thermal camera.
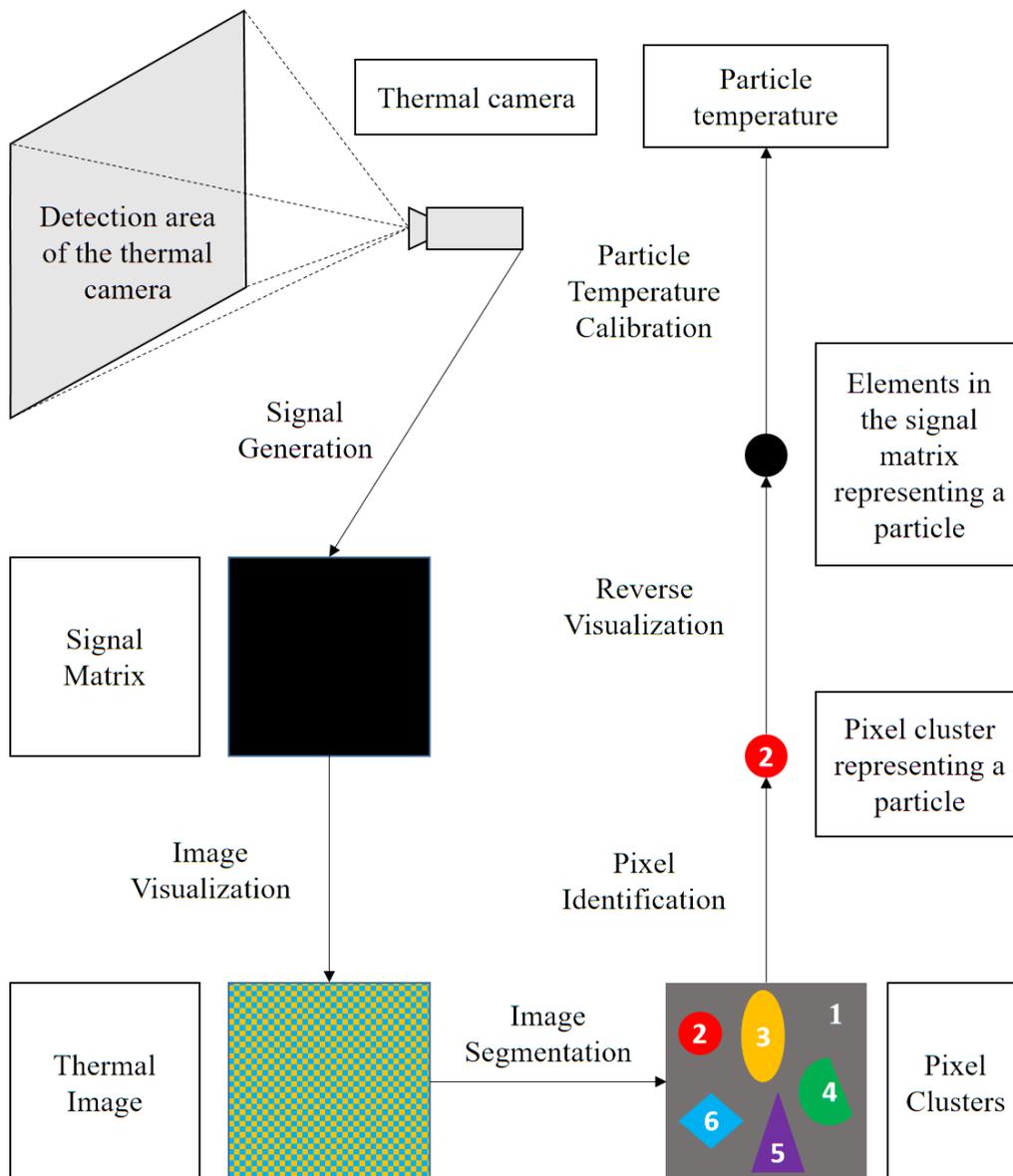
Figure 1. Temperature measurement using a thermal camera.

When a thermal camera receives infrared radiation from its detection area, it generates an array of signal values (signal matrix). For display, the signal matrix can be visualized as a thermal image. The thermal image could be a grey scale image (the colour of a pixel is represented by a grey value and varied from 0 to 255, where 0 is the black and 255 is the white), a RGB image (the colour of a pixel is represented by red, green and blue values and respectively varied from 0 to 255, where (0, 0, 0) is the black and (255, 255, 255) is the white) or an image in other formats. This process is unlikely to introduce error in the temperature measurement of the fluidizing particles.

From the visualized thermal image, the particles that were within the detection area of the thermal camera can be observed. However, observation cannot be used scientifically to identify the pixels that represent the particles. Image segmentation is a technique that can divide an image into multiple segments (also known as sets of pixels, pixel clusters, image objects and etc.). In an image, pixels in the same pixel segment (pixel set, pixel cluster, image object and etc.) are connected to each other in eight directions (up, down, left, right, up-left, up-right, down-left and down-right). Sometimes, the connected directions can be simplified as four directions (up, down, left and right). Unconnected pixels belong to different pixel segments. For example, the pixel clusters 1-6 are segmented in Figure 1.

In a fluidized bed, both the particles and the fluidized bed wall are in the detection area. If an inappropriate image segmentation is used, the pixels representing the particles and the pixels representing the fluidized bed wall could be divided within the same connected subsets (pixel cluster). This process is likely to introduce error in the particle temperature measurement.

Based on the segmented pixel clusters, if the definition of a particle in the thermal image is given, then the pixel cluster that satisfies the definition (for example, the pixel clusters 2 in Figure 1) can be identified as a particle. The pixels within the identified pixels clusters are representing the particles in the thermal image. In this thesis, this process is referred as the pixel identification.

It should be noticed that (Pal & Pal, 1993): "hundreds of image segmentation techniques are presented in the literature, but there is no single method which can be considered good for all images, nor are all methods equally good for a particular type of image". If an inappropriate particle definition is used, the number of pixels

14

representing the particle may be more or less than it should be. This process is likely to introduce error in the particle temperature measurement.

By reversing the visualization function, the element in the signal matrix that is corresponded to an identified pixel can be obtained. These elements are representing the particles in the signal matrix and can be correlated to the particle temperature (referred as the particle temperature calibration in Figure 1).

The correlation function can be affected by the relationship between the infrared radiation emitted from the particles and received by the thermal camera, the relationship between the infrared radiation received by the thermal camera and the generated signal matrix by the infrared sensor, and the quality of the image segmentation.

In summary, in order to use a thermal camera to online monitor the particle temperature in a fluidized bed accurately, the general steps are:

i.   Install the thermal camera and visualize the signal matrices into thermal images. The factors that need to be concerned are the specification of the thermal camera, the material of the window used on the fluidized bed and the focus plane of the thermal camera;

ii.   Segment the thermal images into pixel clusters, identify the pixel clusters that represent the particles. The factors that need to be concerned are the stability of the identification technique, and the uniformity of the relationship between the identified pixels and the particle temperature;

iii. Obtain the signal values of the elements in the signal matrices that represent the particles and correlate them to the particle temperature. The factors that need to be concerned are the influence of the hot air, and the accuracy of the particle temperature measured for calibration.

Recently, several researchers used thermal cameras successfully to measure the particle temperature non-invasively in flat fluidized beds (referred as a pseudo-2D fluidized bed, in comparison, an ordinary fluidized bed is referred as a 3D fluidized bed). The main advantages of a flat fluidized bed is that due to the restriction of the fluidized bed wall, all particles can be assumed to move in the same plane and can be continuously focused by the thermal camera.

However, most of the fluidized beds used in industries are ordinary 3D fluidized beds. Compared to the 2D fluidized bed, the contacts between the air and the particles, and between the particles and the fluidized bed wall are different in the ordinary 3D fluidized beds. In these fluidized beds, because the particles can move in three directions, not all particles can be focused by a thermal camera. It is expected that there will be many unfocused particles in the thermal images. Therefore, the effect of the thermal camera focus on the temperature measurement of the particles needs to be considered.

During the heating process of the particles, heat transfer occurs between the air and the particles, between the air and the fluidized bed wall, and between the particles and the fluidized bed wall. The order of the air temperature, the particle temperature and the fluidized bed wall temperature indicates the directions of the heat transfer processes. The trends of the temperature differences between the air and the particles, between the air and the fluidized bed wall, and between the particles and the fluidized bed indicate the heat flux between them during the heat transfer processes.

In the operation of a fluidized bed, inlet air velocity, inlet air temperature and loaded particle mass can affect the heat transfer processes between the air and the particles, between the air and the fluidized bed wall, and between the particles and the fluidized bed wall. In terms of the heat transfer coefficients for the above heat transfer processes, there are many empirical models in the literature can be used.

However, those models are mainly addressing the heat transfer process between the air and the particles, or between the particles and the fluidized bed wall. Also, limited by the particle temperature measurement technique, the relationship between the heat transfer coefficients for the two processes are not established. In applications, researchers tend to empirically select a heat transfer coefficient for one of the heat transfer processes and fitting the heat transfer coefficient for the other. Because both of the heat transfer processes are affected by the particle fluidization, it is proposed in this thesis that the heat transfer coefficient between the air and the particles, and between the particles and the fluidized bed wall are correlated and can be addressed simultaneously.

When the particle temperature does not change over time, a temperature steady state of the particles is reached. At this state, the total heat flux from the air to the particles

is equal to the total heat flux from the particles to the fluidized bed wall. By measuring the temperature difference between the air and the particles and between the particles and the fluidized bed wall, the overall heat transfer coefficients between the air and the particles, and between the particles and the fluidized bed wall can be compared.

In this thesis, at the temperature steady state, a particle is considered to gain heat from somewhere that has higher temperature than it and lose the same amount of heat to somewhere that has lower temperature than it (as shown in Figure 2). The zone has temperature higher than the particle is referred as the hot zone and the zone has temperature lower than the particle is referred as the cold zone.
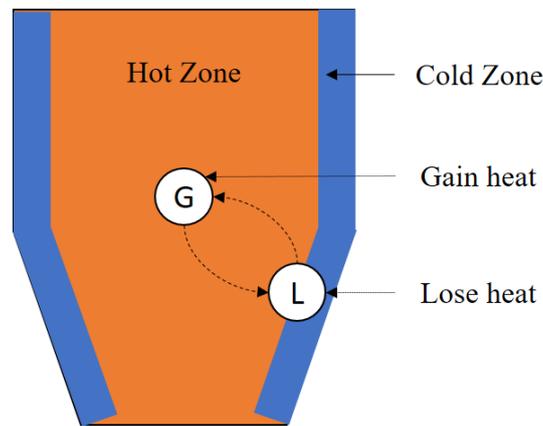
Figure 2. Two-compartment model.

Based on this, a two-compartment model (hot zone and cold zone) can be developed to describe the heat transfer process of a particle. The heat transfer process in each zone can be described by the heat transfer coefficient, the contact area between the zone and the particle, and the time that the particle spent in the zone. For simplification, the hot zone is set as the area where a particle is in full contact with the hot air, and the cold zone is set as the area where a particle is in contact with the fluidized bed wall. By experimentally measuring the temperature difference between the particles and the air, and between the particles and the fluidized bed wall, a balance equation between the heat gained and lost by the particle can be obtained.

1.2   Aims of the thesis

Due to the complexity of the temperature measurement using thermal cameras, the primary aim of this thesis is to establish a method that can reliably measure the online temperature of the particles in a 3D fluidized bed.

Using this method, the second aim of this thesis is to investigate the effect of the inlet air velocity, the inlet air temperature and the loaded particle mass on the particle temperature during the particle heating process.

Based on the online measured particle temperature, the third aim of this thesis is to compare the heat transfer coefficient between the air and the particles and between the particles and the fluidized bed wall.

1.3   Structure of the thesis

In chapter 2, the literature related to the topics in this thesis is reviewed. In Chapter 3, the factors that are relevant to the installation of the thermal camera are considered. An experimental setup was designed to minimize the measurement error caused by the installation. In Chapter 4, the factors that are relevant to the identification of the pixels representing the particles in the thermal images are considered. An identification procedure was developed to improve the measurement accuracy. In Chapter 5, the factors that are relevant to the correlation between the identified pixels and the particle temperature are considered. Three correlation methods were compared and the optimum results were used. In Chapter 6, during the particle heating process, the online particle temperature was monitored using a thermal camera. In the meanwhile, the online temperatures of the inlet air, the exit air, the fluidized bed wall and the ambient of the fluidized bed were recorded using thermocouple probes. In Chapter 7, the heat transfer coefficient between the air and the particles and the heat transfer coefficient between the particles and the fluidized bed wall were compared at the particle temperature steady state. A two-compartment model is developed.

2 Literature Review

2.1 Scope of review

The fluidization behaviour of the particles is relevant to the density and size of the particles. The Geldart classification (Geldart, 1973) is widely used to indicate the relationship between the particle type and its fluidization behaviour. In a fluidized bed, pressure drop is an important indication of the particle fluidization state (Ergun, 1952; Kunii & Levenspiel, 1991; Rhodes, 2008). The inlet air velocity should be higher than the minimum fluidization velocity (Chitester, Kornosky, Fan, & Danko, 1984; Kunii & Levenspiel, 1991; Wen & Yu, 1966) and lower than the particle terminal velocity (Haider & Levenspiel, 1989; Kunii & Levenspiel, 1991; Turton & Clark, 1987).

This chapter first reviewed the fundamental knowledge of the particle fluidization.

The particle temperature in a fluidized bed can be measured by temperature probes (Baeyens & Goossens, 1973; Borodulya, Teplitsky, Markevich, Hassan, & Yeryomenko, 1991; Gunn & De Souza, 1974; Gunn & Khalid, 1975; Malek & Lu, 1964; Petrovic, Thodos, & Illinois, 1968; Valenzuela & Glicksman, 1984; van Heerden, Nobel, & van Krevelen, 1953; Wadke, Hounslow, & Salman, 2005) and thermal cameras (Brown & Lattimer, 2013; Li et al., 2017; A. V. Patil, Peters, Sutkar, Deen, & Kuipers, 2015; Sutkar et al., 2015; Tsuji, Miyauchi, Oh, & Tanaka, 2010). Both of them have advantages and disadvantages. Compared to temperature probes, thermal cameras are more suitable for online monitoring of the particle temperature in a fluidized bed.

This chapter then reviewed the concepts of the temperature probes and the thermal cameras.

When a thermal camera is used to measure the particle temperature in a fluidized bed, the thermal image usually contains both the particles and the fluidized bed wall. It is first necessary to distinguish between pixels that represent particles and pixels that represent the fluidized bed wall. The process that divides an image into multiple segments is the image segmentation. In the literature, the fluidized beds that were online monitored using thermal cameras were flat fluidized beds (Brown & Lattimer,

2013; Li et al., 2017; A. V. Patil, Peters, Sutkar, et al., 2015; Sutkar et al., 2015; Tsuji et al., 2010).

This chapter also reviewed the image segmentation techniques briefly and the methods used by the researchers for obtaining the particle temperature.

However, most of the fluidized beds that were used to develop the empirical heat transfer models are ordinary (e.g. column, tube, cylindrical) 3D fluidized beds (Borodulya et al., 1991; Decker & Glicksman, 1983; Ganzha, Upadhyay, & Saxena, 1982; Gunn, 1978; Gunn & Khalid, 1975; Malek & Lu, 1964; Mickley & Fairbanks, 1955; Petrovic et al., 1968; Ranz & Marshall, 1952; Saxena & Ganzha, 1984; van Heerden et al., 1953; van Heerden, Nobel, & van Krevelen, 1951).

This chapter then reviewed the trend of the particle temperature and the widely used empirical heat transfer models.

2.2 Fundamental of particle fluidization

2.2.1 The Geldart classification

In order to describe the relationship between the fluidization behaviour and the properties of particles, the Geldart (1973) classification is generally used (as show in Figure 3). Based on the Geldart classification, the particle type can be described as (Litster & Ennis, 2004; Morl, Heinrich, & Peglow, 2007): Type A particles are usually with a mean particle size larger than $50\ \mu m$ and smaller than $200\ \mu m$, and with a density between 700 and $1400\ kg/m^3$. This type of particles can be easily fluidized and show some particulate expansion. Type B particles are usually with a mean particle size larger than $40\ \mu m$ and smaller than $500\ \mu m$, and with a density between 1400 and $4000\ kg/m^3$. This type of particles can also be fluidized easily but do not show any particulate expansion. Type C particles are usually with a mean particle size smaller than $50\ \mu m$. This type of particles are cohesive and fluidized poorly. Type D particles are relatively large and require higher air velocities for fluidization.
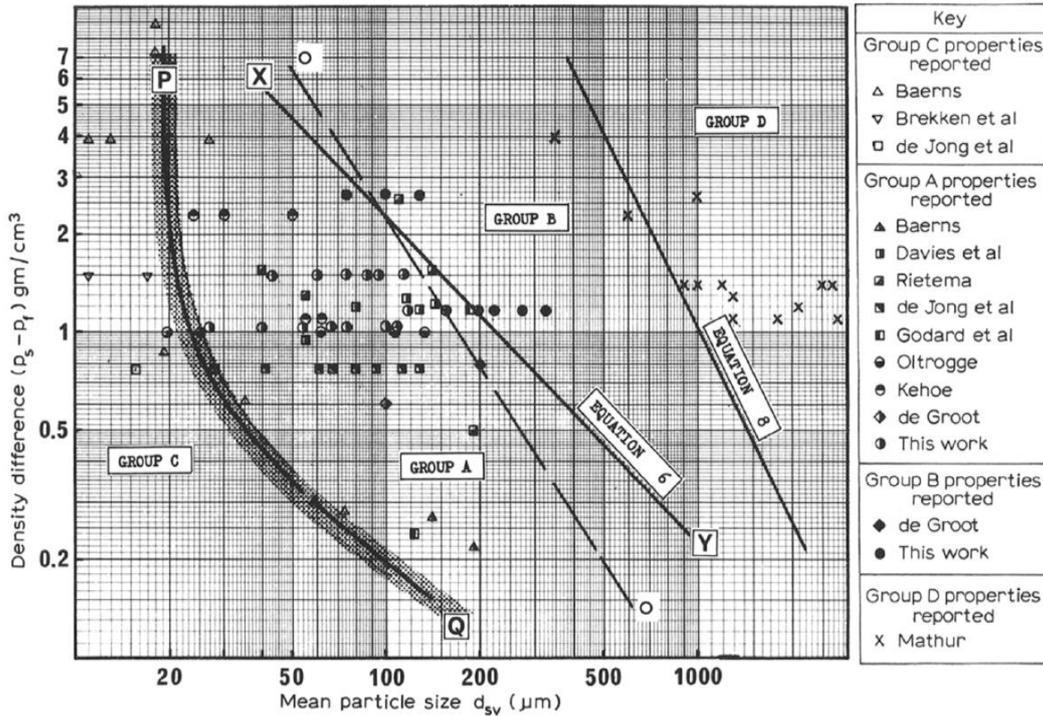
Figure 3. Diagram of the Geldart classification (Geldart, 1973).

2.2.2 Pressure drop

In a fluidized bed, pressure drop is generally used to indicate the fluidization state and the superficial fluid velocity required to fluidize a packed bed is known as the minimum fluidization velocity. As shown in Figure 4, in region OA, the bed remains fixed and pressure drop increases with increased fluid velocity; in region AB, the bed is partially fluidized and pressure drop decreases with increased fluid velocity; in region BC and afterwards, the bed is fully fluidized and pressure drop remains constant; the superficial fluid velocity in point A is the minimum fluidization velocity (Rhodes, 2008).
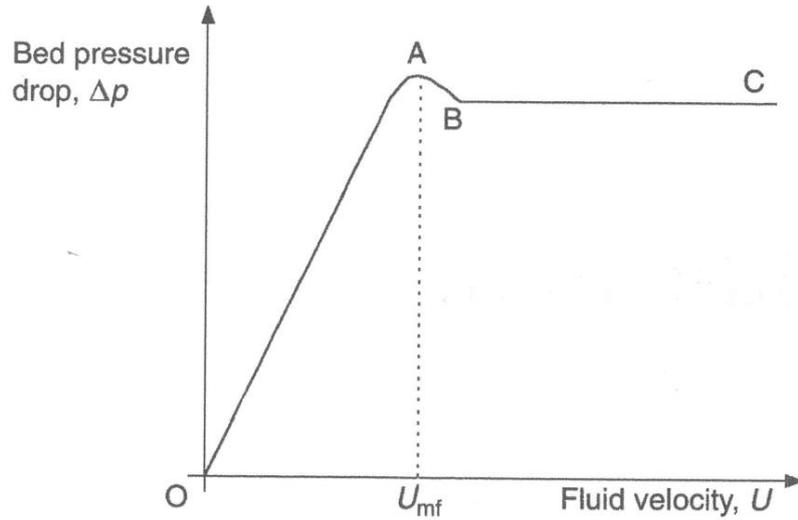
Figure 4. Ideal pressure drop velocity curve (Rhodes, 2008).

When the particles are fully fluidized, the pressure drop in a fluidized bed can be calculated from the force balance of the particles and expressed as (Davidson & Harrison, 1971; Kunii & Levenspiel, 1991; Rhodes, 2008):

$$\Delta p = H_{bed}(1 - \varepsilon)(\rho_p - \rho_a)g \qquad \text{Eq. (2)}$$

Where Δp is the pressure drop (Pa), H_{bed} is the bed height (m), ε is the void fraction, ρ_p is the density of particles (kg/m^3), ρ_a is the density of air (kg/m^3), g is the gravitational acceleration (m/s^2).

Generally, when the particles are fully fluidized, the relationship between the pressure drop and the air velocity can be described by the Ergun equation (Ergun, 1952):

$$\frac{(-\Delta p)}{H_{bed}} = 150\frac{\mu U}{D^2}\frac{(1 - \varepsilon)^2}{\varepsilon^3} + 1.75\frac{\rho_a U^2}{D}\frac{(1 - \varepsilon)}{\varepsilon^3} \qquad \text{Eq. (3)}$$

Where μ is the viscosity of air ($Pa \cdot s$), U is the superficial air velocity (m/s), and D is the particle diameter (m).

2.2.3 Minimum fluidization velocity

The superficial air velocity at the incipient fluidization is the minimum fluidization velocity. It is the lowest air velocity required to fluidize the particles in a fluidized bed.

By introducing the Archimedes number (Ar):

$$Ar = \frac{\rho_a(\rho_p - \rho_a)gD^3}{\mu^2} \qquad \text{Eq. (4)}$$

And the particle Reynolds number at the incipient fluidization ($Re_{p,mf}$):

$$Re_{p,mf} = \frac{U_{mf}D\rho_a}{\mu} \qquad \text{Eq. (5)}$$

Where U_{mf} is the minimum fluidization velocity (m/s).

The Ergun equation Eq. (3) can be written as (Kunii & Levenspiel, 1991):

$$Ar = 150\frac{(1 - \varepsilon_{mf})}{\varepsilon_{mf}^3\phi_s^2}Re_{p,mf} + 1.75\frac{1}{\varepsilon_{mf}^3\phi_s}Re_{p,mf}^2 \qquad \text{Eq. (6)}$$

Where ε_{mf} is the bed void fraction at the incipient fluidization and ϕ_s is the sphericity of the particles.

The Eq. (6) can be rewrite as (Kunii & Levenspiel, 1991):

$$Ar = K_1 Re_{p,mf}^2 + K_2 Re_{p,mf} \qquad \text{Eq. (7)}$$

Where,

$$K_1 = \frac{1.75}{\varepsilon_{mf}^3\phi_s} \qquad \text{Eq. (8)}$$

And,

$$K_2 = \frac{150(1 - \varepsilon_{mf})}{\varepsilon_{mf}^3\phi_s^2} \qquad \text{Eq. (9)}$$

It was found (Wen & Yu, 1966) that K_1 and K_2 stayed nearly constant depending on the particle type and size (when the air Reynolds number was between 0.001 and 4000). They also predicated the minimum fluidization velocity with ±34% standard deviation.

To calculate the minimum fluidization velocity of coarse particles, the values of K_1 and K_2 were recommended (Chitester et al., 1984) as 28.7 and 0.0494, respectively. The Eq. (7) can be written as:

$$Re_{p,mf} = [(28.7)^2 + 0.0494 \, Ar]^{1/2} - 28.7 \qquad\qquad \text{Eq. (10)}$$

To calculate the minimum fluidization velocity of fine particles, the values of K_1 and K_2 were recommended (Wen & Yu, 1966) as 33.7 and 0.0408, respectively.

The Eq. (7) can be written as:

$$Re_{p,mf} = [(33.7)^2 + 0.0408 \, Ar]^{1/2} - 33.7 \qquad\qquad \text{Eq. (11)}$$

Then the minimum fluidization velocity can be calculated using the Eq. (5).

2.2.4 Particle terminal velocity

In a fluidized bed, in order to fluidize the particles therein, the air velocity should be higher than the minimum fluidization velocity. Meanwhile, the air velocity should be lower than the particle terminal velocity to allow the particles to circulate in the fluidized bed.

The particle terminal velocity can be estimated from the force balance of a single particle and expressed as (Kunii & Levenspiel, 1991):

$$U_t = \left[\frac{4D(\rho_p - \rho_a)g}{3\rho_a C_D} \right]^{1/2} \qquad\qquad \text{Eq. (12)}$$

Where U_t is the particle terminal velocity and C_D is the drag coefficient that can be determined empirically (Yow, Pitt, & Salman, 2005).

In order to evaluate the particle terminal velocity directly, based on the equation form suggested by Turton and Clark (1987), Haider and Levenspiel (1989) presented following approximation:

$$U_t^* = \left[\frac{18}{(D^*)^2} + \frac{2.335 - 1.744\phi_s}{(D^*)^{0.5}} \right]^{-1}, \qquad 0.5 \le \phi_s \le 1 \qquad\qquad \text{Eq. (13)}$$

Where U_t^* and D^* were defined as:

$$U_t^* = U_t \left[\frac{\rho_a^2}{\mu(\rho_p - \rho_a)g} \right]^{1/3} = \frac{Re_p}{Ar^{1/3}} = \left(\frac{4}{3} \frac{Re_p}{C_D} \right)^{1/3} \qquad\qquad \text{Eq. (14)}$$

$$D^* = D \left[\frac{\rho_a (\rho_p - \rho_a) g}{\mu^2} \right]^{1/3} = Ar^{1/3} = \left(\frac{3}{4} C_D Re_p^2 \right)^{1/3}$$

Eq. (15)

Re_p is the particle Reynolds number:

$$Re_p = \frac{UD\rho_a}{\mu}$$

Eq. (16)

Graphically, the Eq. (13) can be presented as:
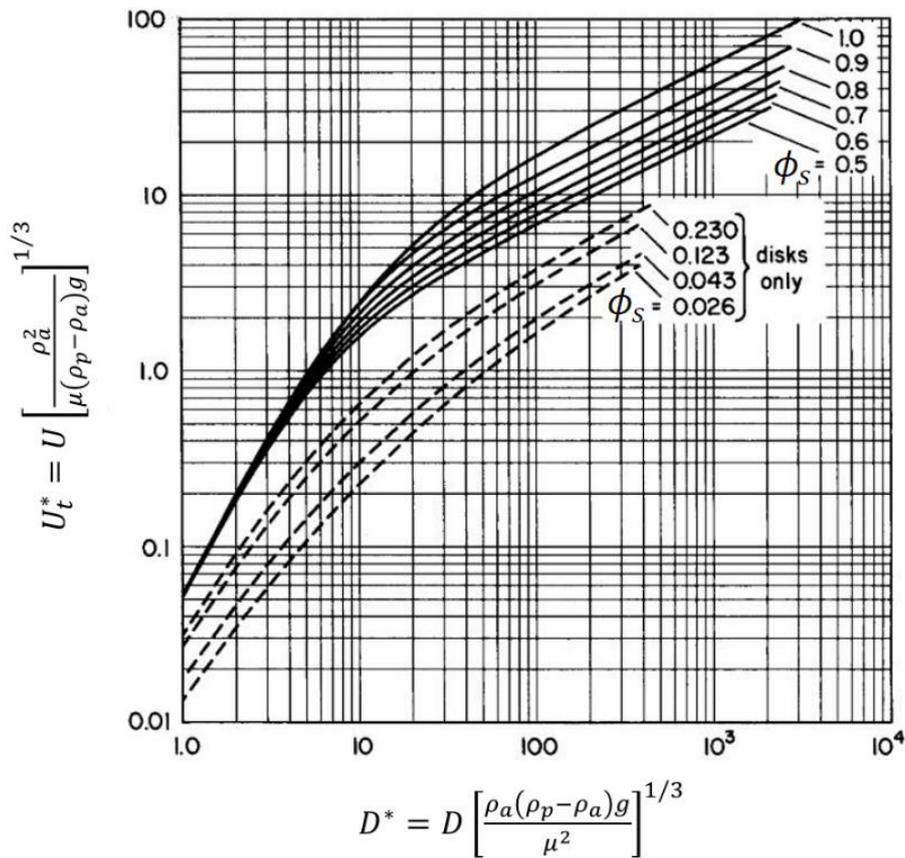
Figure 5. Chart for finding the terminal velocity of a single particle (Haider & Levenspiel, 1989).

2.3 Concepts of temperature measurement

2.3.1 Concept of temperature probes

In order to measure the particle temperature in a fluidized bed, temperature probes were widely used by previous researchers (Baeyens & Goossens, 1973; Borodulya et al., 1991; Gunn & De Souza, 1974; Gunn & Khalid, 1975; Malek & Lu, 1964; Petrovic et al., 1968; Valenzuela & Glicksman, 1984; van Heerden et al., 1953; Wadke et al., 2005).

The concept of the temperature measurement using the thermistor probes (Gunn & De Souza, 1974; Wadke et al., 2005) is the temperature dependence of electrical resistance (Childs, Greenwood, & Long, 2000). In advance, the relationship between the temperature of a conductor and its electrical resistance need to be calibrated. Then, in measurement, the calibration results can be used to convert the electrical resistance to the temperature. Depending on the material of the conductor, the accuracy of the thermistor can be very high.

Compared with the thermistors, the advantages of the thermocouples are their temperature range and speed of response (Childs et al., 2000). The concepts of the temperature measurement using the thermocouple probes (Baeyens & Goossens, 1973; Borodulya et al., 1991; Gunn & Khalid, 1975; Malek & Lu, 1964; Petrovic et al., 1968; Valenzuela & Glicksman, 1984; van Heerden et al., 1953) are the thermoelectric effects including the Seebeck effect, the Peltier effect and the Thomson effect.

The Seebeck Effect is described as (D. D. Pollock, 1971): " When two dissimilar conductors, A and B, comprise a circuit, a current will flow in that circuit as long as the two junctions are at different temperatures, $T < T + \Delta T$. Conductor A is defined as being positive with respect to B if the current (electrons) flows from A to B at the colder junction." (Figure 6).
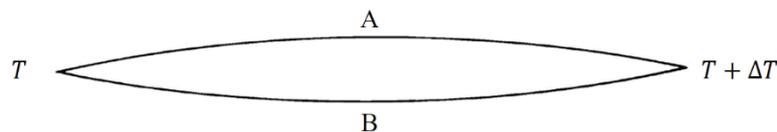
Figure 6. The Seebeck Effect (D. D. Pollock, 1971).

The Peltier Effect is described as (D. D. Pollock, 1971): "When an electric current flows across a junction of two dissimilar metals, heat is liberated or absorbed. When the electric current flows in the same direction as the Seebeck current, heat is absorbed at the hotter junction and liberated at the colder junction." (Figure 7).
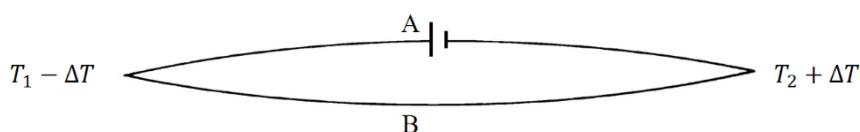
Figure 7. The Peltier Effect (D. D. Pollock, 1971).

Actually, the physical process described by the Seebeck effect and the Peltier effect is the same. This process can also be referred as the Peltier-Seebeck effect.

The Thomson effect is described as (D. D. Pollock, 1971): "The change in the heat content of a single conductor of unit cross section when a unit quantity of electricity flows through it along a temperature gradient of 1 K."

Basically, a thermocouple probe is made of two dissimilar metal (Metal A and B in Figure 8). The two metals are electrically connected in one end, which is called the measuring (hot) junction. In another end, the two metals are thermally connected, which is called the reference (cold) junction. If temperatures of the two junctions are different, a voltage called electromotive force (EMF) will be generated ($EMF = V_A - V_B$). As long as the cross-section of the two metal conductors are uniform along their length, the EMF is only affected by the temperature difference between the measurement (hot) junction and the reference (cold) junction, and not the temperature distribution along the conductor between them (J. Park & Mackay, 2003). Then the relationship between the EMF value and the temperature difference can be calibrated experimentally.
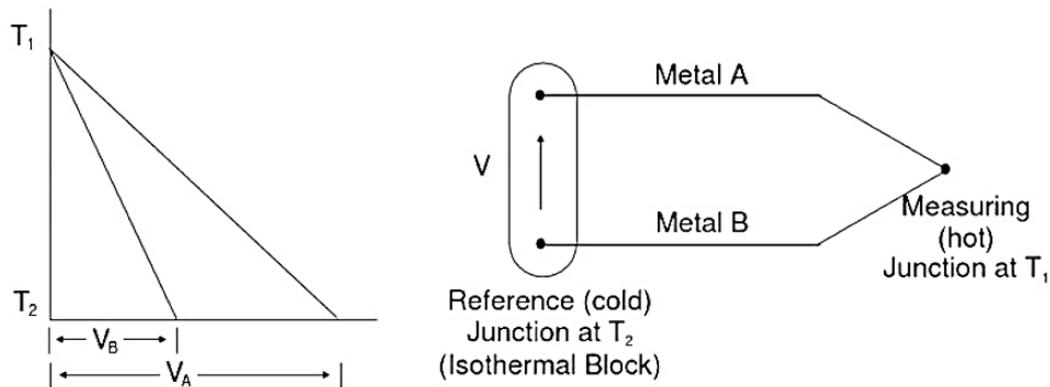
Figure 8. Structure of a thermocouple (J. Park & Mackay, 2003).

In a fluidized bed, when a thermocouple probe is used to measure the air temperature and the fluidized bed wall temperature, it should be noticed that the thermocouple

probes cannot respond to the temperature instantly and their measurement errors are affect by how the thermocouple probes are installed (R. Park et al., 1993).

When a thermocouple probe is used to measure the particle temperature, in addition to the response time and the installation effects, the measurement can also be affected by the particle circulation and the surrounding air of the particles (Baeyens & Goossens, 1973). Moreover, the inserted thermocouple probe has influence on the movement of particles (Leva, 1959).

2.3.2 Concept of thermal cameras

In order to improve the accuracy of the particle temperature measurement in a fluidized bed, thermal cameras were used by many researcher (Brown & Lattimer, 2013; Li et al., 2017; A. V. Patil, Peters, Sutkar, et al., 2015; Sutkar et al., 2015; Tsuji et al., 2010). The concepts of the temperature measurement using thermal cameras are the Kirchhoff's law of thermal radiation, the Planck's law, the Stefan-Boltzmann's law and the Wien's displacement law.

The Kirchhoff's law can be illustrated by the Figure 9.
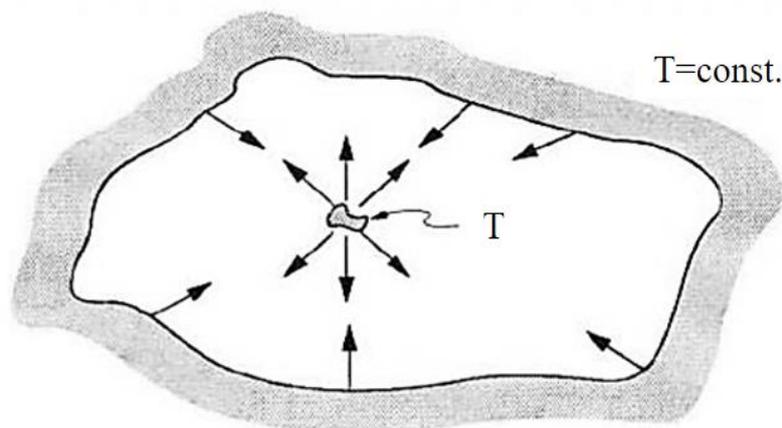
Figure 9. The Kirchhoff's law (Modest, 2003).

When two identical black-walled enclosures, thermally insulated on the outside, with each containing a small object – one black and the other one not. After a long time, both entire enclosures and the objects within them will be at a single uniform temperature (Modest, 2003). This indicates that when an object is in thermodynamic equilibrium, its emittance and absorptance are the same.

The Planck's law is reported by Max Planck (1901), which gives the spectral blackbody emissive power distribution (Williams, 2009):

$$W(\lambda, T) = e(\lambda)c_1/\pi\lambda^5 \left[\exp\left(\frac{c_2}{\lambda T}\right) - 1\right] \qquad \text{Eq. (17)}$$

Where $W(\lambda, T)$ is the radiance ($W \cdot m^{-2} \cdot sr^{-1} \cdot \mu m^{-1}$) for a wavelength λ in μm and a temperature T in Kelvin (K), c_1 equals to 3.7418×10^8, c_2 equals to 14387.9 and $e(\lambda)$ is the emissivity at a wavelength λ and can vary in the range 0 to 1.

The Stefan-Boltzmann's law gives the total radiation emitted from an object at a specific temperature and can be integrated from the Planck's law (Modest, 2003; Pan & Atungulu, 2010; Williams, 2009):

$$E_b(T) = \int_0^\infty W(\lambda, T)d\lambda = e(\lambda)\sigma T^4 \qquad \text{Eq. (18)}$$

Where σ is the Stefan-Boltzmann constant ($5.670 \times 10^{-8} \ W/m^2 \cdot K^4$).

The Wien's displacement law gives the peak wavelength (λ_{max}) of the spectral blackbody emissive power distribution (Modest, 2003; Pan & Atungulu, 2010; Williams, 2009):

$$\lambda_{max} = \frac{2898\mu m \cdot K}{T} \qquad \text{Eq. (19)}$$

Where unit of temperature T is Kelvin (K).

From the above concepts, it is known that if the radiation emitted from an object can be measured, the temperature of the object can be determined non-invasively. Depends on the wavelength of the radiation, the radiation emitted from an object are classified in several categories (as shown in Figure 10): gamma rays, x-rays, ultraviolet, visible, infrared, and microwaves.
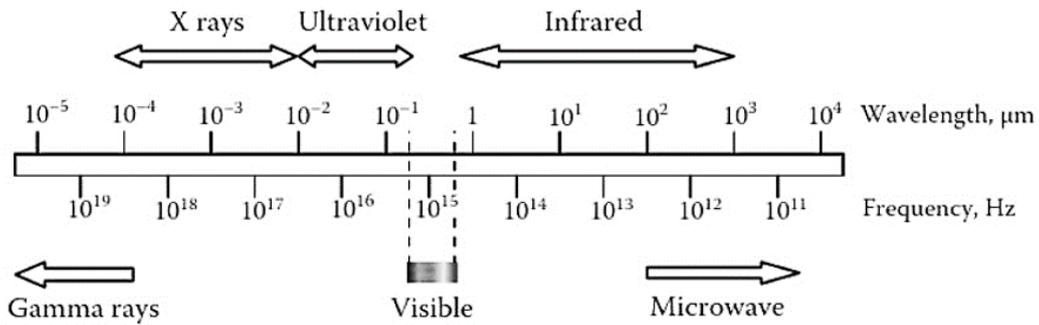
Figure 10. Names of the radiation with different wavelength (Pan & Atungulu, 2010).

Due to the heating effect of the infrared radiation, it is preferred to be used to determine the object temperature. The devices used to receive the infrared radiation emitted from an object are the infrared sensors. The infrared sensors can be divided into two types, one is the thermal sensor (also called radiation temperature sensors) and the other is the photon or quantum sensor (Budzier & Gerlach, 2011). When the thermal sensors received infrared radiation, their temperature will be changed. The temperature change is then converted into an electric output signal. When the photon or quantum sensors received infrared radiation, an electric output signal is generated directly. The time required by this process is the exposure time (the detector time constant, or the integration time). For both types of the infrared sensors, the electric output signal generated can be correlated to the received infrared radiation and used to determine the object temperature.

Generally, the wavelength-dependence of the photon or quantum sensors is much heavier than the thermal sensors (Budzier & Gerlach, 2011). In operation, cooling systems are also important for the photon or quantum sensors, but not necessary for the thermal sensors.

The infrared sensors can be single-element sensors or multi-element sensors. The elements (sometimes also named as detectors) in the multi-element sensors are usually arranged in an array and called as the array sensors. Compared with the single-element sensors, the array sensors can output a matrix of the electric signal to indicate the received infrared radiation.

A thermal camera is a system mainly composed of a lens, an array infrared sensor and a digital signal processor. Depending on the thermal camera module, more

components may be included, such as the system controller, the cooling system and etc.

In operation, the noise (the mean small random variations of a signal) is an important factor that need to be concerned (Budzier & Gerlach, 2011). The main sources that cause the noise are: the thermal noise (also known as Johnson-Nyquist noise (Johnson, 1928; Nyquist, 1928)) that is related to the movement of the free charge carriers at the thermal sensor, the current noise that is related to the potential barrier that the charge carriers have to overcome (Budzier & Gerlach, 2011), the radiation noise that is related to the distribution of the object emission (Budzier & Gerlach, 2011), and the temperature fluctuation noise that is related to the temperature of the thermal sensor (Budzier & Gerlach, 2011; Kruse, 2001). Typically, the noise in a continuous measurement process follows a normal distribution that can be described with expected value and variance (Budzier & Gerlach, 2011).

2.4 Using thermal camera in a fluidized bed

2.4.1 Fundamental of image segmentation

Formally, the image segmentation can be defined as (Pal & Pal, 1993): if F is the set of all pixels and $F_{define}(\ )$ is a uniformity (homogeneity) predicate defined on groups of connected pixels, then segmentation is a partitioning of the set F into a set of connected subsets or regions $(F_1, F_2, ..., F_n)$ such that:

$$\bigcup_{i=1}^{n} F_i = F \qquad with \qquad F_i \bigcap F_j = \emptyset, \qquad i \neq j \qquad \qquad \text{Eq. (20)}$$

The uniformity predicate $F_{define}(F_i) = true$ for all regions (F_i) and $F_{define}(F_i \cup F_j) = false$, when F_i is adjacent to F_j.

Threshold-based image segmentation is one of the simplest and most popular techniques for image segmentation (Fu & Mui, 1981; Pal & Pal, 1993; Taxt, Flynn, & Jain, 1989). The advantages of this technique are: the approaches and algorithms are easy to be programmed and the computational speed is fast. The disadvantages of this technique are (Fu & Mui, 1981; Pal & Pal, 1993; Taxt et al., 1989): the output is sensitive to the complexity of the image (such as, the size and shape of the object and the contrast between the object and the background) and is difficult to be evaluated.

Depending on the number of thresholds used for image segmentation, the threshold-based image segmentation can be categorized as the bi-level thresholding (the single-threshold method) or the multi-thresholding (the multi-threshold method) (Pal & Pal, 1993).

There are many algorithms (Kittler & Illingworth, 1986; Otsu, 1979; Wong & Sahoo, 1989) can be used to compute the single-threshold. The Otsu's method (Otsu, 1979) is one of the algorithms that has been widely used. In this method, the pixels of a given image were represented in Z grey levels $[1,2, \dots, Z]$. Then the distribution of the grey values can be normalized and presented as a probability distribution:

$$p_i = \frac{n_i}{N_{img}} \qquad \text{Eq. (21)}$$

Where p_i is the probability of the pixels with grey level i, n_i is the number of the pixels with grey level i, N_{img} is the total number of pixels in the image. The sum of the total probability distribution (ω_0) and the class mean grey level (μ_0) are respectively:

$$\omega_0 = \sum_{i=1}^{Z} p_i = 1 \qquad \text{Eq. (22)}$$

$$\mu_0 = \frac{\sum_{i=1}^{Z} i p_i}{\omega_0} = \sum_{i=1}^{Z} i p_i \qquad \text{Eq. (23)}$$

Any grey level k can separate the pixels into two classes: $[1,2, \dots, k]$ and $[k+1, k+2, \dots, Z]$.

For the pixels in the class $[1,2, \dots, k]$, the sum of the probability distribution ($\omega_1(k)$) and the class mean grey level ($\mu_1(k)$) are respectively:

$$\omega_1(k) = \sum_{i=1}^{k} p_i \qquad \text{Eq. (24)}$$

$$\mu_1(k) = \frac{\sum_{i=1}^{k} i p_i}{\omega_1} \qquad \text{Eq. (25)}$$

For the pixels in the class $[k + 1, k + 2, ..., Z]$, the sum of the probability distribution ($\omega_2(k)$) and the class mean grey level ($\mu_2(k)$) are respectively:

$$\omega_2(k) = \sum_{i=k+1}^{Z} p_i \qquad \text{Eq. (26)}$$

$$\mu_2(k) = \frac{\sum_{i=k+1}^{Z} i p_i}{\omega_2} \qquad \text{Eq. (27)}$$

In order to evaluate the "goodness" of the grey value k as a threshold, a between-class variance is defined as:

$$\sigma_B^2(k) = \omega_1(k)[\mu_1(k) - \mu_0(k)]^2 + \omega_2(k)[\mu_2(k) - \mu_0(k)]^2 \qquad \text{Eq. (28)}$$

The optimal threshold k^* is searched within the grey values range $[0, 1, ..., Z]$ to maximize the $\sigma_B^2(k)$:

$$\sigma_B^2(k^*) = \max_{1 \le k \le Z} \sigma_B^2(k) \qquad \text{Eq. (29)}$$

Then Otsu (1979) suggested k^* as the threshold of the image.

The multi-threshold method can be explained as selecting several thresholds for the entire image or selecting single thresholds for each block that is divided from the entire image (Chow & Kaneko, 1972; Fu & Mui, 1981; Nakagawa & Rosenfeld, 1979; Pal & Pal, 1993; Taxt et al., 1989; Yanowitz & Bruckstein, 1989).

In addition to threshold-based image segmentation, there are other image segmentation techniques, such as region-based, edge-based, and neural network-based image segmentation. Compared to the threshold-based image segmentation that only considers the grey value of the pixels, these techniques also take into account the connectivity of the pixels.

The region-based image segmentation (Calderon De Anda, Wang, & Roberts, 2005; Rajab, Woolfson, & Morgan, 2004) is to segment the image into meaningful pixel clusters based on their features/properties (e.g. area, perimeter, circularity, etc.). The edge-based image segmentation (Calderon De Anda et al., 2005; Canny, 1986) is to segment the image into meaningful pixel clusters based on the points of abrupt changes in grey values. The neural network-based image segmentation (Frei & Kruis,

2020) is to segment the image into meaning pixel clusters in a manner similar to some aspects of the human information processing system.

2.4.2   Methods used by previous researchers

In the literature, Tsuji et al. (2010) used a thermal camera to monitor the cooling process of fluidizing particles in a flat spout-fluidized bed with air introduced. The observation window was made of spinel. The thermal camera used was TVS-8502 (NEC Avio Infrared Technologies Co., Ltd). Resolution of the thermal image was $251 \times 236\ pixels$. Size of each pixel in the thermal images was $0.33\ mm$. Frame rate was $120\ fps$. The particles were spherical aluminium particles and coated with black body paint (THI-1B, TASCO JAPAN). The mean particle diameter was $2\ mm$. The dimension of the vessel was $400\ mm\ (Height) \times 76\ mm\ (Width) \times 21\ mm\ (Depth)$. Initial temperature of the particles and the air was $423\ K$ and $292\ K$, respectively. The particle cooling process was monitored for $8.1\ s$.

Tsuji et al. (2010) correlated the temperature of the particles measured by the thermal camera to the temperature of the particles measured by a thermocouple probe. In the thermal camera, the received infrared radiation by the thermal camera was correlated to the particle surface temperature using the Stefan-Boltzmann Law (Eq. (18)), and 0.94 was used as the emissivity of the particles to obtain an uncalibrated temperature. The calibration expression they obtained was:

$$T_{cal} = 1.0466 T_{uncal} + 8.0873 \qquad\qquad \text{Eq. (30)}$$

Where T_{cal} is the calibrated particle temperature (K), and T_{uncal} is uncalibrated particle temperature measured from the thermal camera (K).

Tsuji et al. (2010) did not segment their thermal images (Figure 11). However, from the figure, it can be seen that both the particles and the fluidized bed wall are in the thermal images. Without image segmentation, the particles and the fluidized bed wall cannot be separated. Therefore, they roughly compared the temperature change of the particles directly based on the snapshots of the thermal images without quantifying the temperature of the particles.
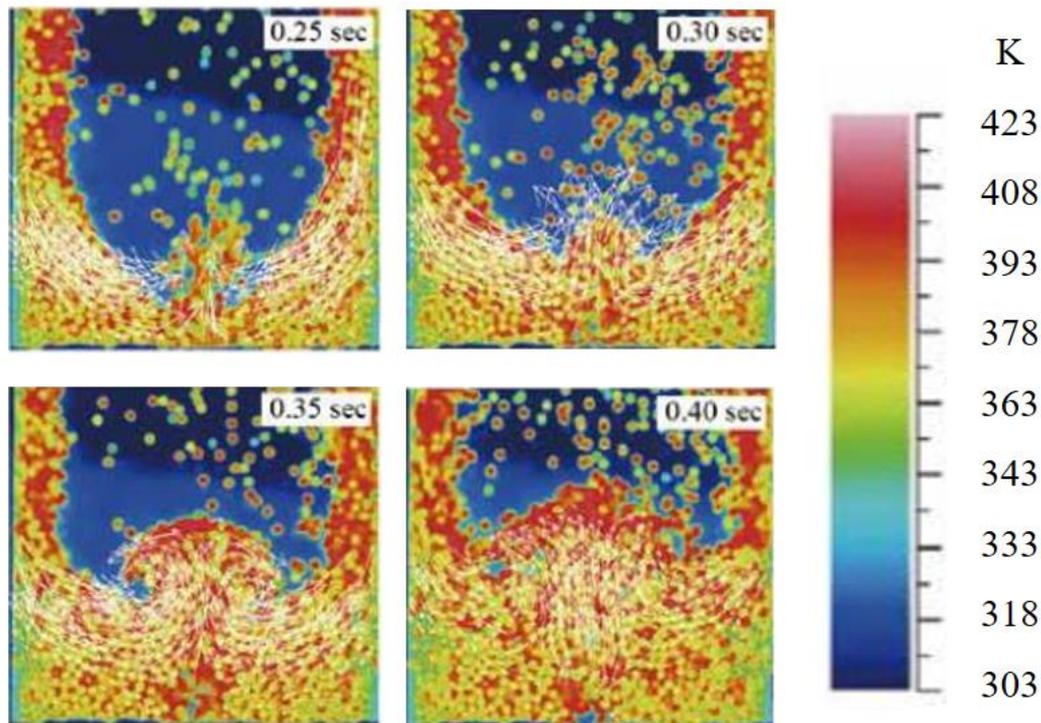
Figure 11. Thermal images used by Tsuji et al. (2010).

Brown and Lattimer (2013) used a thermal camera to monitor the heating process of fluidizing particles in a flat spout-fluidized bed with air introduced. The observation window was made of sodium chloride. The thermal camera used was FLIR SC655. The detector time constant and frame rate was $8\ ms$ and $200\ fps$, respectively. Resolution of the thermal image was $640 \times 120\ pixels$. In the thermal images, about one pixel was occupied by a particle. The particles were glass beads with mean particle diameter $550\ \mu m$. The dimension of the fluidized bed was $280\ mm\ (Height) \times 56.4\ mm\ (Width) \times 4.95\ mm\ (Depth)$. Initial temperature of the particles and the air was same and around $295\ K$. Then the air temperature was increased and the particles were heated. The particle heating process was monitored for $60\ s$.

Brown and Lattimer (2013) considered the influence of the observation window in the calibration procedure. They placed the particles on a copper plate coated in paint close to an ideal blackbody with low radiation reflection. The observation window was positioned just above the particles and multiple bare bead thermocouples were immersed in the particles. Then the whole setup was encompassed in a black body box with an opening for the thermal camera. The distance between the thermal camera

and the particles was same as it was in their experimental setup. The calibration expression they obtained was:

$$T_{cal} = 1.44 T_{uncal} - 130.89$$

Eq. (31)

Where T_{cal} is the calibrated particle temperature (K), and T_{uncal} is uncalibrated particle temperature measured from the thermal camera (K).

Brown and Lattimer (2013) also did not segment their thermal images (Figure 12). They used the average of the cross-sectional temperatures as the particle temperature and neglected the temperature of the stagnant particles. However, from the figure, it can be seen that the particles are not fully fluidized and neglecting the stagnant particles can result in inaccurate temperature measurement of the particles.
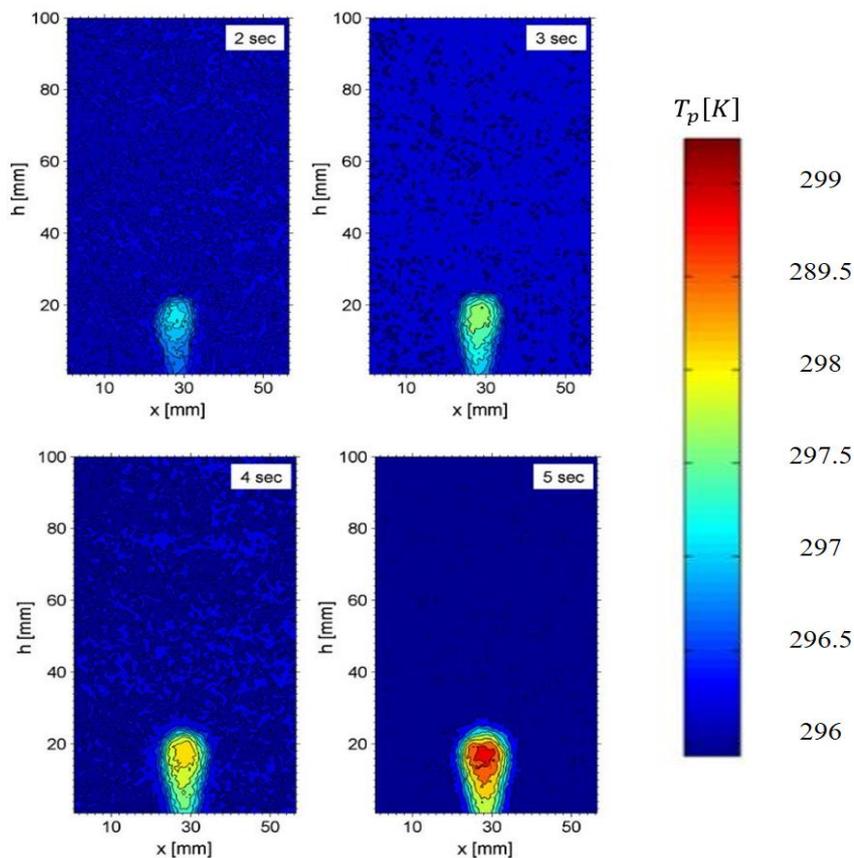
Figure 12. Thermal images used by Brown and Lattimer (2013).

Patil et al. (2015) used a thermal camera to monitor the cooling process of fluidizing particles in a flat spout-fluidized bed with nitrogen gas introduced. The observation window was made of sapphire glass. The thermal camera used was FLIR SC7600. The detector time constant and frame rate was $0.6\ ms$ and $10\ fps$, respectively.

Resolution of the thermal image was $250 \times 512\ pixels$. The particles were glass beads. The mean particle diameter was 0.5 and $1\ mm$, respectively. The dimension of the fluidized bed was $200\ mm\ (Height) \times 80\ mm\ (Width) \times 15\ mm\ (Depth)$. Initial temperature of the particles and the air was around $393\ K$ and $293\ K$, respectively. The particle cooling process was monitored for less than $60\ s$.

Patil et al. (2015) used a thermal camera and a high speed camera simultaneously. The threshold-based image segmentation was used first to identify the pixels representing the particles in their thermal images (Figure 13_a).

(a) Raw IR image   (b) Direct filtered IR image
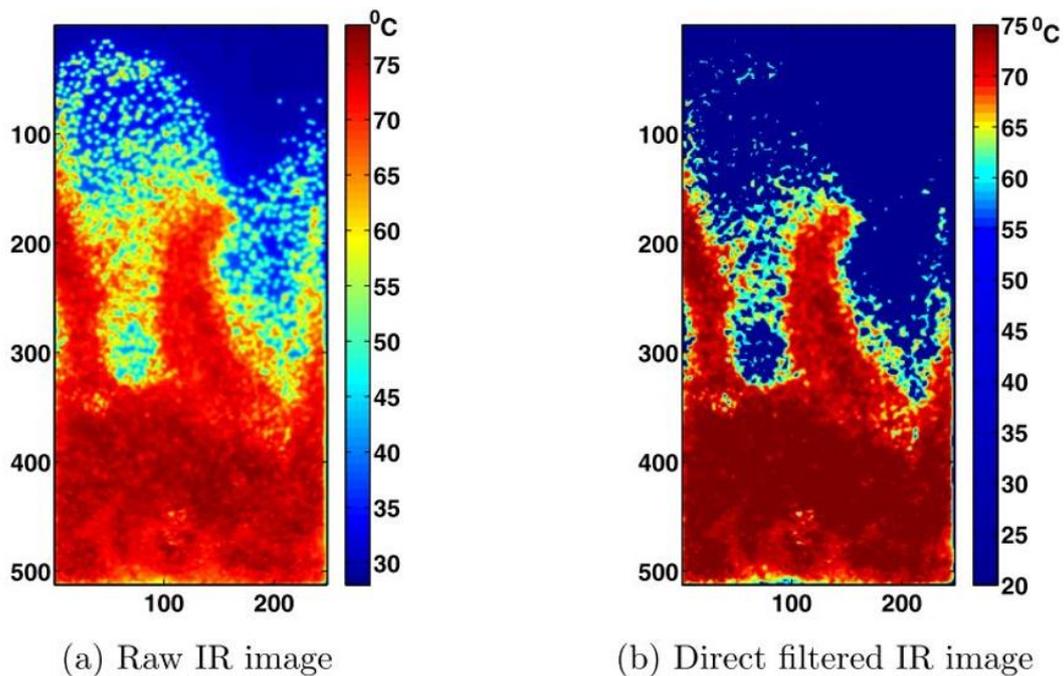
Figure 13. Thermal images used by Patil et al. (2015).

The threshold (T_{thr}) they used was calculated from the following equation (based on observation, they found it can result in good images):

$$T_{thr} = 0.25T_{bg} + 0.75\langle T_p \rangle_{pix}$$

Eq. (32)

Where T_{bg} is the temperature of the pixels representing the background, and $\langle T_p \rangle_{pix}$ is the mean temperature of the pixels representing the particles in the previous thermal image. Initially, $\langle T_p \rangle_{pix}$ was picked manually in the first thermal image. Temperature of the background was assumed to be a constant.

Pixels with temperature higher than T_{thr} was then identified as the pixels representing the particles in the thermal images (Figure 13_b). These thermal images were then compared with the visual images from the high speed camera to extract the overlaying pixels as the final pixels that represent the particles in both the thermal images and the visual images.

However, by comparing the Figure 13_a and the Figure 13_b, it can be found that some of the particles are also filtered by using the threshold-based image segmentation. Since the accuracy of the threshold-based image segmentation is affected by the complexity of the thermal images and the amount of the filtered particles cannot evaluated, uncertainty will be introduced in the online temperature measurement of the fluidizing particles. Patil et al. (2015) fitted a tracer particle at the tip of thermocouple probe and placed the probe inside the fluidized bed. Then particle was positioned very close to the observation window. By pouring hot particles into the fluidized bed, they varied the temperature of the tracer particle. They also pointed that the calibrated particle temperature should be correlated to the digital level (i.e. signal value) rather than the uncalibrated particle temperature from the thermal camera. Therefore, a relationship between the calibrated particle temperature and the signal value of the pixel that represent the particle were obtained.

Additionally, Patil et al. (2015) attached a sample particle to the tip of a straight wire. The particle was first immersed in the hot particle bed and then gradually lifted. In the meanwhile, they maintained a small background gas velocity of 0.1 m/s to keep the particle in a gas environment that has a temperature equal to the bulk temperature of the bed. By doing so, they estimated the error in the particle temperature when it moves between dense and isolated regions of the bed.

Sutkar et al. (2015) used a thermal camera to monitor the wetting process of fluidizing particles in a flat spout-fluidized bed with nitrogen gas introduced. The observation window was made of sapphire glass. The thermal camera used was FLIR SC7600. The detector time constant and frame rate was $0.6\ ms$ and $100\ fps$, respectively. Resolution of the thermal image was $640\ \times\ 512\ pixels$. The particles were non-porous glass beads and porous γ-Aluminium Oxide particles, respectively. The mean particle diameter was $1\ mm$. The dimension of the fluidized bed was $180\ mm\ (Height)\ \times\ 80\ mm\ (Width)\ \times\ 18\ mm\ (Depth)$. Initial temperature of

the particles was around $303\ K$. Then water droplets with $293\ K$ temperature was sprayed from the bottom of the fluidized bed. The spraying process was monitored for $120\ s$.

Sutkar et al. (2015) used the same method as Patil et al. (2015). Their thermal images are shown in Figure 14.
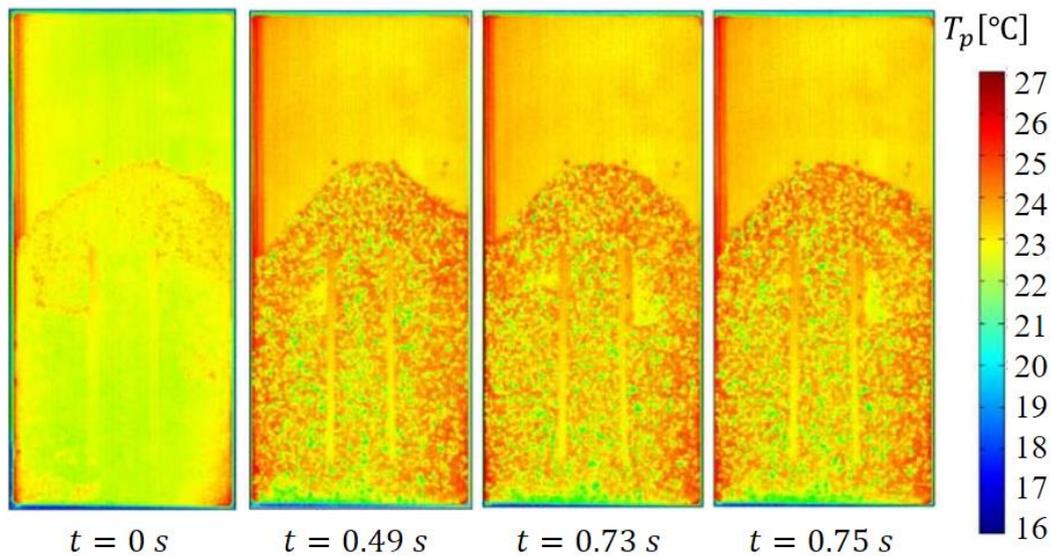
Figure 14. Thermal images used by Sutkar et al. (2015).

Sutkar et al. (2015) and calibrated the particle temperature and the signal value of the pixel that represent the particle similar to the method used by Patil et al. (2015).

Li et al. (2017) used a thermal camera to monitor the adsorption process of fluidizing particles in a flat spout-fluidized bed with gas (a mixture of nitrogen and carbon dioxide) introduced. The observation window was made of sapphire glass. The thermal camera used was FLIR X8400sc. The detector time constant and frame rate was $0.54\ ms$ and $40\ fps$, respectively. Resolution of the thermal image was $1280\ \times\ 1024\ pixels$. The particles were zeolite 13X beads. The particle diameter was between 1.8 and 2 mm, respectively. The dimension of the fluidized bed was $250\ mm\ (Height)\ \times\ 80\ mm\ (Width)\ \times\ 15\ mm\ (Depth)$. Initial temperature of the particles and the gas was similar and around $291\ K$. When the gas was introduced, the particles were heated up due to the CO_2 adsorption. The adsorption process was monitored for $120\ s$.

Li et al. (2017) also used a thermal camera and a high speed camera simultaneously. The threshold-based image segmentation was used first to identify the pixels representing the particles in their thermal images. They normalized the intensity of the thermal images into the scale 0 to 1 first and used 0.32 (picked from the trial error experimentation) as the threshold. Then the thermal image was compared with the visual images to extract the overlaying pixels as the final pixels that represent the particles in both the thermal images and the visual images. The scheme they used is shown in Figure 15. In the figure, IR image is referred as the thermal image. Li et al. (2017) calibrated the particle temperature and the signal value of the pixel that represent the particle similar to the method used by Patil et al. (2015).
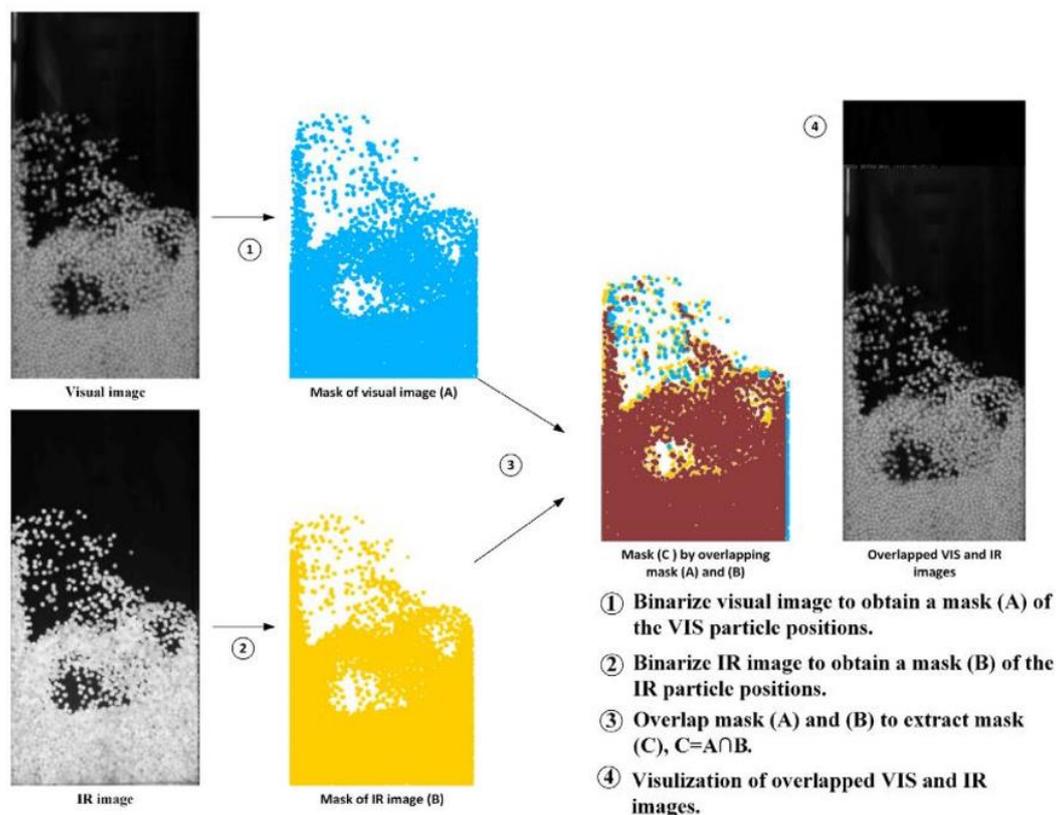
Figure 15. Thermal images used by Li et al. (2017).

2.5   Heat transfer models in a fluidized bed

2.5.1   Trend of the particle temperature

In the literature, by using thermocouple probes, Malek and Lu (1964) studied the radial and axial temperature of the particle bed in a cylindrical spouted fluidized bed.

They drilled a series of holes on the fluidized bed wall that also allows the thermocouple probes to measure temperature at different axial position.

Inside the fluidized bed, they also compared the temperatures measured by bare thermocouple probes and thermocouple probes covered by a fine screen (to prevent the contact of the particles). The two measured temperatures were found to be different when the measured position was closer to the bottom of the fluidized bed, but the difference was decreased when the measured position was closer to the top of the fluidized bed. Considering the particles near the bottom of the fluidized bed are more than the particles close to the top of the fluidized bed, this indicates that the particle temperature measured by thermocouple probes are affected by the particles and their surrounding air. It is therefore necessary to measure the particle temperature and the air temperature separately.

As shown in Figure 16, their results shows that when the measured position was closer to the top of the fluidized bed or closer to the fluidized bed wall, temperature of the particle bed was decreased. This indicates that the temperature distribution inside a fluidized bed is related to the temperatures of the air and the fluidized bed wall.
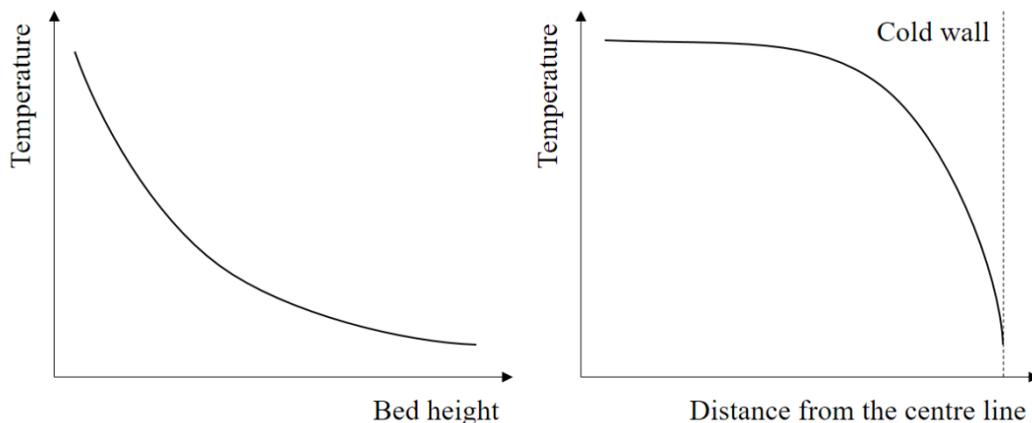
Figure 16. Typical temperature profile for a spouted bed (Malek & Lu, 1964).

By using a thermal camera, Brown and Lattimer (2013) measured the particle temperature separately during the particle heating process in a flat fluidized bed. They also measure the air temperature using thermocouple probes. But limited by the identification and correlation methods, their measured temperatures were not able to be presented directly. Therefore, they introduced a dimensionless term (θ_{gp}):

$$\theta_{gp} = \frac{T - min(T_{p,s}, T_g)}{max(T_{p,s}, T_g) - min(T_{p,s}, T_g)} \qquad \text{Eq. (33)}$$

Where T is the instantaneous measured temperature (particle temperature or the air temperature), $T_{p,s}$ is the particle temperature, T_g is the air temperature.

Then the time averaged dimensionless term of the air and the particles were plotted against the bed height (H), as shown in Figure 17. However, limited by the experimental setup of the flat fluidized bed, they did not measure the fluidized bed wall temperature. Also, they did not compare the temperatures of the air, the particles and the fluidized bed wall with time.
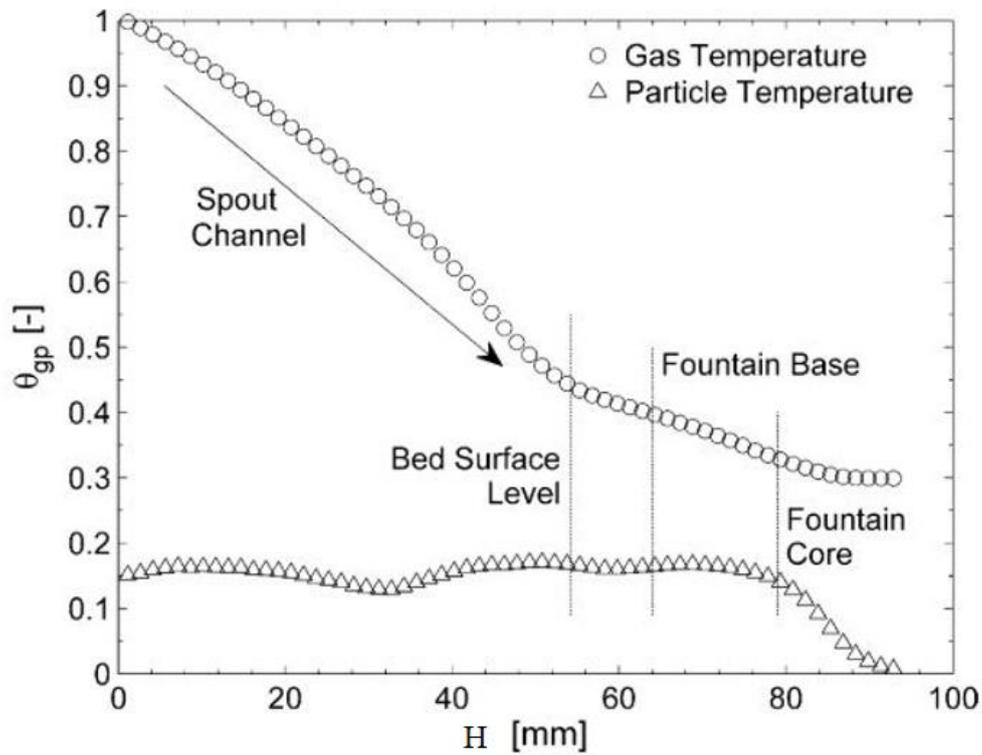
Figure 17. The 60 s time average dimensionless air and particle temperature distribution in the spouted regime at 3.0 u_{mf} (Brown & Lattimer, 2013).

By using a thermal camera, Patil et al. (2015) also measured the particle temperature separately during the particle cooling process in a flat fluidized bed. They added $120°C$ particles in the fluidized bed with $20°C$ nitrogen gas supplied. In their experiment, they compared the effect of the inlet gas velocity and the loaded particle mass on the particle temperature with time (Figure 18). From their results, it can be found that when the inlet gas velocity was higher or the loaded particle mass was less,

the particle temperature was lower and closer to the cold gas temperature ($20°C$). However, in their experiment, they assumed that the fluidized bed wall temperature did not change over time.
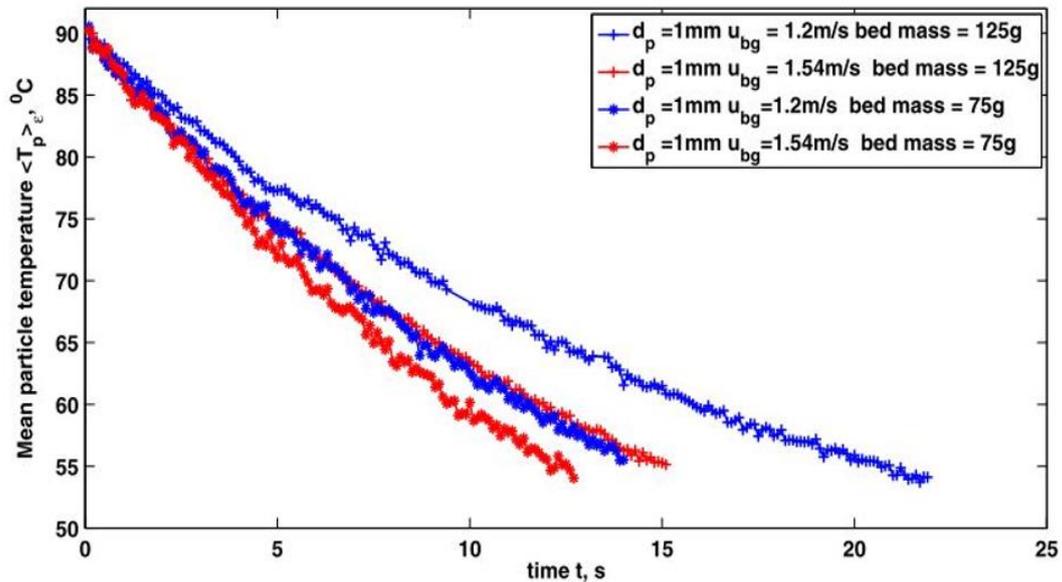
Figure 18. Mean temperatures of particles with time in a cooling process (A. V. Patil, Peters, Sutkar, et al., 2015).

2.5.2 Fundamental models

Since the particle temperature can be measured more accurately using a thermal camera, it is interesting to investigate the heat transfer relevant to the particle temperature. Generally, there are three fundamental models to describe the heat transfer mechanisms in a fluidized bed: conduction, convection and radiation.

The conduction is the heat transfer caused by the temperature gradient through a solid material (Han, 2012; Serth & Lestina, 2014). The heat transfer can be primarily described by the Fourier's conduction law:

$$q_{cond} = -k_s \frac{\Delta T_s}{dx}$$

<div align="right">Eq. (34)</div>

Where q_{cond} is the conduction heat flux per area (W/m^2), k_s is the thermal conductivity of the solid material ($W/m \cdot K$), and $\frac{\Delta T_s}{dx}$ is the temperature gradient through the solid material (K/m).

The convection is the heat transfer caused by the air flow motion over a solid surface (Serth & Lestina, 2014). It can be described by:

$$q_{conv} = h_{as} A_{as} \Delta T_{as} \qquad \text{Eq. (35)}$$

Where q_{conv} is the convection heat flux (W), h_{as} is the heat transfer coefficient between the air and the solid material ($W/m^2 \cdot K$), A_{as} is the contact area between the air and the solid surface (m^2), and ΔT_{as} is the characteristic temperature difference between the air and the solid.

The radiation is the heat transfer caused by the radiation emitted from the air and the solid. It can be described by the Stefan-Boltzmann's law (Eq. (18)).

In a fluidized bed, two heat transfer processes are mostly concerned (Davidson & Harrison, 1971): heat transfer between the particles and the fluidized bed wall, and heat transfer between the particles and the air.

2.5.3   Particle-wall heat transfer coefficient

When considering the heat transfer process between the particles and the fluidized bed wall, it is widely accepted that the particles in contact with the fluidized bed wall will be washed away by fresh bed particles, and the contact time of the particles and the fluidized bed wall controls the heat transfer process (Bao, Duan, Wu, & Zhao, 2020; Decker & Glicksman, 1983; Kunii & Levenspiel, 1991; Mickley & Fairbanks, 1955).

As shown in Figure 19, particles will be resting on the fluidized bed wall for the time length τ, and then be replaced by other particles.
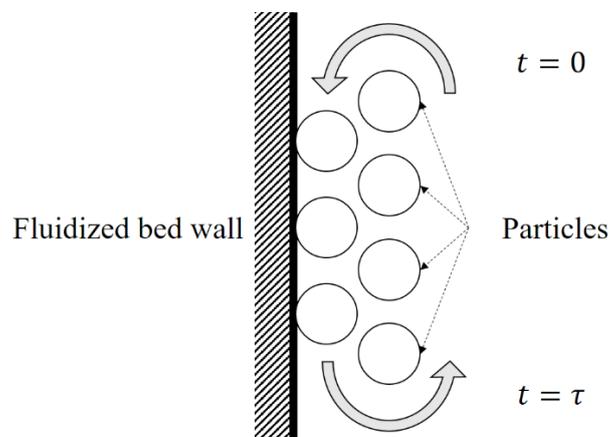
Figure 19. Models for heat transfer between particles and the fluidized bed wall.

For the large particles with short contact time, the heat transfer coefficient between the particles and the fluidized bed wall was correlated as (Kunii & Levenspiel, 1991):

$$\frac{h_{bw}D}{(1-\varepsilon)k_a} = 5.0 + 0.05PrRe_p \qquad \text{Eq. (36)}$$

Where h_{bw} is the heat transfer coefficient between the particle bed and the wall ($W/m^2 \cdot K$), and k_a is the thermal conductivity of the air ($W/m \cdot K$).

Pr is the Prandtl number:

$$Pr = \frac{\mu C_{p,a}}{k_a} \qquad \text{Eq. (37)}$$

Where $C_{p,a}$ is the specific heat of the air ($J/kg \cdot K$).

Depending on the value of the particle Reynolds number, following heat transfer coefficients were also used (A. V. Patil, Peters, & Kuipers, 2015a):

$$\begin{cases} Nu_{bw} = 5.0 + 0.05PrRe_p, & Re < 150 \\ Nu_{bw} = 0.18Pr^{1/3}Re_p^{0.8}, & Re > 150 \end{cases} \qquad \text{Eq. (38)}$$

Where Nu_{bw} is the Nusselt number for the particle bed contacted with the fluidized bed wall:

$$Nu_{bw} = \frac{h_{bw}D}{k_a} \qquad \text{Eq. (39)}$$

In the literature, there are many experimental studies and correlations for the heat transfer coefficient between the particles and the fluidized bed wall have been reported (Bao et al., 2020; Borodulya et al., 1991; Grewal & Saxena, 1980; Kim, Ahn, Kim, & Hyun Lee, 2003). But most of them are limited to a narrow range of conditions.

2.5.4 Air-particle heat transfer coefficient

When considering the heat transfer process between the air and the fluidizing particles, the heat transfer coefficient is model-dependent. Its calculated value can be greatly affected by the flow pattern of gas and of particles in the bed (Kunii & Levenspiel, 1991).

Among those models, by considering the void fraction (ε) of the particle bed, Gunn (1978) proposed a more general equation:

$$Nu_{ap} = (7 - 10\varepsilon + 5\varepsilon^2)\left(1 + 0.7Re_p^{0.2}Pr^{\frac{1}{3}}\right)$$

Eq. (40)

$$+(1.33 - 2.4\varepsilon + 1.2\varepsilon^2)Re_p^{0.7}Pr^{1/3}$$

Nu_{ap} is the Nusselt number for particles in the air:

$$Nu_{ap} = \frac{h_{ap}D}{k_a}$$

Eq. (41)

Where h_{ap} is the convective heat transfer coefficient between the air and the particles ($W/m^2 \cdot K$).

For a single particle in the air, following equation were suggested by Ranz (Ranz & Marshall, 1952) and Rowe et al. (Davidson & Harrison, 1971):

$$\begin{cases} Nu_{ap} = 2 + 0.6Re_p^{1/2}Pr^{1/3}, sphere\ particle\ falling\ through\ air \\ Nu_{ap} = 2 + 0.74Re_p^{1/2}Pr^{1/3}, single\ fixed\ particle\ in\ air \\ Nu_{ap} = 2 + 1.8Re_p^{1/2}Pr^{1/3}, large\ isometric\ particle\ in\ a\ fixed\ bed \end{cases}$$

Eq. (42)

2.6 Summary

From the literature, it is known that the Geldart type of the particles, the bed pressure drop, the minimum fluidization velocity, and the particle terminal velocity can be obtained from the properties of the particles and the air. The Geldart type of the particles and the bed pressure drop can be used to indicate the particle fluidization behaviour. The minimum fluidization velocity and the particle terminal velocity can be used to give a range of the inlet air velocity.

The thermistor probes can measure particle temperature based on the temperature dependence of electrical resistance. The thermocouple probes can measure particle temperature based on the thermoelectric effects. Both of these require direct contact with the particles and are affected by the air surrounding the particles.

The thermal camera can measure particle temperature based on the Planck's law. It is non-invasive and affected by relationship between the infrared radiation received by

the thermal camera, the infrared radiation emitted by the particles, and the particle temperature.

In terms of identifying pixels that represent the particles in the thermal images, image segmentation can be used. The technique can be used based on threshold, region, edge, neural network, and etc. Previous researchers monitored the particles in flat (2D) fluidized bed using thermal cameras. They used the threshold-based image segmentation. The disadvantage of this technique is that the threshold is selected based on human observations and it is difficult to evaluate the identification results. After identifying the pixels representing the particles in the thermal images, previous researchers correlated the intensities of the identified pixels with the particle temperature by using stationary particles outside or inside the fluidized beds.

From the literature, it is known that the particle temperature is affected by the temperatures of the air and the fluidized bed wall, the inlet air velocity, and the loaded particle mass. It is necessary to online monitor the temperatures of the air, the particles, and the fluidized bed wall separately.

The heat transfer between the particles and the fluidized bed wall is determined by the time that the particles residence on the wall. The heat transfer between the air and the particles is affected by the void fraction of the particle bed, the particle Reynolds number, and the Prandtl number.

3   Experimental setup

3.1   Particles

In this thesis, Calcium carbonate particles (CaCO$_3$, sand) were used. In order to obtain identifiable particles in the thermal images and to keep the particles as small as possible, the size of the particles were sieved to be between $1.0 \times 10^{-3}\ m$ and $1.5 \times 10^{-3}\ m$ (so that the particle diameter in the thermal images will be around 10 pixels). At $20°C$, density (ρ_p), specific heat ($C_{p,p}$), thermal conductivity (k_p) of the particles is $2600\ kg/m^3$, $840\ J/kg \cdot K$ and $1.9\ W/m \cdot K$, respectively (Kunii & Levenspiel, 1991). The particles are classified into the Geldart type D.

Figure 20 shows a microscope image of the particles. The microscope used was KEYENCE VHX-5000 with $\times$ 20 magnification. Resolution of the image is $827\ (H) \times 599\ (L)\ pixels$.

Figure 20. Calcium carbonate particles (CaCO$_3$) under microscope ($\times$ 20).

In terms of the particle irregularity, many indications can be used, such as:

$$
\begin{cases}
\dfrac{P^2}{4\pi A}, & (\text{Gray}, 1971;\ \text{Rajab et al.}, 2004) \\[2ex]
\dfrac{\sqrt{4\pi A}}{P}, & (\text{Kudo}, \text{Yasuda},\ \text{Matsusaka}, 2020) \\[2ex]
\dfrac{4\pi A}{P^2}, & (\text{Saha}, \text{Bajger},\ \text{Lee}, 2017)
\end{cases}
\qquad \text{Eq. (43)}
$$

Where A is the particle area and P is the particle parameter in the image.

In this thesis, the indication $\frac{4\pi A}{P^2}$ is used, because it can give an irregularity value between 0 and 1. It is the circularity of the particles (C). Therefore,

$$C = 4\pi A / P^2 \qquad\qquad \text{Eq. (44)}$$

In order to obtain the area and parameter of the particles in the microscope image, by observation, the threshold-based image segmentation was used. Then the pixel clusters representing the particles were obtained (Figure 21).
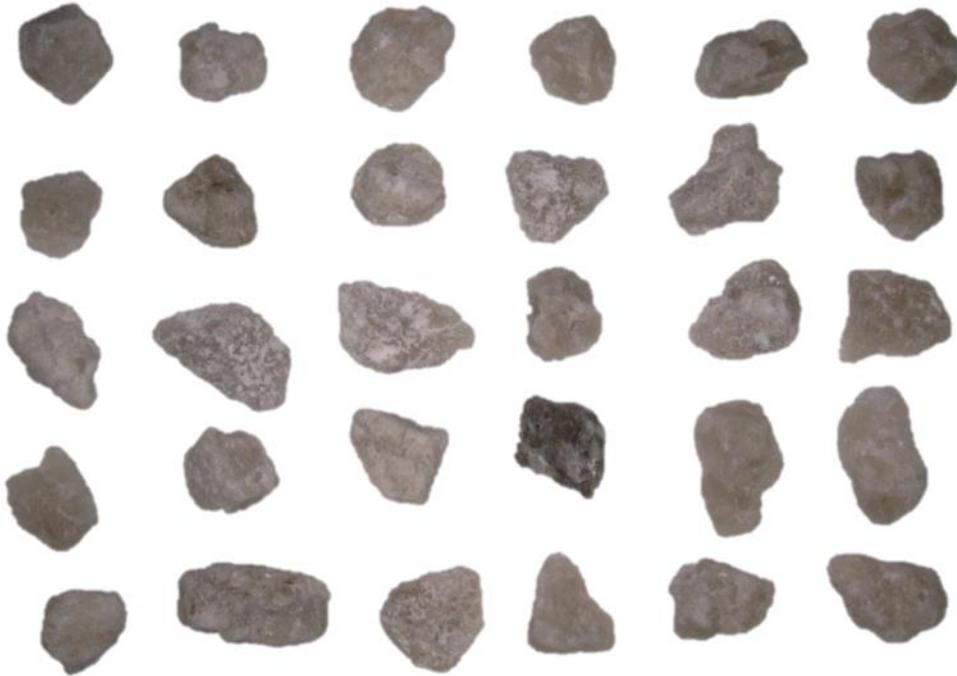
Figure 21. Pixel clusters representing the particles in the microscope image.

In the image, the particle area A is counted as the number of pixels included in a pixel cluster. The particle parameter P is counted as the total sides of the pixels, which are not connected with other pixels in the same pixel cluster.

An example is given by Figure 22. Pixel 0 is connected with pixels 1-4, so pixels 0-4 are identified as a pixels cluster. Its area (A) is the number of pixels included (i.e. 5). Its perimeter (P) is the total sides of the pixels that are not connected with other pixels in the same pixel cluster (i.e. 12). Its circularity (C) is then calculated to be around 0.44.
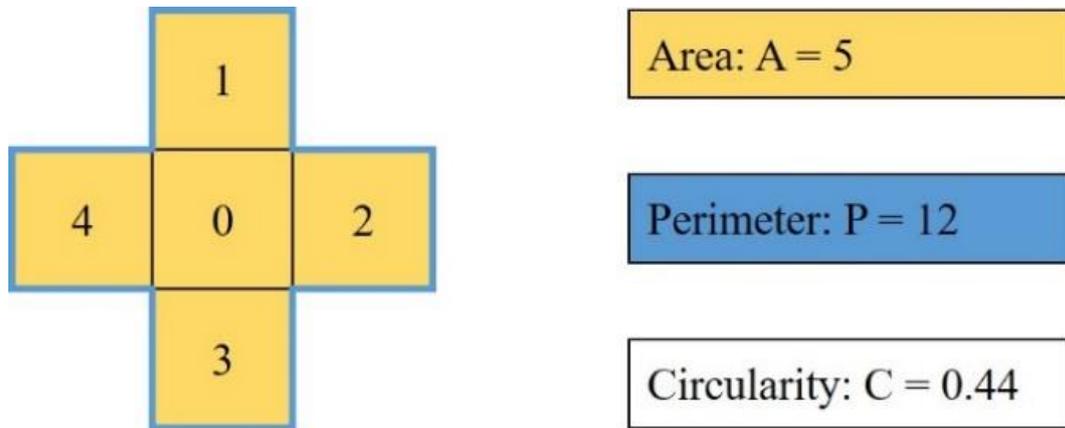
Figure 22. Example for calculating the particle size and shape.

Then the mean area and the mean circularity of the particles in the microscope image was calculated as 5337 ($\pm$1660) and 0.54 ($\pm$0.1), respectively. These values can only be used to represent the particle size and shape in the microscope image and will be different in the thermal image. This is because the image resolution and the camera lens used by the microscope and the thermal camera are different (the thermal camera will be introduced later).

3.2 Fluidized bed

The fluidized bed used was GLATT-WSG-3. It consists of two parts. Its geometry is shown in Figure 23. Height of the lower component and the higher component is 200 mm and 260 mm, respectively. Radius of the bottom circular area and the top circular area is 100 mm and 150 mm, respectively. Thickness of the fluidized bed wall is around 5 mm. Air enters from the bottom and leaves from the top. The air distributor on the bottom of the fluidized bed is made of steel with circular mesh (0.5 mm in diameter). The pressure drop across the air distributor is around 200 Pa.
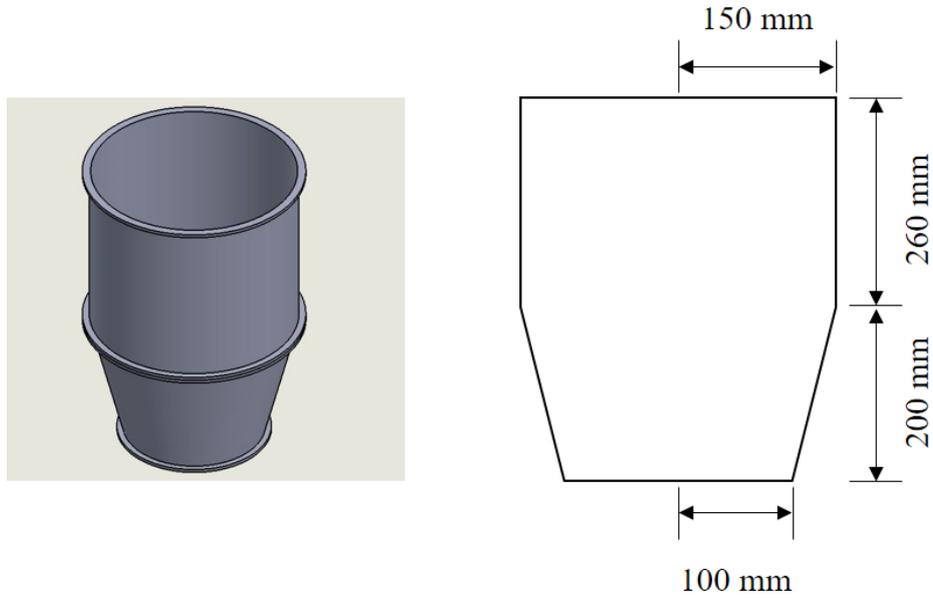
Figure 23. Dimension of the fluidized bed (GLATT-WSG-3).

At $20°C$, density (ρ_w), specific heat ($C_{p,w}$), and thermal conductivity (k_w) of the steel wall is $7800 \ kg/m^3$, $480 \ J/kg \cdot K$, and $45 \ W/m \cdot K$, respectively. Density (ρ_a), specific heat ($C_{p,a}$), thermal conductivity (k_a) and viscosity (μ) of air is $1.205 \ kg/m^3$, $1005 \ J/kg \cdot K$, $0.026 \ W/m \cdot K$ and $1.8 \times 10^{-5} \ kg/m \cdot s \ (Pa \cdot s)$, respectively (Kunii & Levenspiel, 1991). Gravitational acceleration (g) was adopted as $9.81 \ m/s^2$. It is assumed that the properties of the steel wall and the air are constant during the experiments in this thesis.

In order to fluidize the particles in this fluidized bed properly, the minimum air velocity and the particle terminal velocity need to be estimated.

By using the mean particle size ($1.25 \times 10^{-3} \ m$), the minimum air velocity can be calculated from Eq. (4), Eq. (5), and Eq. (10). The calculated value is $0.85 \ m/s$.

By using the minimum particle size ($1.0 \times 10^{-3} \ m$) and assuming the particle sphericity is 0.5, the particle terminal velocity can be calculated from Eq. (12), Eq. (13), Eq. (14), and Eq. (15). The calculated value is $3.02 \ m/s$.

Therefore, the air velocity should be higher than $0.85 \ m/s$ and lower than $3.02 \ m/s$.

In this thesis, the inlet air temperature will be increased from 30 °C to 50, 57, and 63 °C, respectively.

3.3   Thermal camera

In this thesis, a thermal camera with infrared thermal sensor was used. The thermal camera used was FLIR A655sc. The detector type is focal plane array (FPA, detectors are arranged in an array in the same plane), uncooled micro-bolometer (thermal sensor). In the thermal sensor, the detectors are arranged in $640(H) \times 480 (L)$. Same as the manner in which the thermal detectors are arranged, the entire detection area of the thermal camera can be divided into several sub-detection areas. Each thermal detector receives thermal radiation from its corresponding sub-detection area. The spectral range is $7.5 - 14 \, \mu m$, which means that only the thermal radiation with wavelength between $7.5 \, \mu m$ and $14 \, \mu m$ can be received by the detectors from the sub-detection areas. The detector pitch is $17 \, \mu m$, which means that the physical size of each detector is $17 \, \mu m$. The detector time constant is typical $8 \, ms$, which means that the time required for the thermal detector to respond to the received thermal radiation is $8 \, ms$.

When a thermal detector receives thermal radiation, it generates a signal to indicate the intensity of the received thermal radiation. The thermal radiation received from the entire detection area is then represented by a signal matrix. The unit of the signal value is called raw count in the manual of the thermal camera. The available frequency of the thermal camera is 200/100/50/25/12.5/6.25/… Hz (i.e. the number of signal matrix outputs per second). The focal length, f-number and minimum focus distance of the thermal camera lens used was respectively $24.6 \, mm$, 1.0 and $250 \, mm$. The instantaneous field of view (IFOV) was $0.68 \, mrad$.

The output signal matrix from a thermal camera can be visualized as a thermal image. Since the visualization is an artificial process, the thermal image could be a grey scale image (the colour of a pixel is represented by a grey value and varied from 0 to 255, where 0 is the black and 255 is the white), a RGB image (the colour of a pixel is represented by red, green and blue values) or other image formats.

The visualization can be expressed as:

$$I_{xy} = f(S_{xy}) \hspace{4cm} \text{Eq. (45)}$$

52

Where I_{xy} represents a pixel in the thermal image with coordinate (x, y) and colour value $I(x, y)$, and S_{xy} represents an element in the signal matrix with coordinate (x, y) and signal value $S(x, y)$.

In this thesis, MATLAB R2018b was used to write the programs.

The signal matrix S obtained from the thermal camera was visualized as a grayscale thermal image (represented by I, range of the grey value is $0 - 255$, where 0 and 255 is the black colour and white colour, respectively) using the following equation:

$$I_{xy} = 255 \times (S_{xy} - S_{min})/(S_{max} - S_{min})$$ Eq. (46)

Where I_{xy} represents a pixel in the thermal image with coordinate (x, y) and colour value $I(x, y)$, S_{xy} represents an element in the signal matrix with coordinate (x, y) and signal value $S(x, y)$, and S_{min}, S_{max} are the minimum and maximum value in the signal matrix S, respectively.

When a thermal image is obtained using a thermal camera, the pixel size can be estimated by (Budzier & Gerlach, 2011):

$$l_{pixel} = 2L \tan\frac{IFOV}{2}$$ Eq. (47)

Where l_{pixel} is the pixel size, L is the distance between the focused plane and the lens, and $IFOV$ is the instantaneous field of view.

In this thesis, in order to minimize the pixel size so that more pixels can be occupied by a particle in the thermal images, the minimum focus distance of the thermal camera was used.

Then the distance between the focused place and the lens was calculated as:

$$\begin{aligned} L &= (minimum\ focus\ distance - focal\ length) \\ &= 250 - 24.5 = 225.5\ mm \end{aligned}$$ Eq. (48)

Using the Eq. (47),

$$l_{pixel} = 2L \tan\frac{IFOV}{2} \approx 0.15\ mm$$ Eq. (49)

Then the particle diameter in the unit of pixels can be evaluated as:

$$\begin{cases} D_{\min\_pixel} = \dfrac{D_{min}}{l_{pixel}} = \dfrac{1.0\ mm}{0.15\ mm} \approx 7\ pixels \\ D_{\max\_pixel} = \dfrac{D_{max}}{l_{pixel}} = \dfrac{1.5\ mm}{0.15\ mm} \approx 10\ pixels \end{cases} \qquad \text{Eq. (50)}$$

Where D_{min} is the minimum particle diameter (m) and D_{max} is the maximum particle diameter (m).

However, due to the errors (such as the system error, installation error and etc.), the range of the particle diameter in the unit of pixels does not have much value. It should only be used as an expectation of the thermal image quality.

Strictly, during the detector time constant $(8\ ms)$, if a monitored object moved more than a pixel in the direction horizontal to the thermal camera, it will be blurry in the thermal image. The maximum velocity required for the particles to be clear in the thermal image (U_{mc}) can be calculated as:

$$U_{mc} = \frac{1\ pixel}{8\ ms} = \frac{0.15\ mm}{8\ ms} \approx 0.02\ m/s \qquad \text{Eq. (51)}$$

Therefore, due to the particle fluidization in a fluidized bed, it is expected that most of the particles in the thermal images are blurry. In order to measure the temperature of the fluidizing particles accurately using a thermal camera, the effect of the blurry particles on the temperature measurement must be considered.

3.4 Installation

In order to use the thermal camera to monitor the particles in a fluidized bed, an Infrared (IR) window is needed. Since the spectral range of the thermal camera is $7.5 - 14\ \mu m$ and germanium has a uniform transmission percentage (around 46%) in the range, the material of the IR window was selected to be germanium coated with diamond (a thin layer for protection, its transmission is higher than $90\ \%$ in the range). The IR window was circular with a radius of $30\ mm$.

The setup of the experiment is shown in Figure 24. The thermal camera was placed $250\ mm$ from the centre of the fluidized bed to monitor the fluidizing particles using its minimum focus distance. Height of the thermal camera was $85\ mm$ from the

bottom of the fluidized bed. The IR window was fitted on the fluidized bed, $100\ mm$ from the thermal camera and $150\ mm$ from the centre of the fluidized bed. Four K-type thermocouple probes (temperature range is $-75°C$ to $+260°C$, accuracy is $\pm\ 2.5°C$, calibrated in advance) were used to measure the temperatures of the inlet air, the ambient, the fluidized bed wall and the exit air. In terms of the calibration, the four thermocouple probes were placed in a water bath (Stuart SWB3D Digital Water Bath) and temperatures of the probes were recorded every 1 second. The water was then heated from 20 °C to 90 °C and cooled from 90 °C to 20 °C (repeated three times). By comparing the temperatures measured by the four probes, it was concluded that the probes were consistent.

The thermocouple probe measuring the inlet air was placed slightly above the air distributor and covered by a steel mesh, so that the probe contacted neither with the air distributor nor the particles. The thermocouple probe measuring the fluidized bed wall was placed outside and $85\ mm$ from the bottom of the fluidized bed. The thermocouple probe measuring the ambient was $100\ mm$ from the fluidized bed wall. The thermocouple probe measuring the exit air was in the centre of the fluidized bed and $300\ mm$ from the bottom. The average inlet air velocity can be measured before the air distributor of the fluidized bed by an air velocity meter (TSI 9545-A).
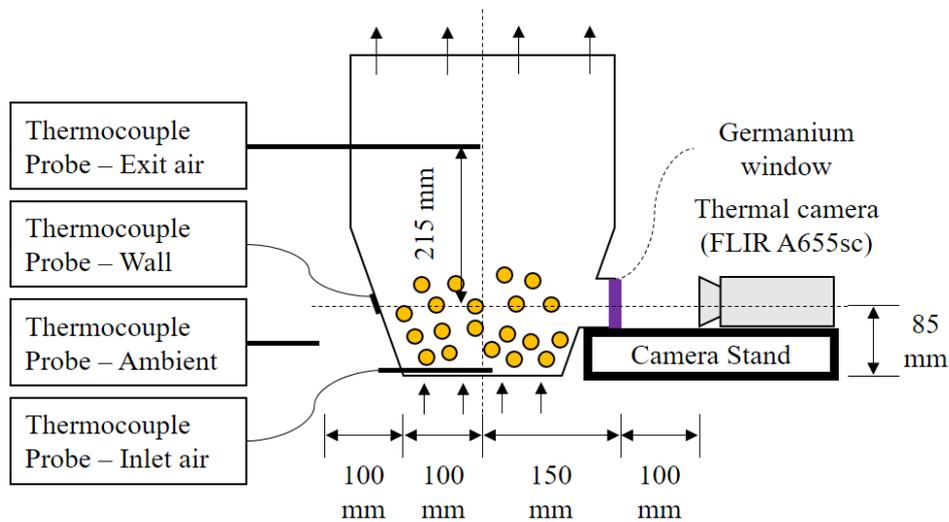
Figure 24. Experimental setup.

Since height of the thermal image is $640\ pixels$, the distance between the thermal image bottom and the fluidized bed bottom ($H_{image-distributor}$) is estimated as:

$$H_{image-distributor} = 85\ mm - \frac{640 \times l_{pixel}}{2}\ mm = 37\ mm \qquad \text{Eq. (52)}$$

Figure 25 shows three images visualized from the signal matrices ($1400\ g$ particles were fluidized using $57°C$ and $2.0\ m/s$ inlet air velocity). From the figure, it can be observed that when a thermal camera is used to monitor the particles in a fluidized bed, both the particles and the fluidized bed wall are in the thermal images. The particles are present individually or in contact with other particles. It can be seen that some of the particles are clear, while others are blurry. Due to the fluidization, the number of the pixels representing the clear and blurry particles in the thermal images varies over time.
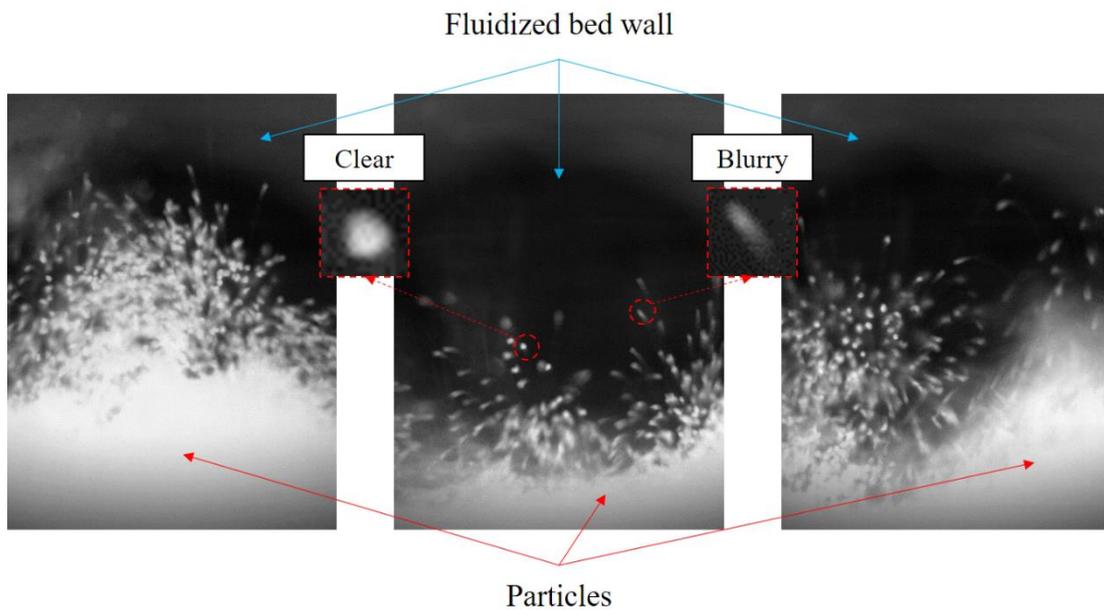
Figure 25. Example of the thermal images.

3.5   Summary

In this thesis, calcium carbonate particles in the Geldart group D were fluidized in a cylindrical 3D fluidized bed. The area and circularity of the particles in the microscope image were calculated.

Based on the properties of the particles and the air, the minimum fluidization velocity and the particle terminal velocity were also calculated. It is known that the air velocity should be roughly between $0.85\ m/s$ and $3.02\ m/s$.

In the setup of the fluidized bed, temperatures of the inlet air, the exit air, the fluidized bed wall, and the ambient can be online monitored by four K-type thermocouple probes. The particles can be online monitored by a thermal camera (FLIR A655sc).

The number of pixels that will be occupied by a particle in the thermal image was evaluated. The maximum velocity of a particle that would cause it blurry in the thermal image was calculated. It is expected many particles will be blurry in the thermal image and their effect on the particle temperature measurement must be considered.

4 Particle identification

4.1 Pixels representing the blurry particles

When using a thermal camera to online monitor the fluidizing particles, some of the particles in the thermal images are clear, while others are blurry.

One of the reason that cause the particles is the focus of the thermal camera. As shown in Figure 26, the blue outlines is real particle, and orange squares is the pixels representing the particle in the thermal image. When the particle is in focus of the thermal camera, the pixel cluster representing the particle in the thermal image will be similar to the actual particle that should be reflected the thermal image. When the particle is out focus, the pixel cluster representing the particle in the thermal image will be bigger (the particle is closer to the thermal camera) or smaller (the particle is further to the thermal camera) than it should be. In the meanwhile, the intensities of the pixels will also be affected.

| In focus | Out focus (closer) | Out focus (further) |
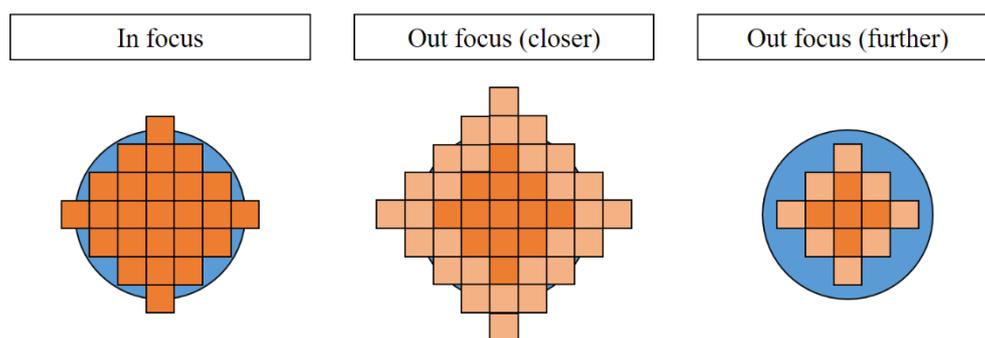
Figure 26. Blurry particles caused by the focus of the thermal camera.

Another reason that cause the blurry particles is the movement of the particles. As shown in Figure 27, when the particle was not moved during the time that the thermal image was taken (i.e. its velocity was $0\ l_{pixel}/t_{constant}$, where l_{pixel} is the pixel size and $t_{constant}$ is the detector time constant), the pixel cluster representing the particle in the thermal image will be similar to the actual particle that should be reflected the thermal image. When the particle was moved during the time that the thermal image was taken, the pixel cluster representing the particle in the thermal image will be stretched and more irregular than the real particle. In the meanwhile, the intensities of the pixels will also be affected. For example, if the particle velocity (U_p) was $1\ l_{pixel}/t_{constant}$, the pixel cluster representing the particle in the thermal image will be stretched for one pixel in the direction of the particle velocity. The intensities of

the pixels in the front and end of the pixel cluster will be affected. If the particle velocity was $D\ l_{pixel}/t_{constant}$ (D is the particle diameter), the pixel cluster representing the particle in the thermal image will be stretched for $\frac{D}{l_{pixel}}$ pixels in the direction of the particle velocity. The intensities of all the pixels in pixel cluster will be affected.
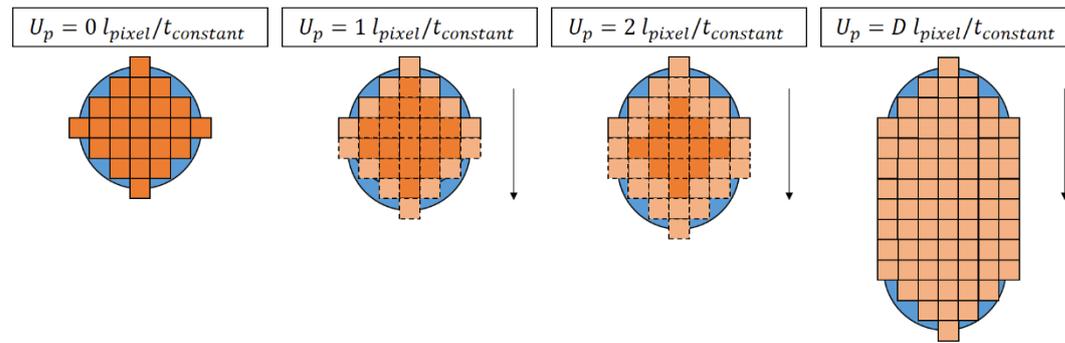
Figure 27. Blurry particles caused by the movement of the particles.

In order to identify the pixels that not only represent the particles but also have the same relationship between the signal value (S_{xy}^*) and the particle temperature (T_{xy}^*), it is necessary to compare the corresponding signal values of the pixels representing the clear and blurry particles.

4.1.1 Focus of the thermal camera

As shown in Figure 28, an experiment was designed to compare the corresponding signal values of the pixels representing clear and blurry particles that are caused by the focus of the thermal camera. In this experiment, a particle was placed on a hot plate (STUART US152), the temperature of which was $50°C$. The thermal camera (FLIR A655sc) was used to monitor the particle. The focus distance of the thermal camera was fixed to its minimum focus distance ($250\ mm$). The distance between the thermal camera and the particle was varied from 230 to 270 mm.
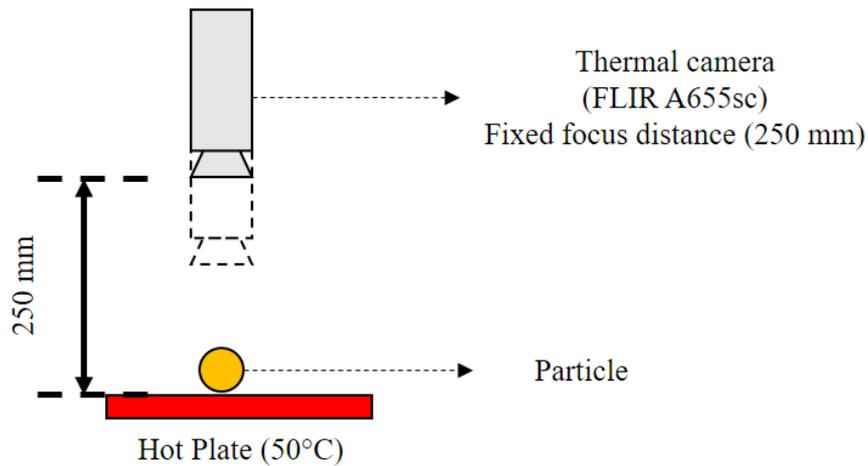
Figure 28. Blurry particle caused by the focus of the thermal camera (experimental setup).

The signal matrices obtained from the thermal camera were visualized using the Eq. (46) and shown in Figure 29.
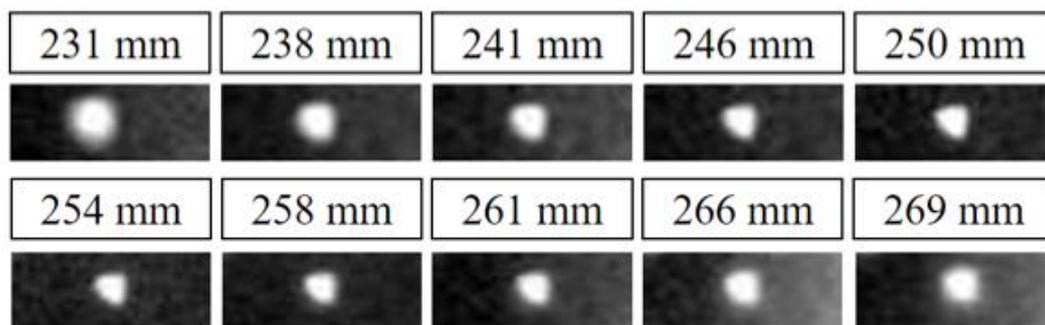
Figure 29. Blurry particle caused by the focus of the thermal camera (thermal images).

From the thermal images, it can be observed that when the distance between the thermal camera and the particle was $250 \, mm$ (i.e. focused), the particle was clear. When the distance was greater or less than $250 \, mm$ (i.e. unfocused), the particle was blurry. It can also be observed that when the particle was unfocused, its size in the thermal image was increased and its shape was closer to a circle.

The corresponding signal value of the pixels representing the particle was picked manually from the centre of the particle. This experiment was repeated five times and the results were shown Figure 30.
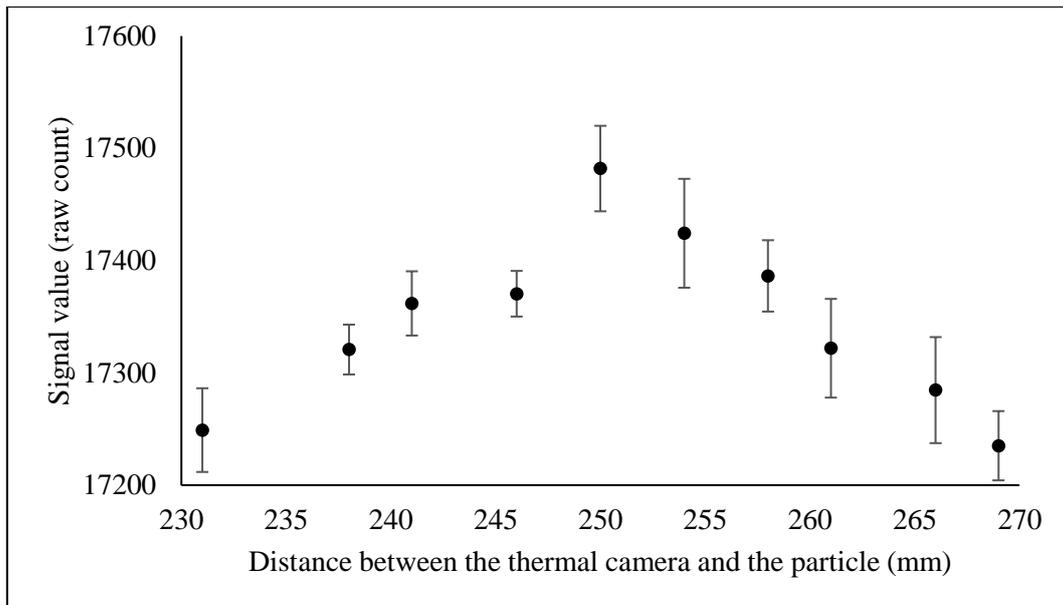
Figure 30. Blurry particle caused by the focus of the thermal camera (signal value).

From the results, it can be observed that when the particle was focused (clear), the signal value was maximized. When the released time was unfocused (blurry), the signal value was decreased. Since the particle temperature was not changed, it is then concluded that for pixels representing the focused and unfocused particles in the thermal images, the relationship between their corresponding signal value and the particle temperature is not the same.

4.1.2   Movement of the particles

As shown in Figure 31, an experiment was design to compare the corresponding signal values of the pixels representing clear and blurry particles that are caused by movement of the particles. In this experiment, a particle was hold by a tweezer and focused by the thermal camera (FLIR A655sc) using its minimum focus distance ($250\ mm$). A steel plate uniformly heated by hot air was placed $500\ mm$ behind the particle as a background. Temperature of the steel place was measured by a thermocouple probe (approximately $50°C$).
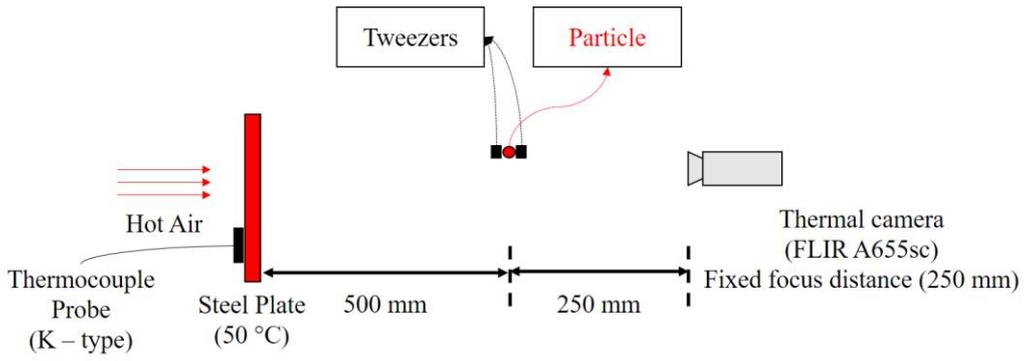
Figure 31. Blurry particle caused by the movement of the particle (experimental setup).

After the thermal camera was started to monitor the particle using $200\ fps$, the particle was released from the tweezer. Then longer falling time can lead to faster particle movement. Since the particle falls rapidly, it is assumed that the particle temperature does not change before and after being released. The signal matrices obtained from the thermal camera were visualized using the Eq. (46) and shown in Figure 32.
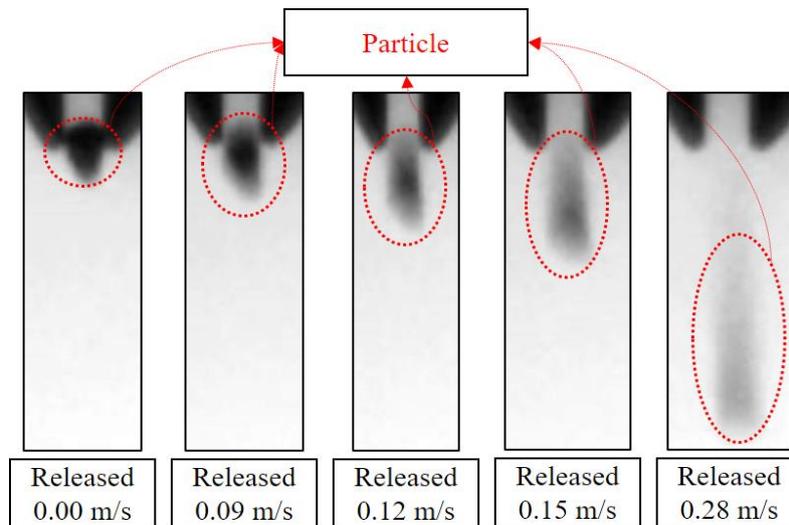
Figure 32. Blurry particle caused by the movement of the particle (thermal images).

In the images, the particle velocity (U_p) was calculated using the following equation:

$$U_p = \sqrt{2g\left(H_{falling}\,l_{pixel}\right)} \qquad \text{Eq. (53)}$$

Where g is the gravitational acceleration (m/s^2), $H_{falling}$ is the falling height of the particle in the unit of pixels, and l_{pixel} is the length of a pixel (m). The value of l_{pixel} was calculated in the section 3.3.

The corresponding signal value of the pixels representing the particle was picked manually from the centre of the particle. This experiment was repeated five times and the results were shown in Figure 33.
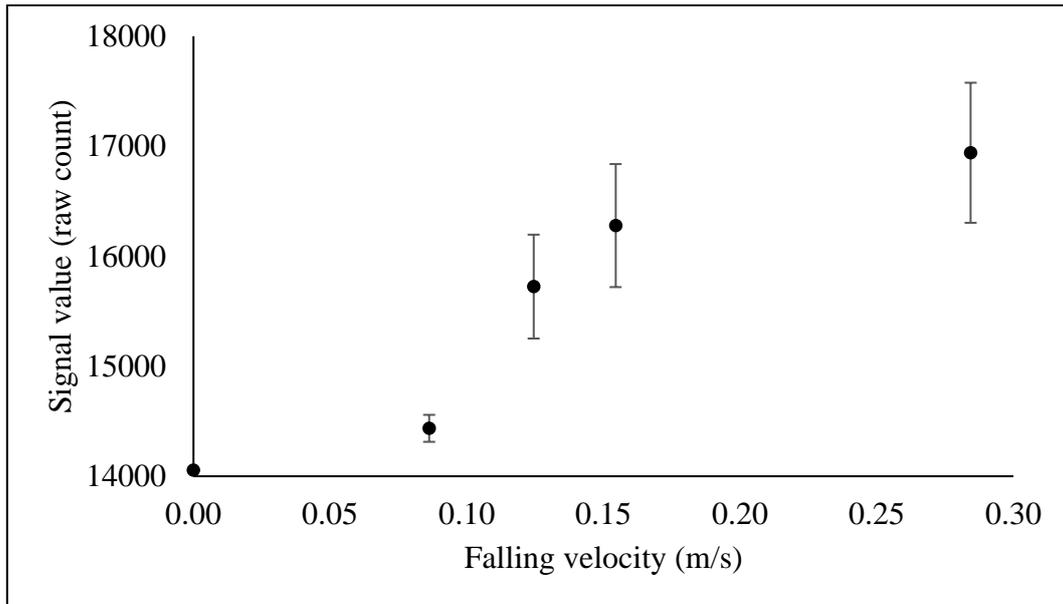
Figure 33. Blurry particle caused by the movement of the particle (signal value).

From the results, it can be observed that when the particle was not released (clear), the signal value was minimized. When the released time was increased (blurry), the signal value was also increased. Since the particle temperature was not changed, it is then concluded that the movement of the particles can affect the relationship between the signal value of the pixel cluster and the temperature of the particle represented by the pixel cluster.

4.2   Threshold-based image segmentation

Threshold based image segmentation can divide an image into multiple groups of pixels based on the pixel grey values. It is a widely used and fast computational method. In this method, single threshold or multiple thresholds can be selected. The distribution of the pixel grey values in the example thermal images are shown in

Figure 34. From the figure, it can be observed that the pixel grey values are continuously distributed and have several peaks and troughs.
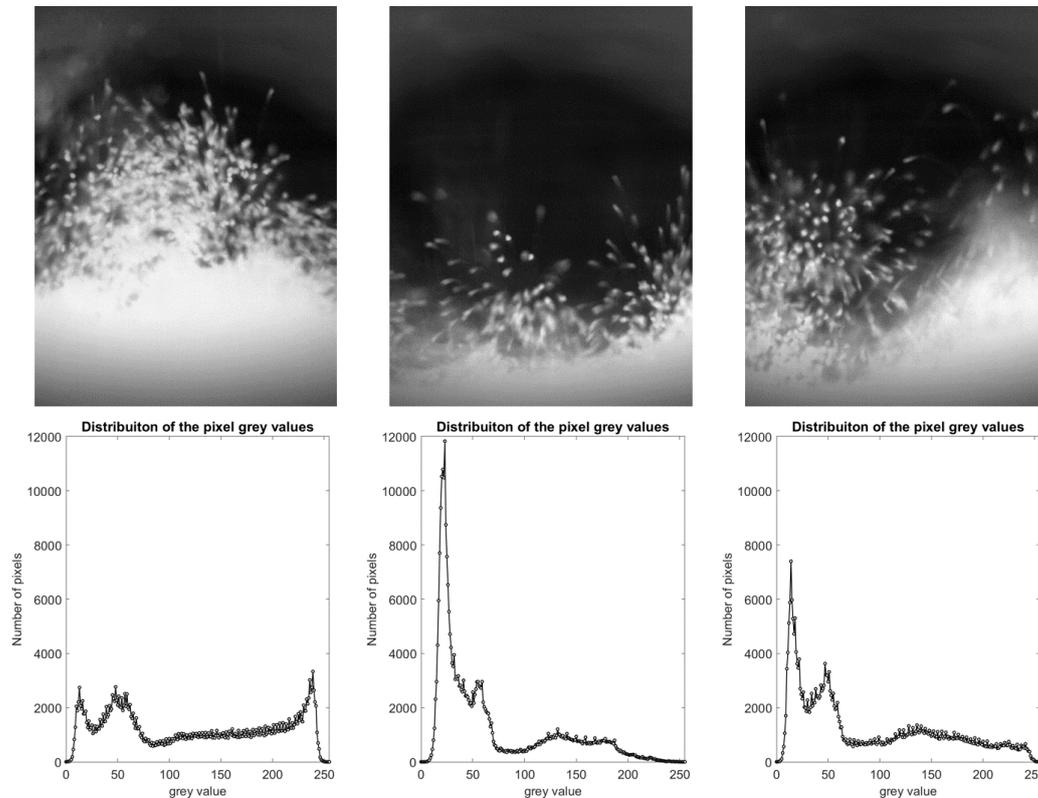
Figure 34. Distribution of the pixel grey values in the thermal images.

Ideally, if a value exist that can significantly separate the distribution of the pixel grey values into two classes, the value can be used as a threshold to segment the thermal image (pixels having grey value higher than the value represent the particles, and pixels having grey value lower than the value represent the fluidized bed wall).

4.2.1 Single-threshold method

When the single-threshold method is used, in the thermal images, pixels that represent the particles are pixels whose grey values are above or below the selected single threshold. For example, in Figure 35, pixels whose grey values are greater than 0, 25, 50, 75, 100, 125, 150, 175, 200, 225 and 250 were displayed in red colour. From the thermal images, it can be observed that when the selected single threshold was close to 0, more pixels representing the fluidized bed wall were included in the identified pixels. When the selected single threshold was close to 255, more pixels representing the particles were excluded from the identified pixels.
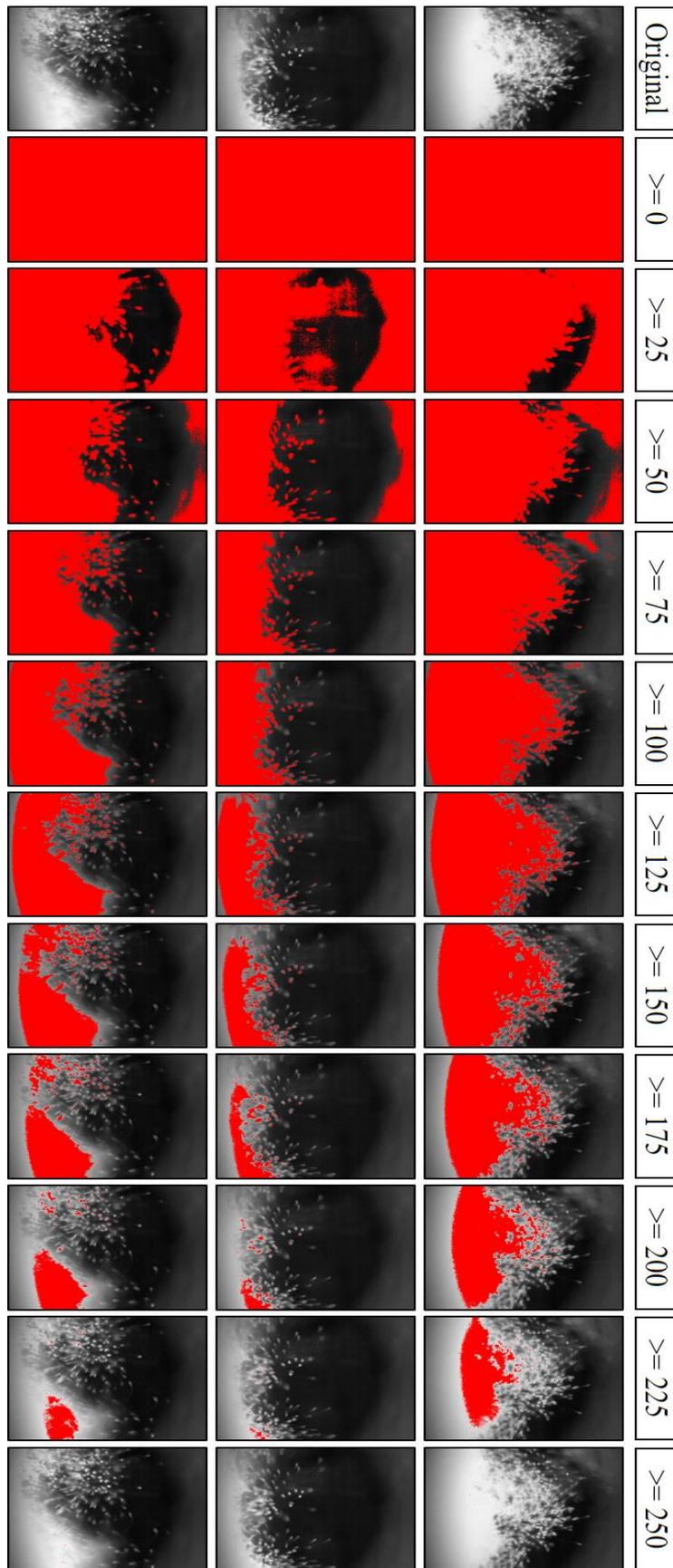
Figure 35. Pixels whose grayscale values are above the selected single threshold (Red colour).

By observation, when the threshold was between 75 and 175, within the identified pixels, most of the pixels were representing the particles (details are shown in Figure 36).
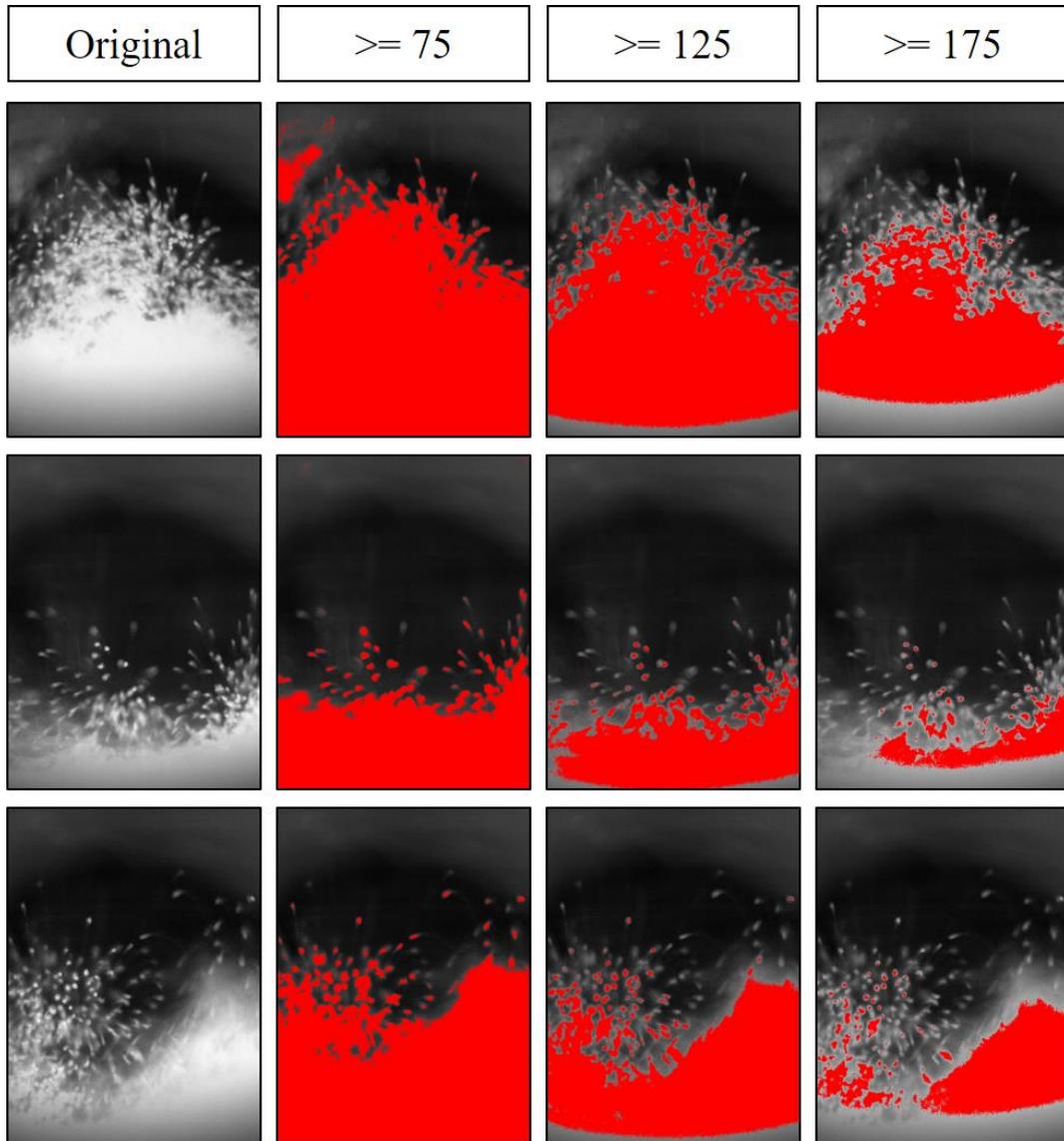
Figure 36. Pixels whose grayscale values are above 75, 125 and 175 (Red colour).

From the Figure 36, it can be observed that using different grey value between 75 and 175 as the single threshold can result in different number of pixels representing the clear and blurry particles.

Although a variety of methods (for example, the Otsu's method (Otsu, 1979) and the trial and error method (Li et al., 2017; A. V. Patil, Peters, Sutkar, et al., 2015; Sutkar et al., 2015)) can be used to select a grey value as the single threshold, it is not possible to consider whether the particles are clear or blurry in the thermal images.

Therefore, for the identified pixels that represent the particles, the relationship between their corresponding signal values and the particle temperature is different. This is the uncertainty caused by the single threshold method. Due to the fluidization of the particles, the complexity of the thermal images changes over time, which can exacerbate the uncertainty when online monitoring the particle temperature.

4.2.2 Multi-threshold method

When the multi-threshold method is used, in the thermal image, the pixels that represent the particles are pixels whose grey values are between the selected multiple thresholds.

In Figure 37, the pixels whose grey values are within several grey value ranges (0-50, 50-100, 100-150, 150-200 and 200-255) were displayed in red colour. It can be seen from the figure that the grey values of the pixels representing the same particle could be within different grey values ranges. The ranges that include the grey value of the pixels representing the clear and blurry particles were not the same.
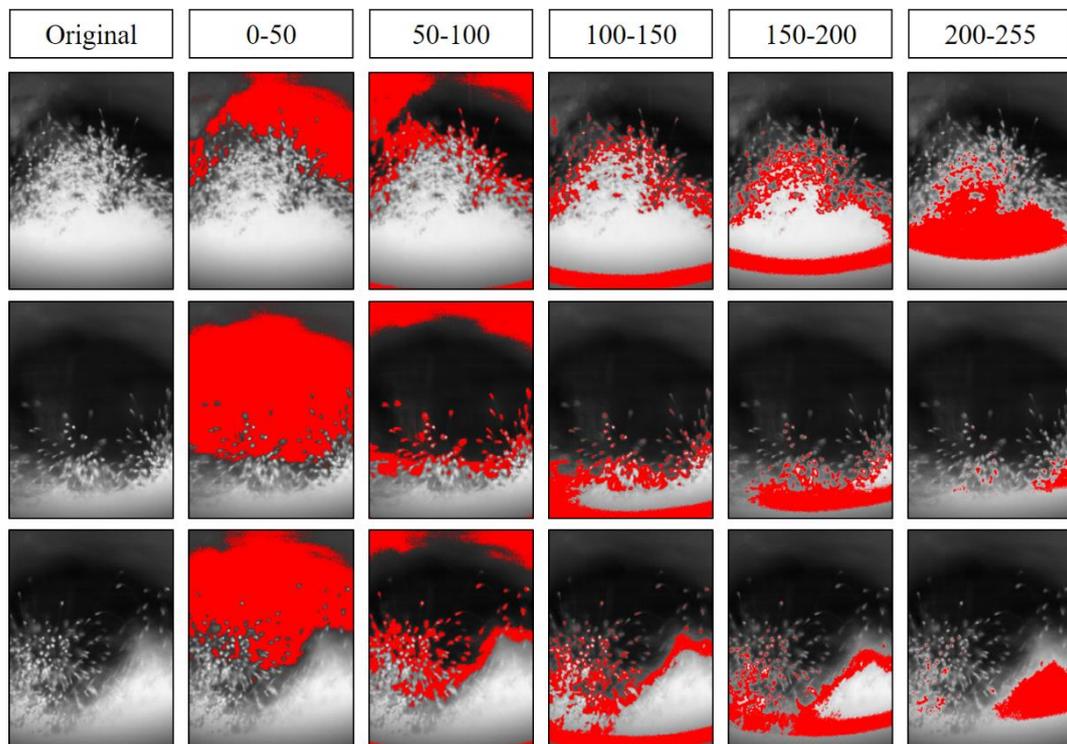
Figure 37. Pixels whose grayscale values are between the selected thresholds (Red colour).

This multi-threshold method is also not possible to consider whether the particles are clear or blurry in the thermal images. The selection of the thresholds, the blurry

particles in the thermal images and the fluidization of the particles can cause uncertainty when the online monitoring the particle temperature. Therefore,

4.3 Region-based image segmentation

From the previous section, it can be found that using the threshold-based image segmentation is not able to accurately monitor the particle temperature online. Since the particle size and shape can be used for the pixel identification to filter the blurry particles, the region-based image segmentation was used in this thesis.

In order to identify the pixels that represent the particles in the thermal images based on their particle size and shape, they must be calibrated first. Due to the influence of the thermal camera focus and the particle movement, it is difficult to calibrate the particle size and shape online. Therefore, an offline calibration experiment is designed.

4.3.1 Offline calibration of the particle size and shape

The experimental setup is shown in Figure 38. One hundred particles were place separately in an array (10×10) on the germanium window 1, so that the particle number is known and the thermal radiation emitted from the background can be controlled. The thermal camera was placed above the particles to monitor them using its minimum focus distance ($250 \ mm$). The frame rate used was 1 fps. The germanium window 2 was placed between the particles and the thermal camera, the same setup as in the fluidized bed experiment (Figure 24). A water sink was placed on a hot plate and under the particles as a controllable background. The advantage of using a water sink is that a background having lower temperature than the particles can be created by adding ice. Compress air was used to prevent the generation of mist on the germanium window 1. Temperature of the germanium window 1 was measured using a K-type thermocouple probe (approximately $25°C$). It is assumed that the germanium window and the particles on it have the same temperature.
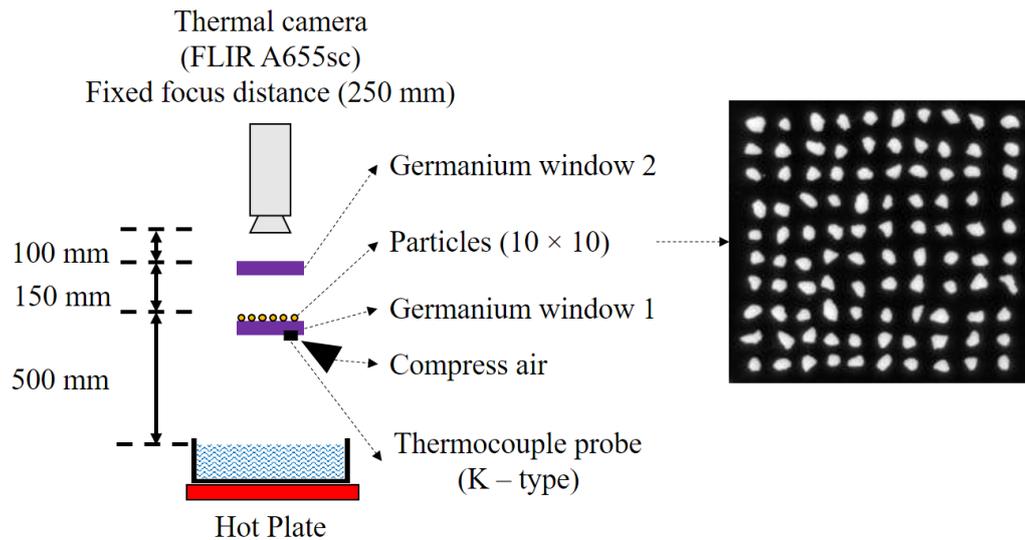
Figure 38. Calibration of the particle size and shape (experimental setup).

In this experiment, temperature of the water was increased from $0°C$ to $70°C$. Then, the effect of the signal difference between the particles and the background on the particle size and shape was taken into consideration.

Signal matrices obtained from this experiment was first converted to thermal images. In the thermal images, it is necessary to identify the pixels that represent the particles. From the experimental setup, it is known that the number of the pixel clusters representing the particles is one hundred and the number of the pixel clusters representing the background is one. Then it is expected that an appropriate threshold (a grey value) should separate the image into two parts, one of which contains only one pixel cluster that represent the background and the other contains one hundred pixel clusters that represent the particles. However, there are more than one threshold can do the job. It is still needed to select one from all of the threshold as the most appropriate threshold.

In order to do so, any grey value (I_n) that meet the following conditions were obtained at first:

i.   Pixels having grey value less than I_n can be divided into 100 (or 1) pixel clusters based on their connectivity.
ii. Pixels having grey value greater than I_n can be divided into 1 (or 100) pixel clusters based on their connectivity.

The 100 and 1 pixel clusters were respectively indicating the number of the particles and the background in the thermal images.

Among the obtained grey values, an optimal threshold (I_{otsu}) can be obtained using the Otsu's threshold method (Otsu, 1979). Using this threshold, the pixels in the thermal images were separated into two classes (class 1, pixels having grey value less than I_{otsu}; class 2, pixels having grey value greater than or equal to I_{otsu}). Figure 39 shows several examples.

In the figure, the difference between the maximum and the minimum values within the signal matrix was adopted as the absolute signal difference between the particle and the background. When the 100 pixel clusters were included in the pixel class 1, the signal difference was negative, and vice versa.

It can be also observed from the figure that when the signal difference between the particles and the background was between - 249 and 241, pixels representing the particles cannot be identified in the thermal images.
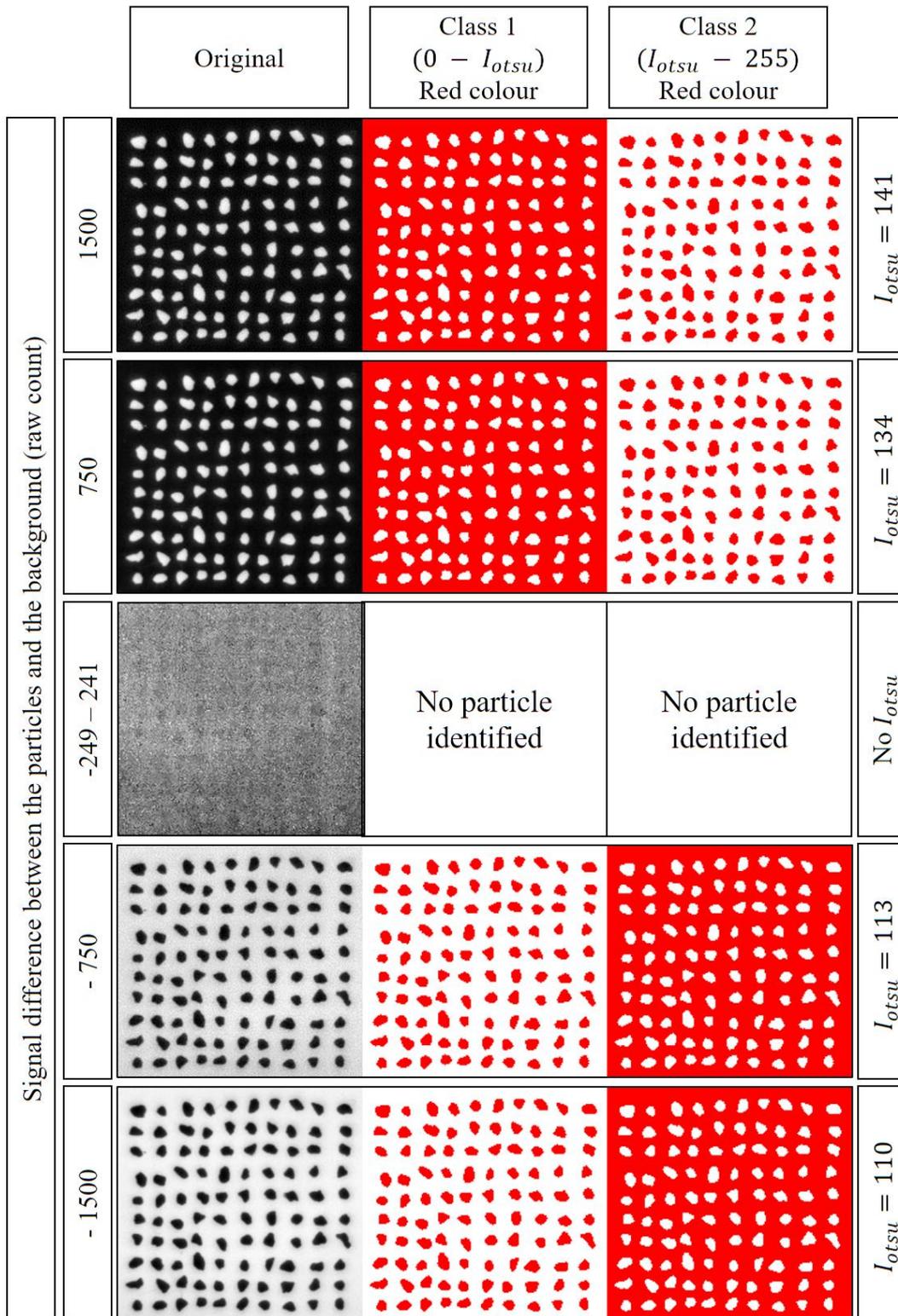
Figure 39. Calibration of the particle size and shape (pixel classes from the thermal images).

Using the method introduced in the section 3.1, the area and circularity of the pixel clusters that represent the particles in the thermal images can be obtained. Figure 40 shows the cumulative distribution of the particle area and circularity. From the figure,

it can be seen that as long as the particles can be identified, their area and circularity were not affected by the signal difference between the particles and the background. The particle area (A) was approximately between 40 (A_{min}) and 100 (A_{max}) pixels. The particle circularity (C) was approximately between 0.4 (C_{min}) and 0.65 (C_{max}).
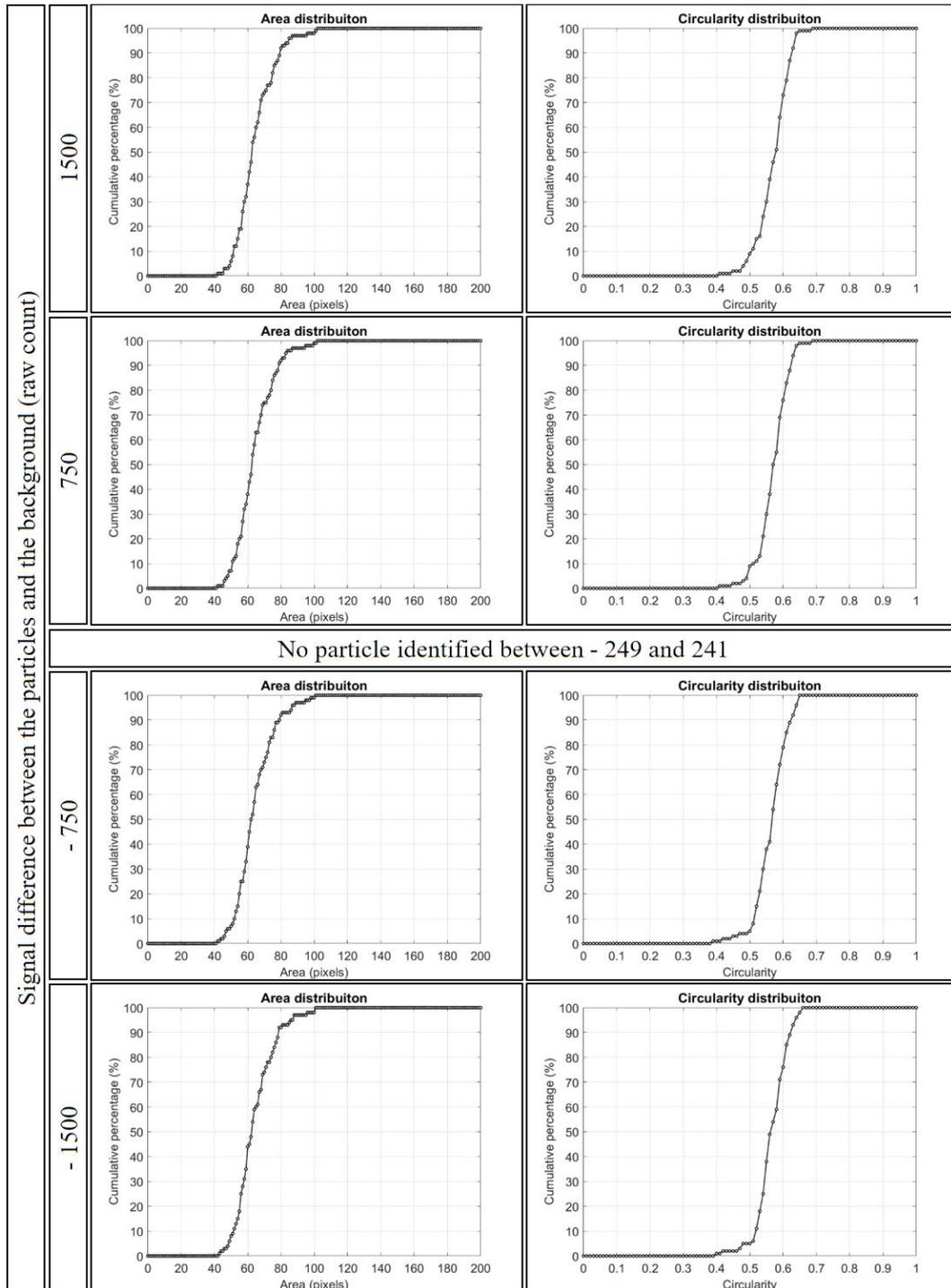
Figure 40. Calibration of the particle size and shape (cumulative distribution).

Based on these two offline calibrated ranges, the pixels representing the particles in the thermal images obtained from the online monitoring process of the fluidized bed can be identified.

4.3.2   Online identification of the particles in the thermal images

In this thesis, a procedure was developed for the online identification. The primary step is using a grey value (I_n) to divide the pixels in the thermal images in two classes (class 1, pixels having grey value less than I_n; class 2, pixels having grey value greater than or equal to I_n). By changing the I_n from 0 to 255, there are 512 (2*256) pixel classes can be obtained. Figure 41 shows three examples, where the I_n was equal to 75, 125 and 175, respectively. In the figure, the red areas within the blue frames were the pixels within the classes.

Within each pixel class, the pixels were separated into multiple clusters based on their connection in four directions (up, down, right and left). Then the area (A) and circularity (C) of the pixel clusters can be obtained.

In the thermal images, when a pixel cluster was representing a clear particle, its area A and circularity C would be respectively between A_{min} and A_{max}, and between C_{min} and C_{max}. When a pixel cluster was representing a blurry particle, or contacted multiple particles, its area and circularity would be respectively out of the ranges. Therefore, the pixel clusters representing the clear particles can be obtained from the pixel classes (the red areas within the green frames in the Figure 41). After all the pixel classes had been processed, the identified pixels in all classes (512) were summarised. Then these pixels was the final identified pixels (an identified pixel is denoted as I_{xy}^*) that represent the clear particles in the thermal image. From the figure, it can be observed that using above procedure, pixels representing the individual and clear particles in the thermal images were identified successfully.
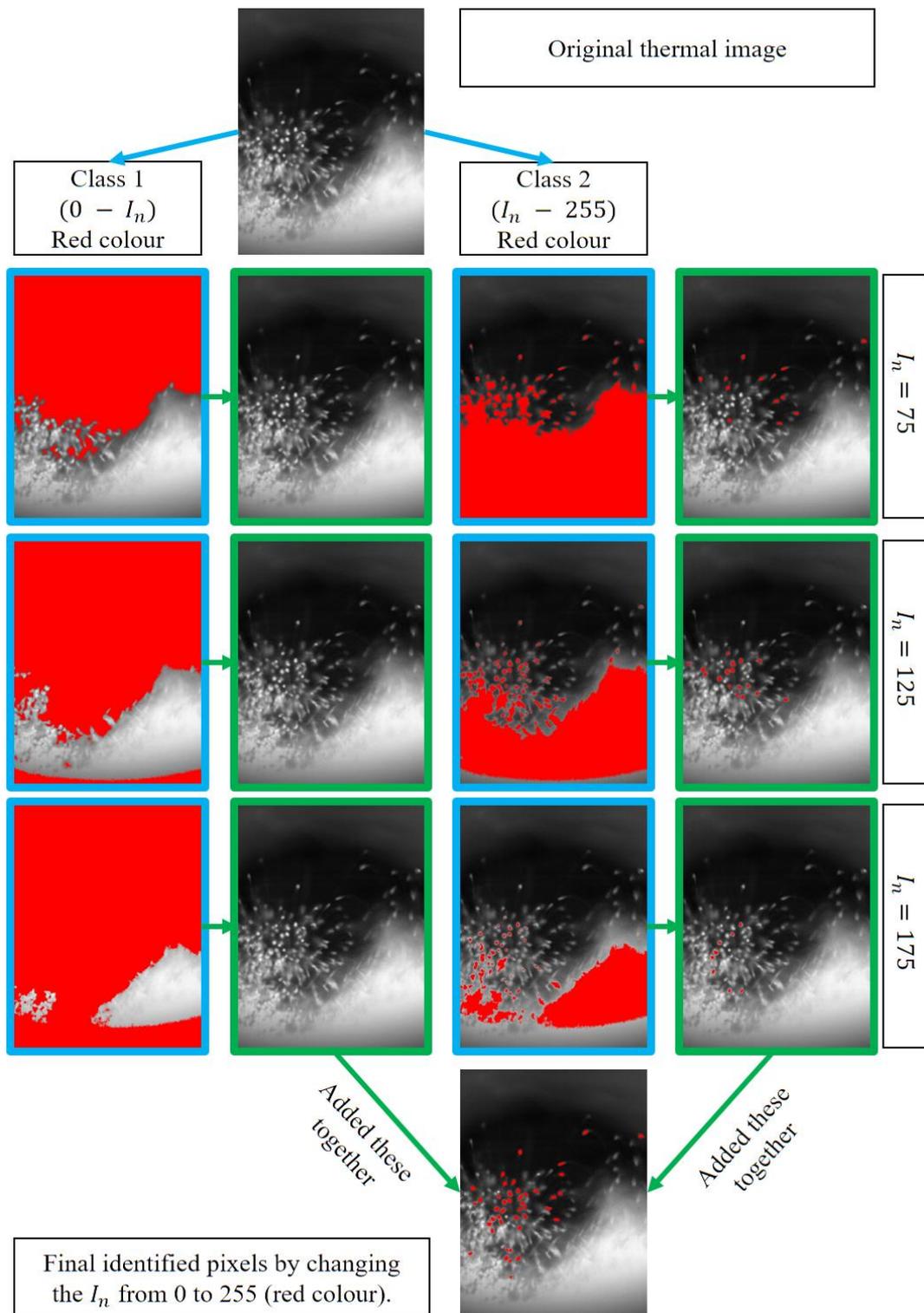
Figure 41. Online identification procedure.

4.4   Summary

By designing two experiments, it is found that when a thermal camera is used to monitor a particle with a constant temperature, the signal value of the particle (indicating the received infrared radiation from the particle) can be affected by the

focus of the thermal camera and the movement of the particle. When a particle is focused by the thermal camera and does not move, it is clear in the thermal image. Otherwise, the particle is blurry in the thermal image. The size and shape of the pixel clusters representing the clear and the blurry particles are different.

The threshold – based image segmentation cannot distinguish the clear and blurry particles, it is not able to accurately monitor the particle temperature online.

Therefore, an improved image segmentation based on the particle size and shape in the thermal images was developed in this thesis. By using an offline calibration method, the size and shape of the particles in the thermal images were measured and it is found that they are not affected by the signal difference between the particles and their background.

By using developed the region-based image segmentation, in the thermal images that were obtained online, the pixels representing the individual and clear particles in the thermal images were identified. It is believed that the signal value corresponded to the identified pixels and the particle temperature have the same relationship.

5 Particle temperature calibration

5.1 Effect of the air temperature

When hot inlet air is introduced into the fluidized bed, it also emits thermal radiation. Therefore, it is necessary to determine whether the thermal radiation emitted from the hot air will affect the relationship between the signal values corresponding to the identified pixels and the particle temperature. Following experiment was designed Figure 42.
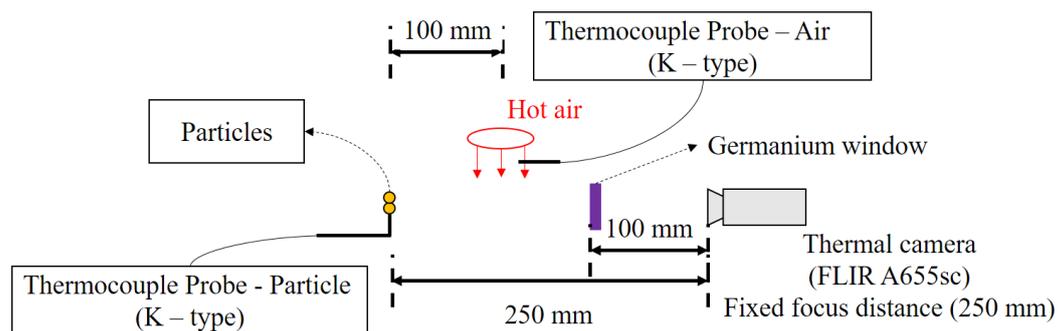
Figure 42. Effect of hot inlet air on the relationship between the signal values corresponding to the identified pixels and the particle temperature (experimental setup).

As shown in the figure, several particles were fixed on the tip of a K-type thermocouple probe. The thermal camera was used to monitor the particles at its minimum focus distance ($250\ mm$). A germanium window was placed between the particles and the thermal camera, the same setup as in the fluidized bed experiment (Figure 24). A hot air gun was used to blow hot air between the particles and the thermal camera. Distance between the heat gun and the particles was $100\ mm$. Temperature of the hot air was measured using a K-type thermocouple probe.

In this experiment, temperature of the hot air was increased from 25 to $400°C$. In the meanwhile, the average particle temperature was around $23.6°C$ during the process. The signal value of the particles measured using the thermal camera was plotted against the air temperature, as shown in Figure 43.
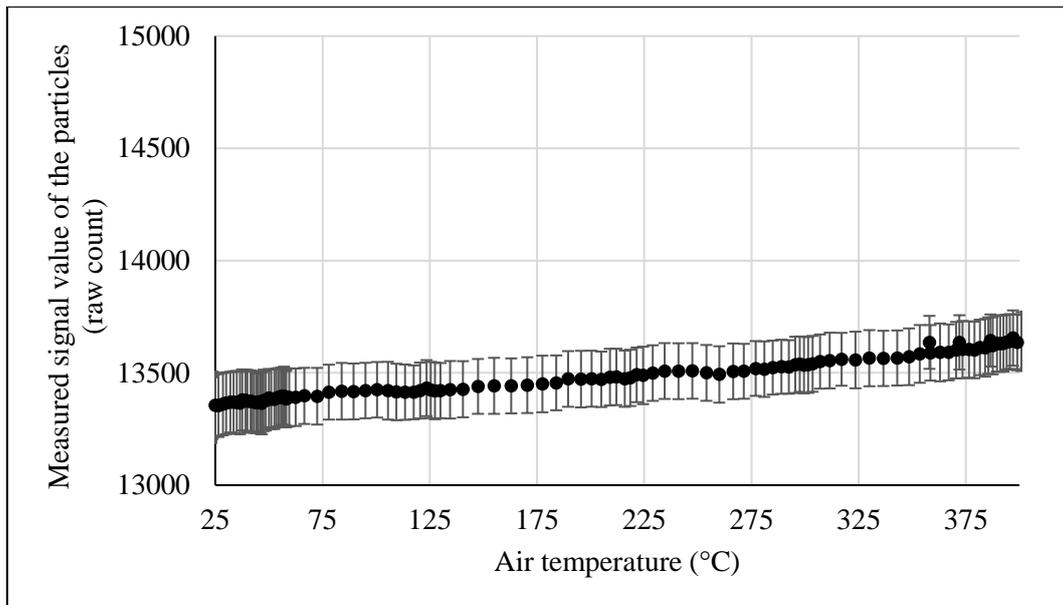
Figure 43. Effect of hot inlet air on the relationship between the signal values corresponding to the identified pixels and the particle temperature (results).

From the results, it can be observed that when the air temperature was increased, the measured signal value of the particles was also increased. This was caused that the thermal radiation emitted from the hot air can also be received by the thermal camera.

It can also be found that when the air temperature was less than $75°C$, the measured signal value of the particles was increased slightly and within the error bar. Therefore, in this thesis, when the inlet air temperature in the fluidized bed was less than $75°C$, the effect of the air temperature on the thermal camera measurement was neglected.

5.2 Calibration Method A (outside, stationary)

The first experiment was designed to correlate the obtained signal value of the particles to the particle temperature when the particles were outside the fluidized bed and placed stationary. The experimental setup was shown in Figure 44. As shown in the figure, particles were placed in a petri dish and heated by a hot plate (STUART US152). The surface temperature of the particles was measured using a K-type thermocouple probe. After the probe was placed, the surface of the particles was flattened. The thermal camera was used to monitor the particles at its minimum focus distance ($250 \, mm$). The frame rate used was $50 \, fps$. A germanium window was placed between the particles and the thermal camera, the same setup as in the fluidized bed experiment (Figure 24).
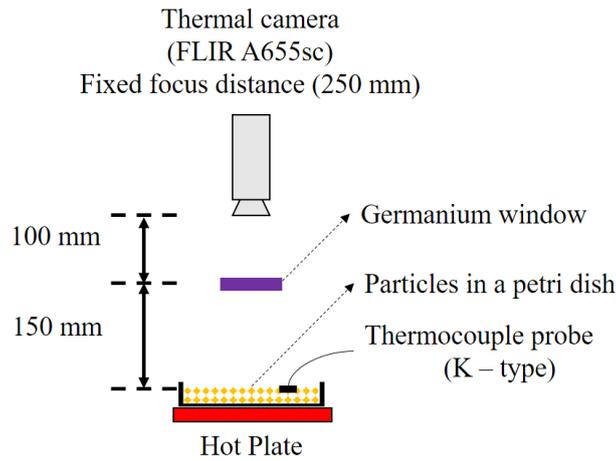
Figure 44. Calibration method A (experimental setup).

In this experiment, temperature of the particle was gradually increased from 25 to 60°C. The measured signal value of the particle was averaged from an area (1.5 × 1.5 mm) representing the particles in the thermal images. Then the measured signal value of the particles was plotted against the particle temperature, as shown in Figure 45.
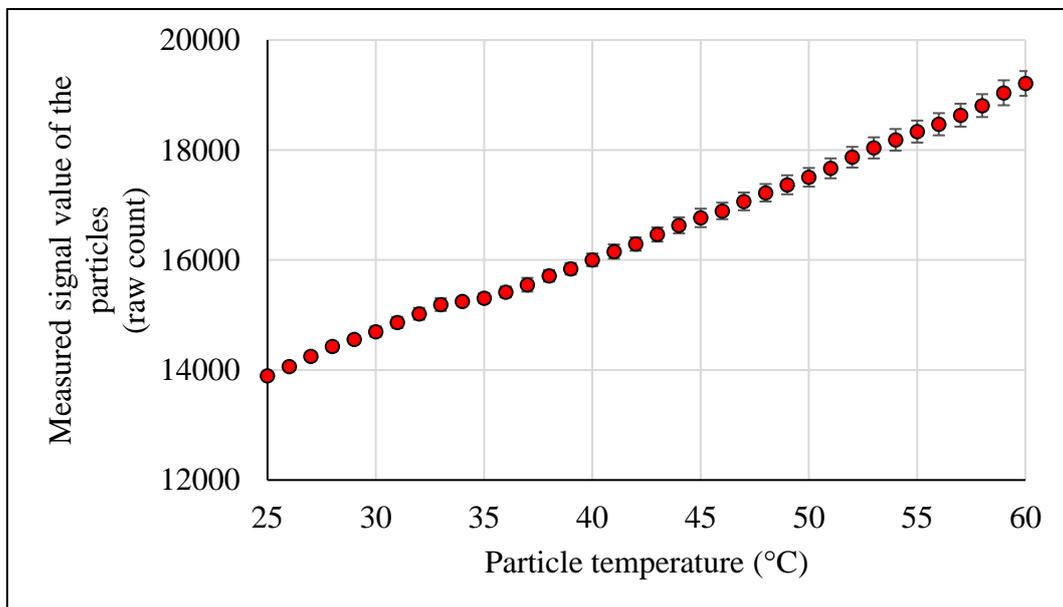
Figure 45. Calibration method A (results).

From the results, it can be found that the obtained signal value of the particles was linearly related to the particle temperature.

In this experiment, since the measurement of the thermocouple probe was affected by room temperature, the measured particle temperature could be slightly lower than the actual particle temperature.

5.3 Calibration Method B (inside, stationary)

The second experiment was designed to correlate the obtained signal value of the particles to the particle temperature when the particles were inside fluidized bed and stationary. The experimental setup was shown in Figure 46. In the fluidized bed, several particles were fixed on the tip of a K-type thermocouple probe, which was located in the centre of the fluidized bed. The thermal camera was used to monitor the particles at its minimum focus distance ($250\ mm$). The frame rate used was $50\ fps$. Height of the thermal camera was $85\ mm$ from the bottom of the fluidized bed.
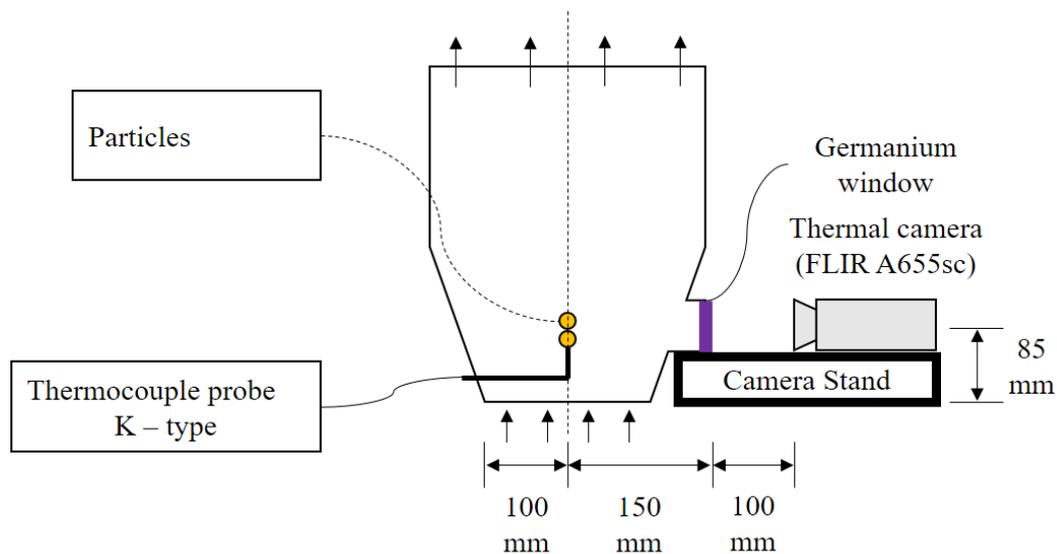
Figure 46. Calibration method B (experimental setup).

In this experiment, temperature of the inlet air was gradually increased from 25 to $70°C$. The measured signal value of the particle was averaged from an area ($1.5 \times 1.5\ mm$)) representing the particles in the thermal images. Then the measured signal value of the particles was plotted against the particle temperature, as shown in Figure 47.
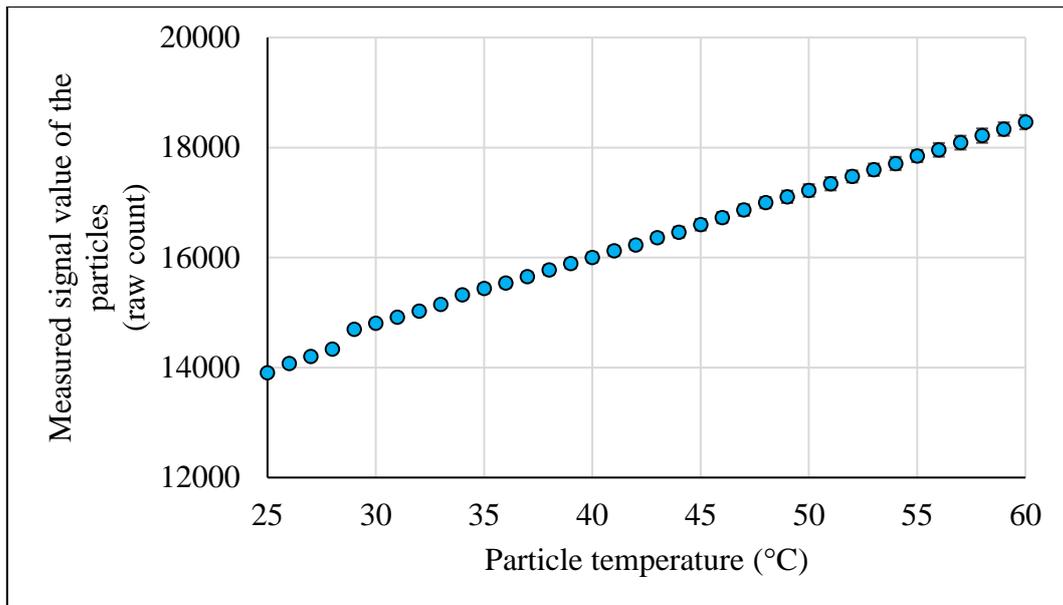
Figure 47. Calibration method B (results).

From the results, it can be found that the obtained signal value of the particles was linearly related to the particle temperature.

In this experiment, since the measurement of the thermocouple probe was affected by inlet air temperature, the measured particle temperature could be slightly higher than the real particle temperature.

Figure 48 compares the results from the offline and online probe methods. It can be found that when the measured signal value of the particles was low, for the same signal value, the measured particle temperature in the two methods was the same. When the measured signal value was high, for the same signal value, the measured particle temperature in the method A was lower. This indicates that the surrounding air of the thermocouple probe can affect the temperature measurement.
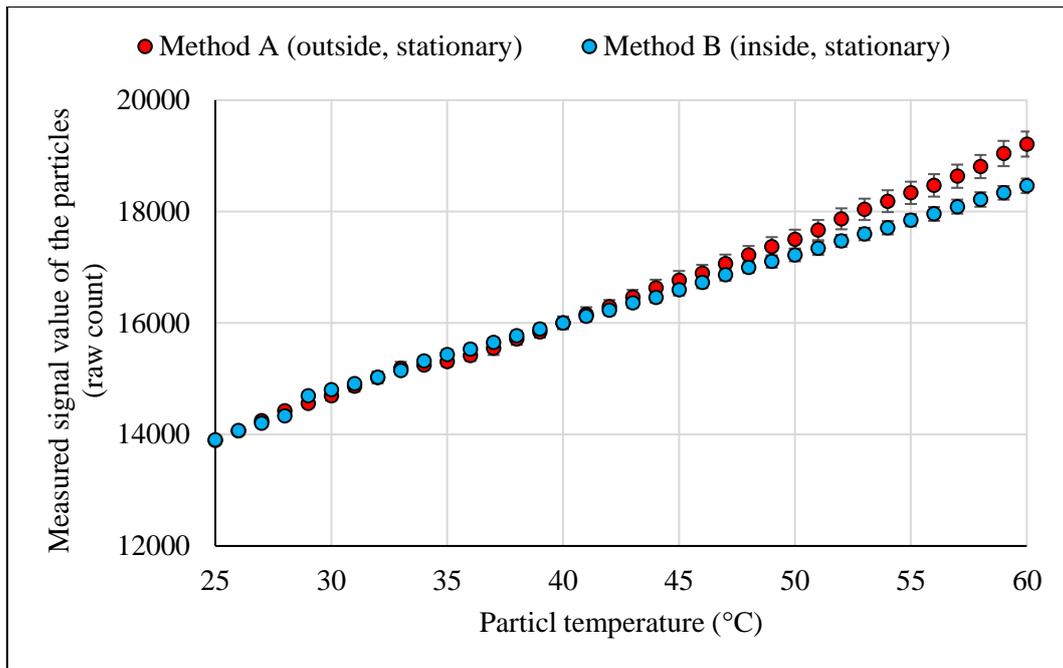
Figure 48. Compare the method A and B.

5.4 Calibration Method C (inside, fluidizing)

Since the particle temperature measured by a thermocouple probe can be affected by the surrounding air of the probe, this experiment was designed. In this experiment, the particles were inside the fluidized bed and fluidizing over time.

As shown in Figure 49, the fluidized bed was thermal insulated. In a thermal insulated fluidized bed, it is assumed that when the temperature steady state is reached, the temperatures of the inlet air, the exit air, the particles and the fluidized bed wall temperature are the same. The loaded particle mass was $1200\ g$. The thermal camera was placed $250\ mm$ from the centre of the fluidized bed to monitor the fluidizing particles using its minimum focus distance. The frame rate used was $50\ fps$. Height of the thermal camera was $85\ mm$ from the bottom of the fluidized bed. Three K-type thermocouple probes were used to measure the temperatures of the inlet air, the ambient, the fluidized bed wall and the exit air. When temperatures of the inlet air, the exit air and the fluidized bed wall did not change over time, the temperature steady state was reached and then the fluidizing particles were monitored using the thermal camera for $2\ min$.
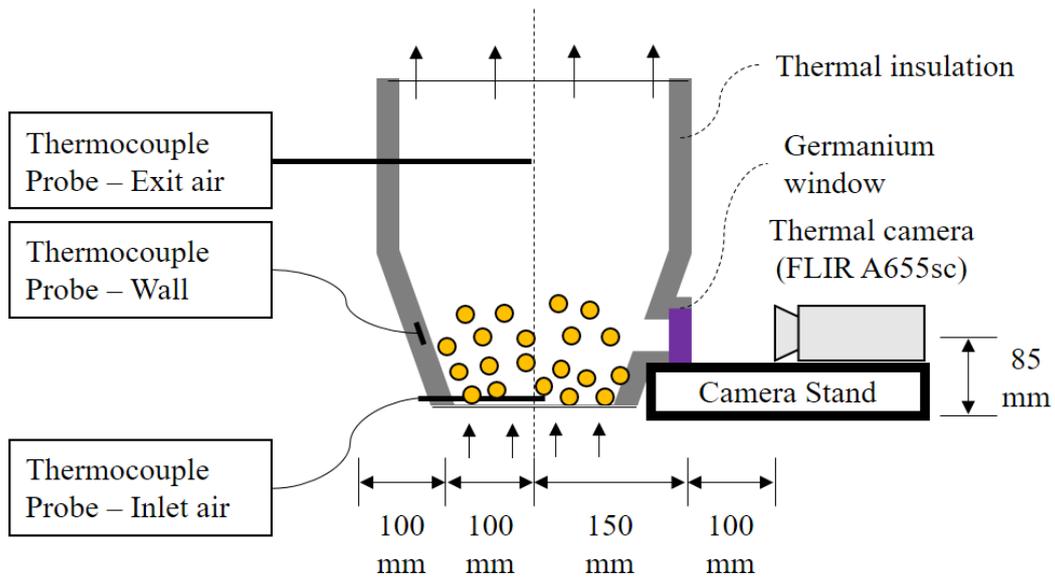
Figure 49. Calibration Method C (experiment).

In this experiment, the inlet air temperature was increased gradually from 25 to $60°C$ and ten temperature steady states were studied. In Figure 50, the number of pixels in the thermal images ($2\ min$) was plotted against their signal values.
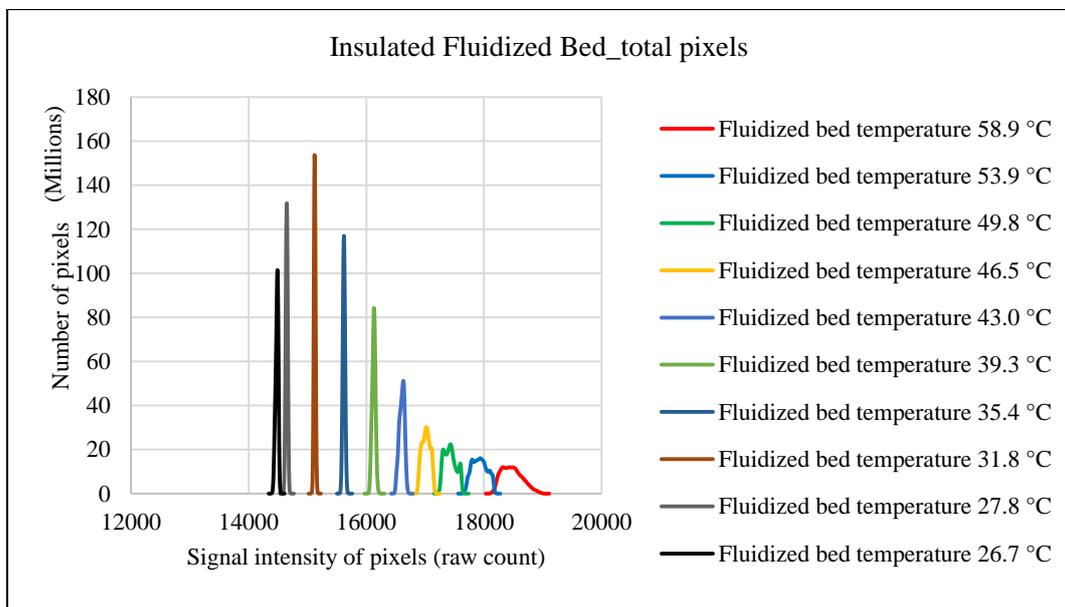
Figure 50. Total pixels in the thermal images (2 min).

In order to correlate the obtained signal value of the pixels to the particle temperature, it is necessary to identify the pixels representing the particles in the thermal images first. However, it is expected that when the thermal radiation emitted from the

fluidized bed wall and the particles was close to each other, the particles in the thermal images were unidentifiable.

In Figure 51, the number of pixels among the identified pixels that represent the particles in the thermal images ($2\ min$) was plotted against their signal values. In the figures, the fluidized bed temperature represents the same temperature of the inlet air, the exit air, the fluidized bed wall and the particles at the temperature steady state.
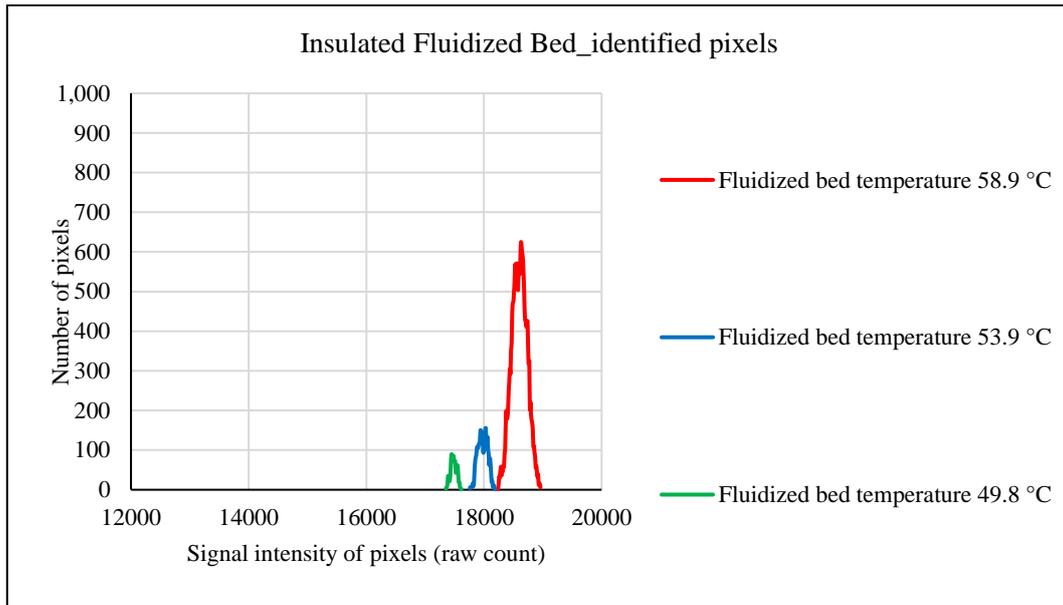
Figure 51. Identified pixels in the thermal images (2 min).

From the above figure, it can be observed that when the fluidized bed temperature was less than $49.8°C$, the particles in the thermal images were unidentifiable. When no pixel was identified in the $2\ min$, the signal values corresponded to the pixels representing the particles and the fluidized bed wall were the same and calculated as the average of all values within the signal matrices obtained in the $2\ min$.

In Figure 52, the results of the method C were plotted and compared with the method A and B.
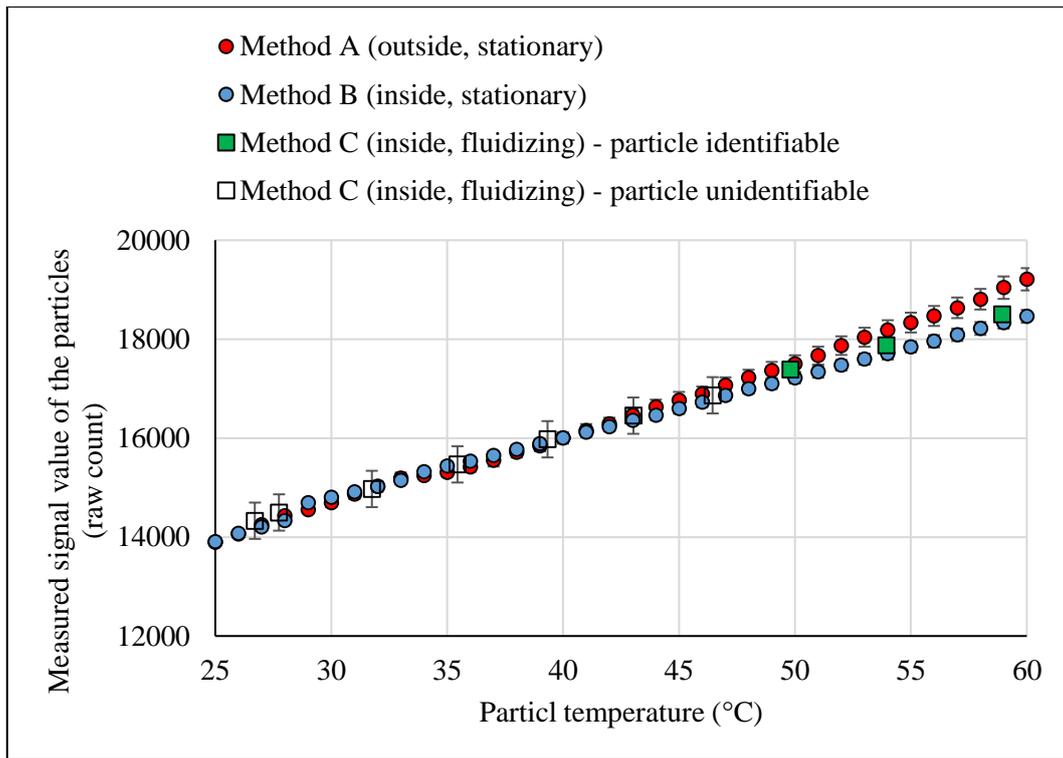
Figure 52. Compare the results from the method A, B, and C.

From the figure, when the measured signal value of the particles was low, for the same signal value, the particle temperature measured in the three methods was similar. When the measured signal value of the particles was high, for the same signal value, the particle temperature measured in the method A was higher than in the method C, and higher than in the method B.

In this thesis, when the measured signal value of the particles was less than $17000\ raw\ count$, it was correlated to the particle temperature averaged from the three methods. When the measured signal value was greater than $17000\ raw\ count$, it was correlated to the particle temperature measured in the method C. The results are shown in Figure 53.
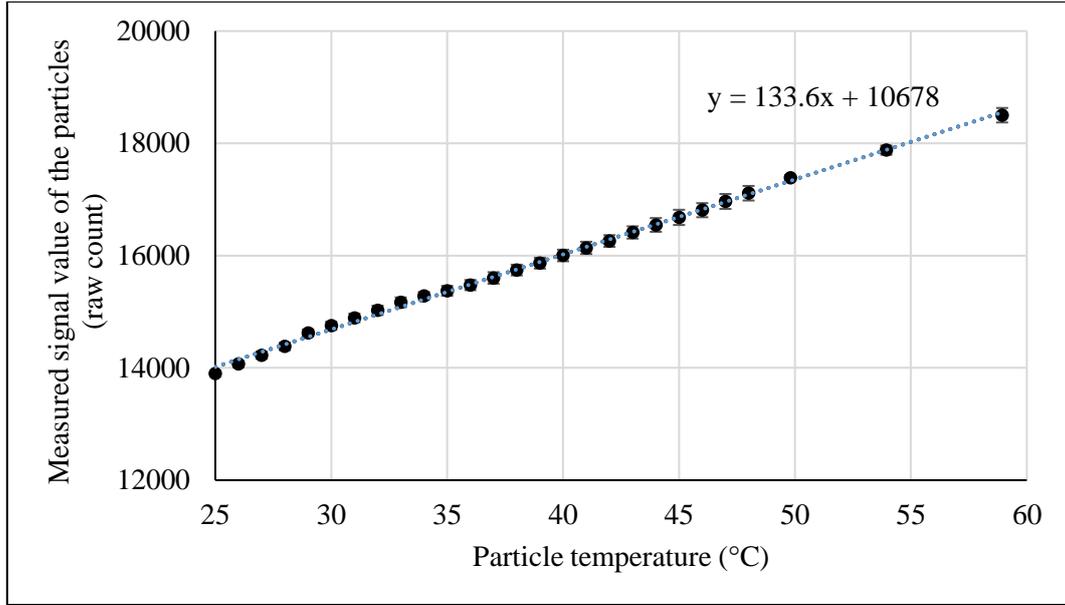
Figure 53. Correlate the measured signal value of the particles to the particle temperature.

From the results, the correlation equation can be fitted as:

$$S_{xy}^* = 133.6 \times T_{xy}^* + 10678 \qquad \text{Eq. (54)}$$

Where S_{xy}^* is an element in the signal matrix $\boldsymbol{S}$ and is corresponded to an identified pixel I_{xy}^* in the thermal image $\boldsymbol{I}$, and T_{xy}^* is the temperature of the particle represented by S_{xy}^* in the signal matrix $\boldsymbol{S}$ and I_{xy}^* in the thermal image correspond to the element S_{xy}^*.

The equation can then be converted to:

$$T_{xy}^* = 0.0075 \times S_{xy}^* - 79.9, \qquad (°C) \qquad \text{Eq. (55)}$$

5.5   Summary

In this chapter, the effect of the flow air on the particle temperature measurement using a thermal camera is examined. It is found that when the air temperature is low, the effect is negligible.

Then three calibration methods were used to correlate the particle temperature with its signal value in the thermal images. In the method A (outside, stationary), the particle was stationary and outside of a fluidized bed. The particle temperature was directly measured by a K-type thermocouple probe. In the method B (inside, stationary), the particle was inside of a fluidized bed and fixed on the tip of a K-type thermocouple

probe. The particle temperature was also directly measured by a K-type thermocouple probe. In the method C (inside, fluidizing), the particles was inside of a thermal insulated fluidized bed and can be fluidized as normal. The particle temperature was deduced from the temperatures of the inlet air, the exit, and the fluidized bed wall at the temperature steady state.

By comparing the results in the three methods, an optimum calibration equation was fitted. This equation will be used in the following chapters to obtain the online particle temperature from the signal matrix output by the thermal camera.

6 Particle heating process

In this chapter, the effect of the inlet air velocity, the inlet air temperature, and the loaded particle mass on the particle temperature was investigated, respectively. The experimental setup used is first introduced in the section 3.4, and repeated here (Figure 54). The fluidized bed was not insulated. Temperatures of the inlet air, the exit air, the fluidized bed wall, and the ambient were online measured by K-type thermocouple probes. Temperature of the particles was online measured by a thermal camera using the previous established method. Since the focus of the thermal camera and the movement of the particles are considered in the particle identification, and the air surrounding the particles is considered in the particle temperature calibration, the particle temperature measured by this method will be more accurate than the results in the literature.
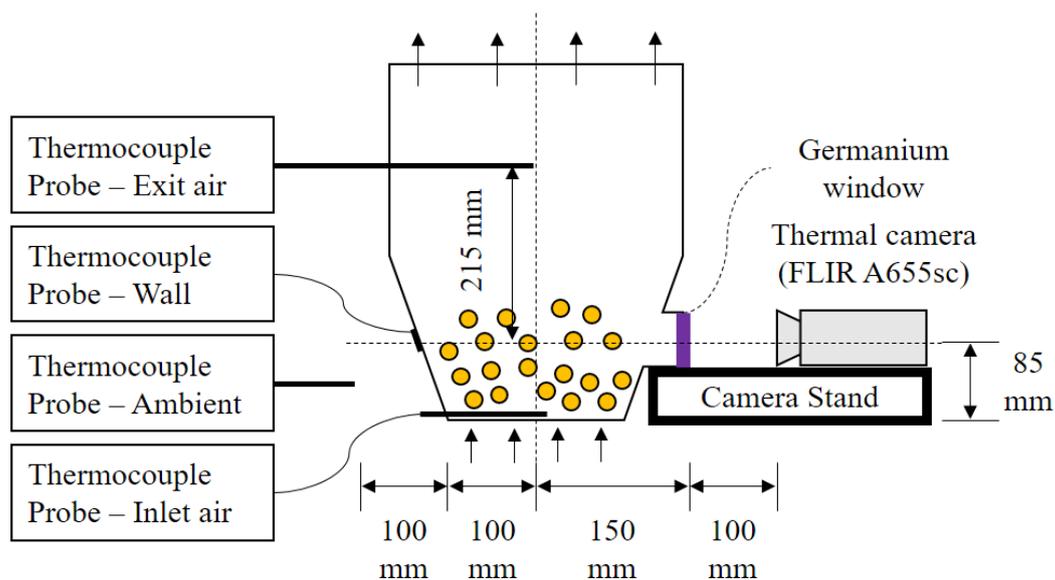
Figure 54. Experimental setup.

At the beginning, the inlet air temperature was $30°C$. When the temperatures of the exit air and the fluidized bed wall did not change over time, the inlet air temperature was started to be increased by the heating system inside the fluidized bed. Then the particle heating process was started. The temperatures of the inlet air, the exit air, the particles, the fluidized bed wall, and the ambient were online measured every second and for 1600 second in total.

The time required by the fluidized bed heating system to heat the inlet air to a desired temperature (53, 57, and 63 °C, respectively) was around $200\ s$. Before $200\ s$, the inlet air temperature was increased rapidly. Followed by the exit air temperature, the particle temperature, and the fluidized bed wall temperature. The particle heating process at this state was mainly determined by the fluidized bed heating system.

In this thesis, the particle heating process was investigated after $200\ s$. In order to compare the heating process of the particles and the fluidized bed wall, a term θ was defined as follow:

$$\theta = \frac{T_p - T_w}{T_a - T_w} \qquad\qquad \text{Eq. (56)}$$

Where T_a is the air temperature (K), T_p is the particle temperature (K), and T_w is the fluidized bed wall temperature (K). From the order of the temperatures, it is known that θ is between 0 (the temperatures of the particles and the fluidized bed wall are same) and 1 (the temperatures of the air and the particles are same).

6.1   Effect of the inlet air velocity

In order to investigate the effect of the inlet air velocity on the particle heating process. The inlet air velocity used was 1.5, 2.0 and 2.5 m/s, respectively. The inlet air temperature used was around $57°C$. The loaded particle mass was $1200\ g$. It should also be noticed that the detector time constant is typical $8\ ms$. The maximum velocity required for the particles to be clear in the thermal image is therefore 0.02 m/s. The online measured temperatures of the inlet air, the exit air, the particles, the fluidized bed wall and the ambient from $200\ s$ to $1600\ s$ are shown in Figure 55, Figure 56, and Figure 57, respectively.
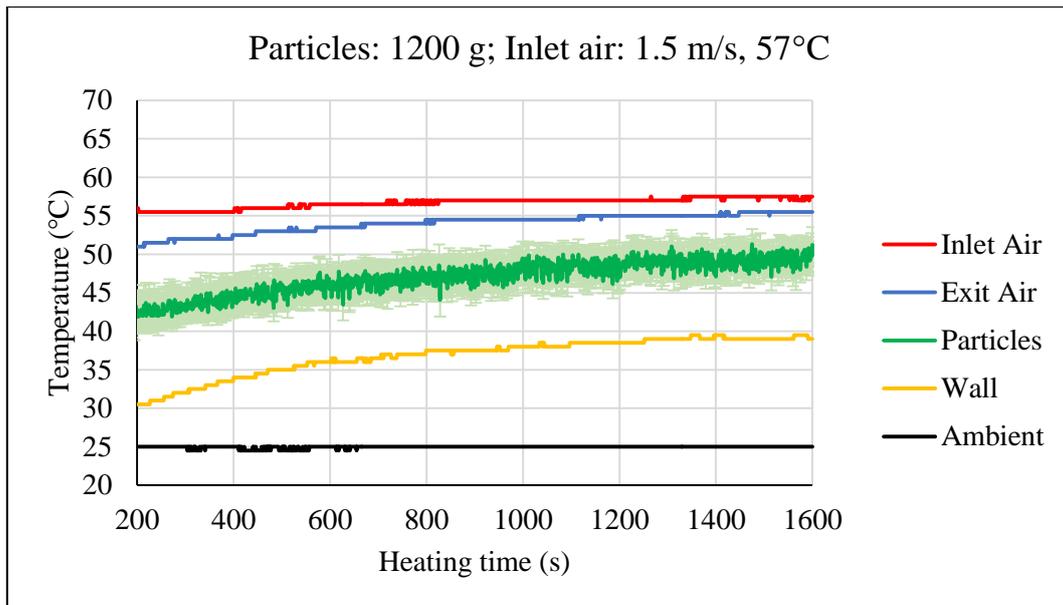
Figure 55. Online monitoring of 1200 g particles heated by 1.5 m/s and 57°C inlet air.

In Figure 55, the inlet air temperature was approximately $57°C$. The exit air temperature was increased from around 51 to $56°C$. The particle temperature was increased from 42 to $49°C$. The fluidized bed wall temperature increased from 31 to $39°C$. The ambient was around $25°C$.
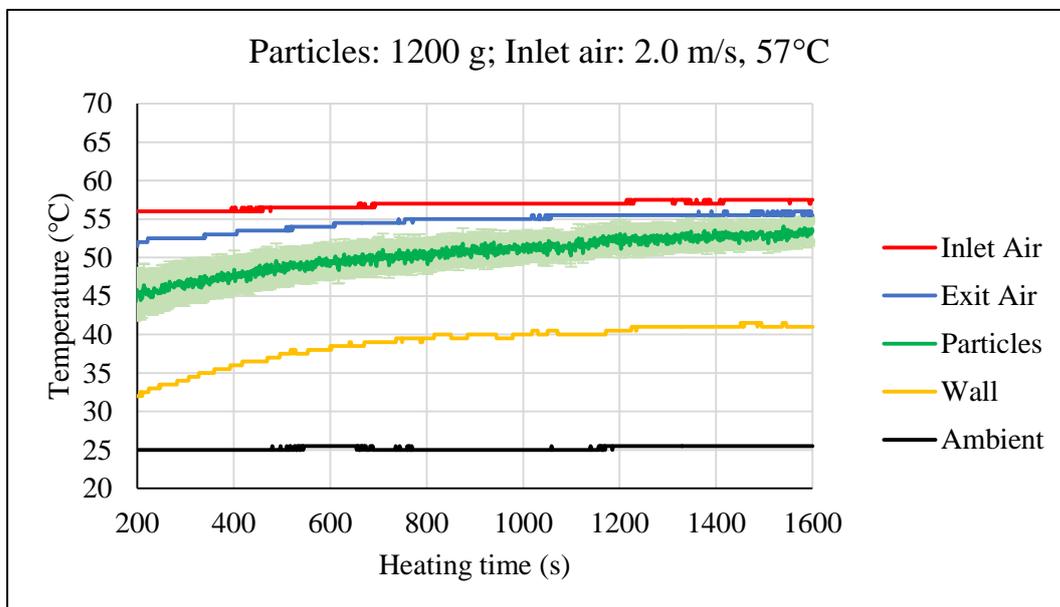
Figure 56. Online monitoring of 1200 g particles heated by 2.0 m/s and 57°C inlet air.

In Figure 56, the inlet air temperature was approximately $57°C$. The exit air temperature was increased from around 52 to $56°C$. The particle temperature was

increased from 45 to 53°C. The fluidized bed wall temperature increased from 32 to 41°C. The ambient was around 25°C.
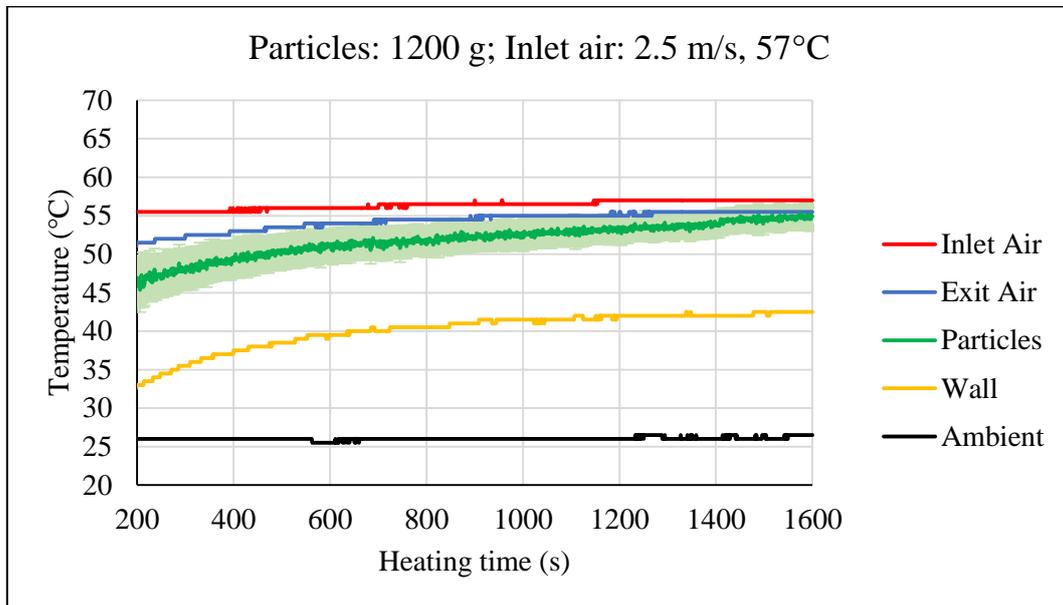
Figure 57. Online monitoring of 1200 g particles heated by 2.5 m/s and 57°C inlet air.

In Figure 57, the inlet air temperature was approximately 57°C. The exit air temperature was increased from around 52 to 55°C. The particle temperature was increased from 46 to 54°C. The fluidized bed wall temperature increased from 33 to 43°C. The ambient was around 26°C.

From the above three figures, it can be found that during the particle heating process, the order of the temperatures from high to low was always the inlet air temperature, the exit air temperature, the particle temperature, the fluidized bed wall temperature and the ambient temperature. This indicates the heat was transferred from the air to both the particles and the fluidized bed wall, from the particles to the fluidized bed wall, and then from the fluidized bed wall to the ambient.

Figure 58 shows the temperature difference between the air (the average of the inlet air and the exit air temperatures) and the particle. From the figure, it can be found that due to the heating process of the particles, the temperature difference was decreased gradually with time. When the inlet air velocity was increased, at the same time, the temperature difference was decreased. This indicates that higher inlet air velocity can accelerate the heating process of the particles.
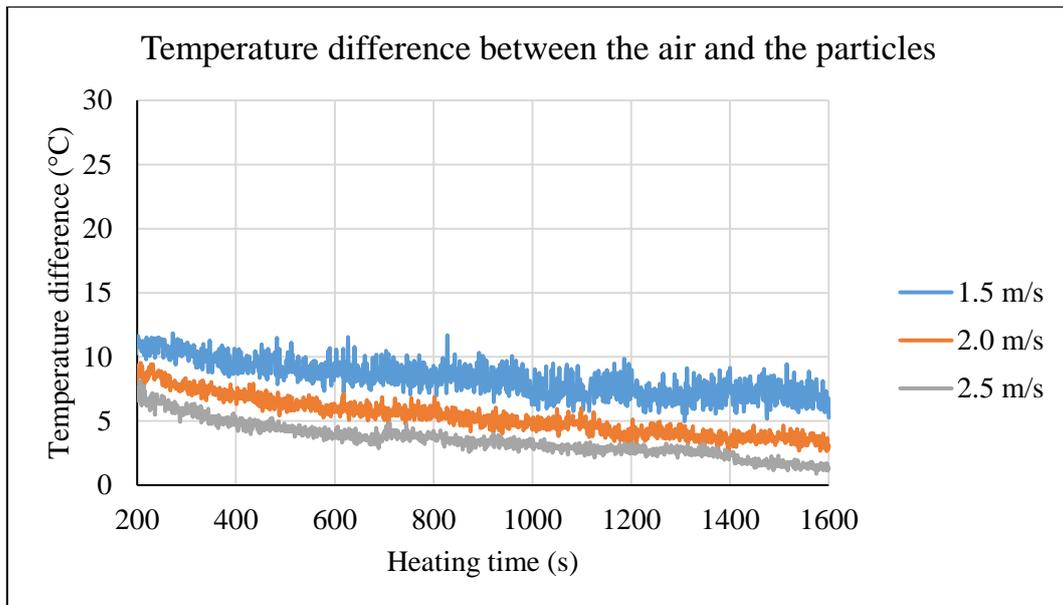
Figure 58. Effect of the inlet air velocity on the temperature difference between the air and the particles.

Figure 59 shows the temperature difference between the air (the average of the inlet air and the exit air temperatures) and the fluidized bed wall. From the figure, it can be found that due to the heating process of the fluidized bed wall, the temperature difference was decreased gradually with time. When the inlet air velocity was increased, at the same time, the temperature difference was decreased. The results indicate that higher inlet air velocity can accelerate the heating process of the fluidized bed wall.
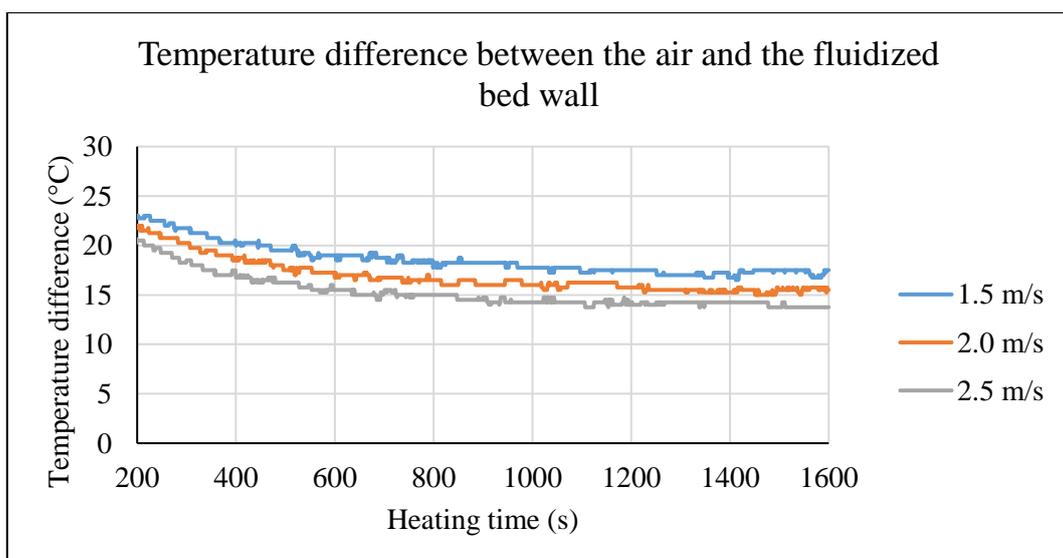
Figure 59. Effect of the inlet air velocity on the temperature difference between the air and the fluidized bed wall.

Figure 60 shows the effect of the inlet air velocity on θ. From the figure, it can be found that θ was increased slowly due to the particle heating process. When the inlet air velocity was increased, θ was increased and the particle temperature was closer to the air temperature. This indicates that the higher inlet air velocity can accelerate the heating process of the particles more than the heating process of the fluidized bed wall.
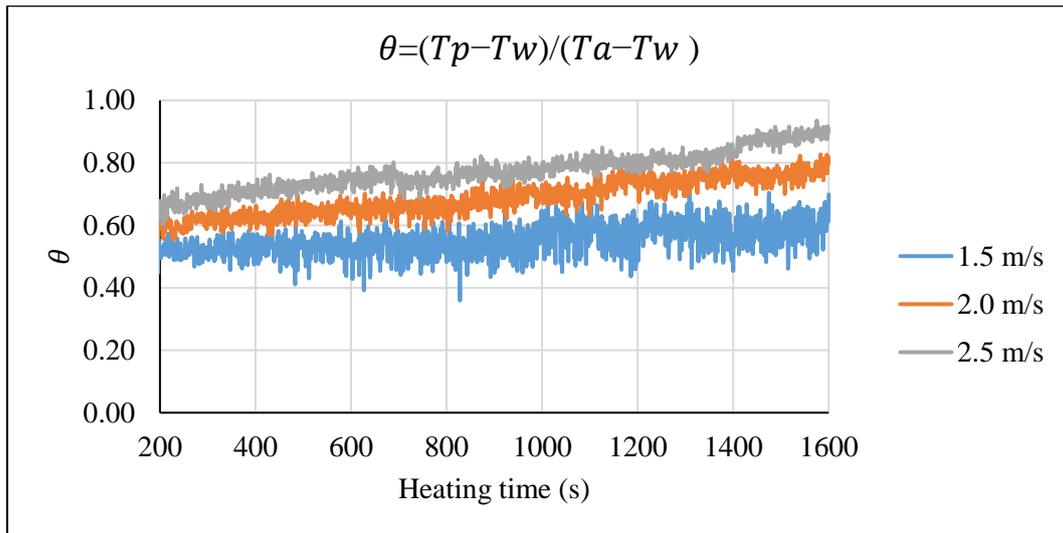
Figure 60. Effect of the inlet air velocity on θ.

6.2 Effect of the inlet air temperature

In order to investigate the effect of the inlet air velocity on the particle heating process. The inlet air velocity used was $2.0\ m/s$. The inlet air temperature used was around 50, 57, and $63°C$, respectively. The loaded particle mass was $1200\ g$. The online measured temperatures of the inlet air, the exit air, the particles, the fluidized bed wall and the ambient from $200\ s$ to $1600\ s$ are shown in Figure 61, Figure 56, and Figure 62, respectively.

In Figure 61, the inlet air temperature was approximately $50°C$. The exit air temperature was increased from around 47 to $50°C$. The particle temperature was increased from 42 to $47°C$. The fluidized bed wall temperature was increased from 32 to $39°C$. The ambient was $27°C$ and did not change over time.
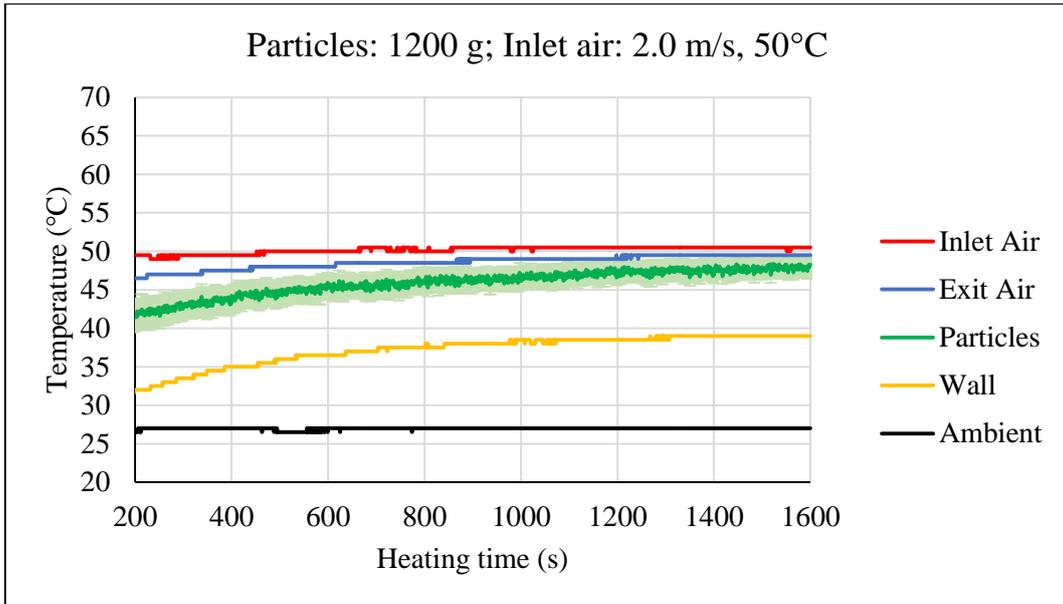
Figure 61. Online monitoring of 1200 g particles heated by 2.0 m/s and 50°C inlet air.

In Figure 62, the inlet air temperature was approximately $63°C$. The exit air temperature was increased from around 57 to $61°C$. The particle temperature was increased from 49 to $61°C$. The fluidized bed wall temperature was increased from 32 to $45°C$. The ambient was $26°C$ and did not change over time.
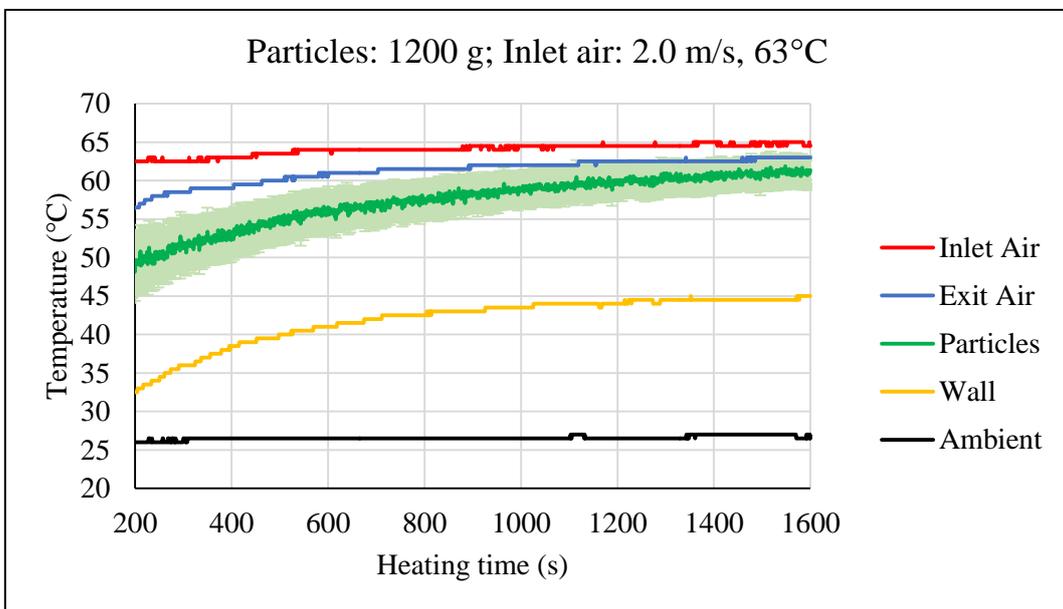
Figure 62. Online monitoring of 1200 g particles heated by 2.0 m/s and 63°C inlet air.

From the above three figures, it is can be found that the order of the temperatures does not affected by the inlet air temperature. The heat transfer from the particles to the fluidized bed wall is higher than that of the hot air to the fluidized bed wall.

Figure 63 shows the temperature difference between the air (the average of the inlet air and the exit air temperatures) and the particle. From the figure, it can be found that due to the heating process of the particles, the temperature differences were decreased gradually with time. At the early state, the temperature difference at the same time was higher when the air temperature (i.e. 50, 57, and $63°C$) was higher.
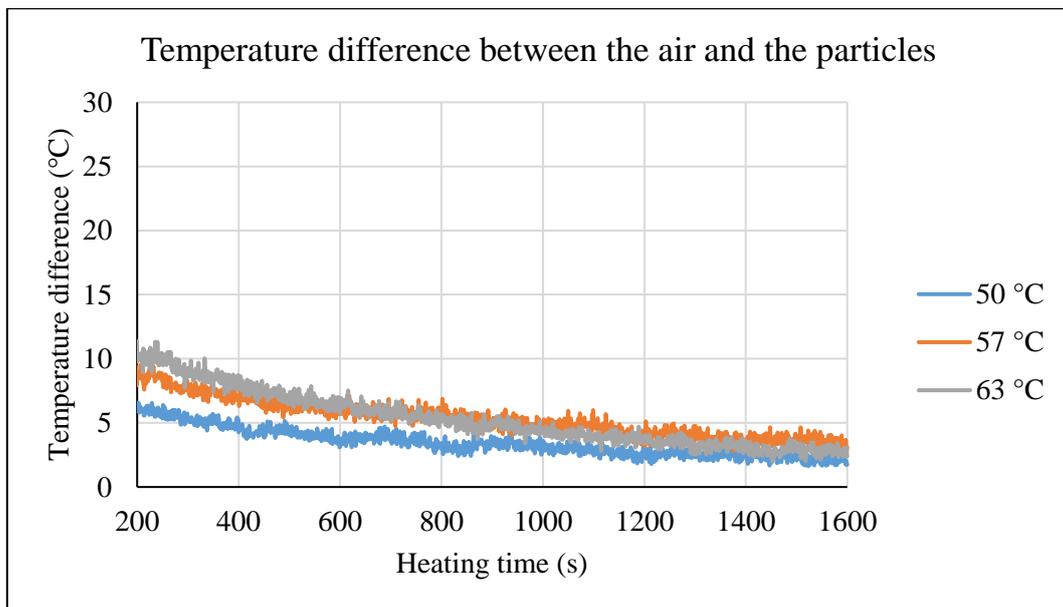
Figure 63. Effect of the inlet air temperature on the temperature difference between the air and the particles.

Figure 64 shows the temperature difference between the air (the average of the inlet air and the exit air temperatures) and the fluidized bed wall. From the figure, it can be found that the temperature difference was decreased gradually with time and the decreasing trend was limited affected by the air temperature. When the air temperature was higher, at the same time, the temperature difference was higher.
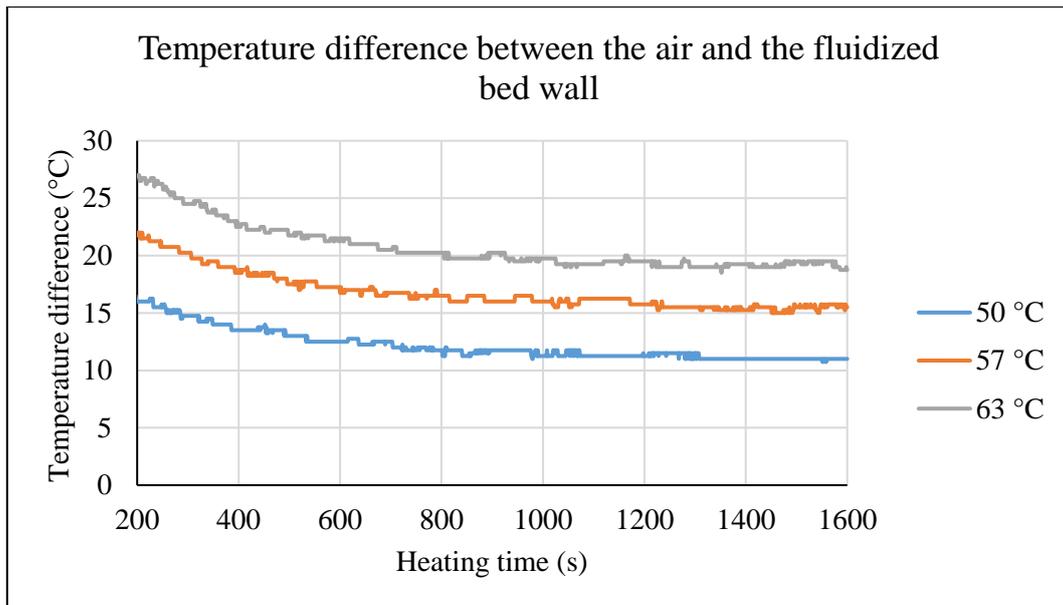
Figure 64. Effect of the inlet air temperature on the temperature difference between the air and the fluidized bed wall.

Figure 65 shows the effect of the inlet air temperature on θ.
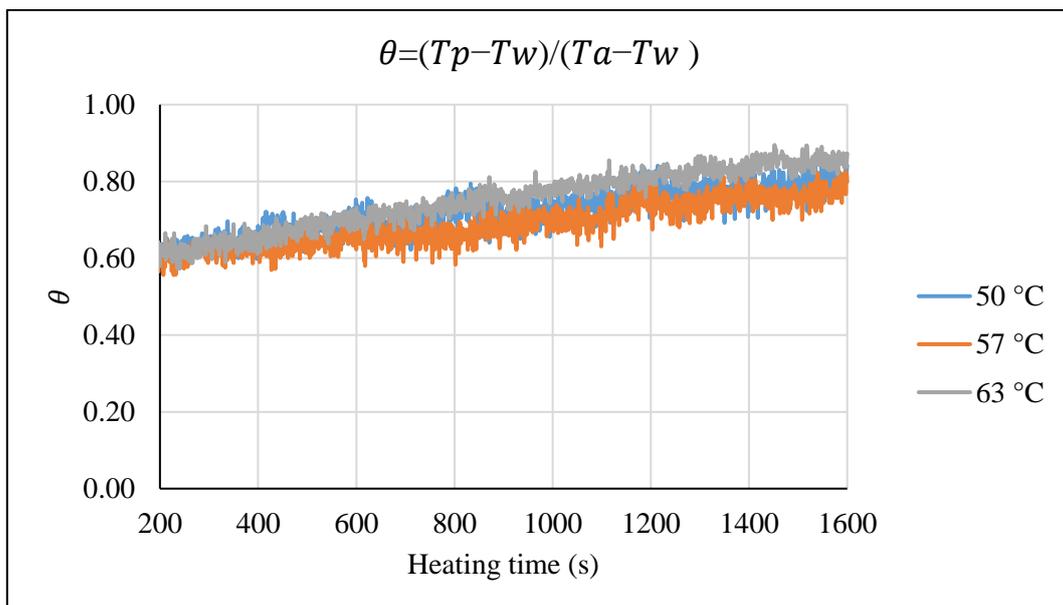
Figure 65. Effect of the inlet air temperature on θ.

From the figure, it can be found that θ was increased slowly due to the particle heating process and the increasing trend was limited affected by the inlet air temperature. This indicates that the when the inlet air temperature was changed, the

relationship between the heating processes of the particles and the heating process of the fluidized bed wall was limited affected.

6.3 Effect of the loaded particle mass

In order to investigate the effect of the inlet air velocity on the particle heating process. The inlet air velocity used was $2.0\ m/s$. The inlet air temperature used was around $57°C$. The loaded particle mass was 1000, 1200, and 1400 g, respectively. The online measured temperatures of the inlet air, the exit air, the particles, the fluidized bed wall and the ambient from $200\ s$ to $1600\ s$ are shown in Figure 66, Figure 56, and Figure 67, respectively.

In Figure 66, the inlet air temperature was approximately $57°C$. The exit air temperature was increased from around 52 to $56°C$. The particle temperature was increased from 42 to $50°C$. The fluidized bed wall temperature was increased from 31 to $41°C$. The ambient was around $24°C$.
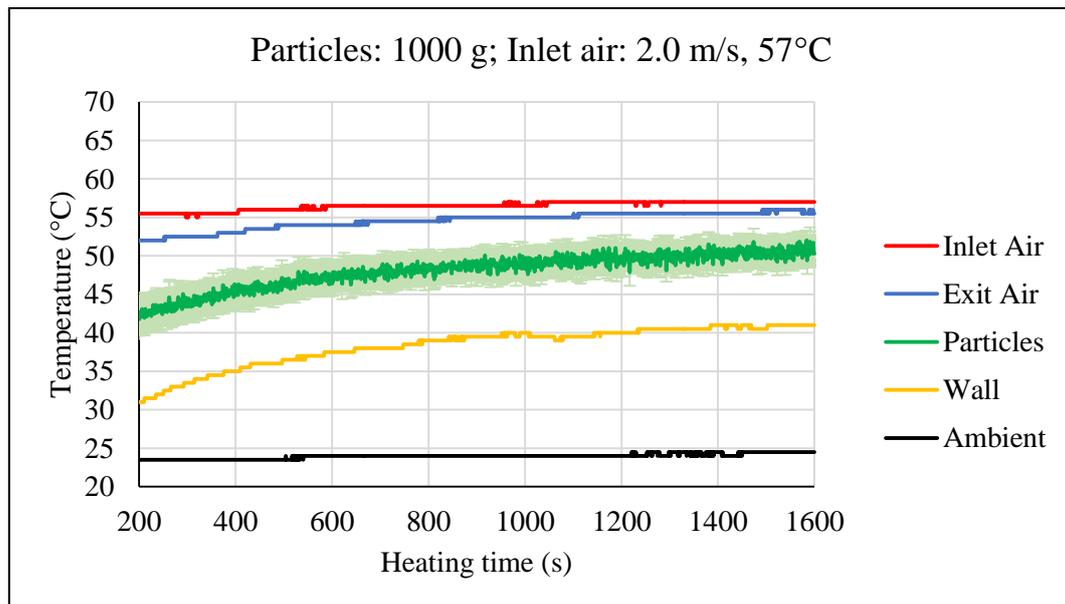
Figure 66. Online monitoring of 1000 g particles heated by 2.0 m/s and 57°C inlet air.

In Figure 67, the inlet air temperature was approximately $57°C$. The exit air temperature was increased from around 52 to $55°C$. The particle temperature was increased from 46 to $54°C$. The fluidized bed wall temperature was increased from 33 to $43°C$. The ambient was around $26°C$.
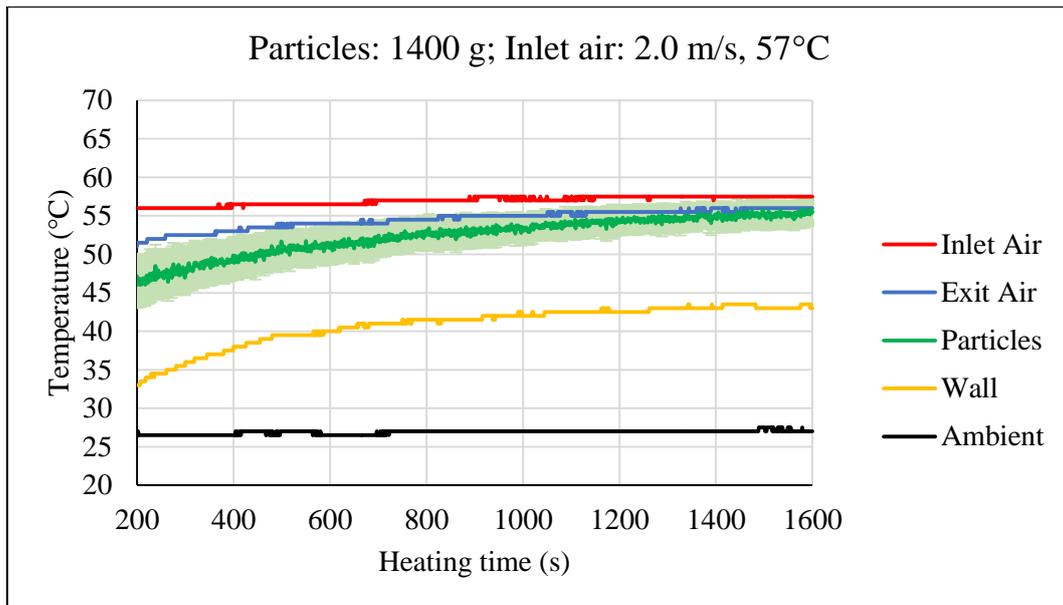
Figure 67. Online monitoring of 1400 g particles heated by 2.0 m/s and 57°C inlet air.

From the Figure 66, Figure 56, and Figure 67, it is can be found that the order of the temperatures does not affected by the loaded particle mass. The heat transfer from the particles to the fluidized bed wall is important.

Figure 68 shows the temperature difference between the air (the average of the inlet air and the exit air temperatures) and the particle. From the figure, it can be found that due to the heating process of the particles, the temperature difference was decreased gradually with time. Generally, it is expected that less loaded particle mass can result in faster particle heating process. However, in this experiment, it can be seen that when the loaded particle mass was less, at the same time, the temperature difference was increased. This indicates that when the mass of the loaded particle is higher (1000g, 1200g, and 1400 g), the heat transfer rate between the air and the particles is higher. This could be caused by the non-uniform temperature distribution in the fluidized bed. When there are more particles, the fluidization of the particles becomes worse and most of the particles are likely to stay close to the bottom of the fluidized bed.
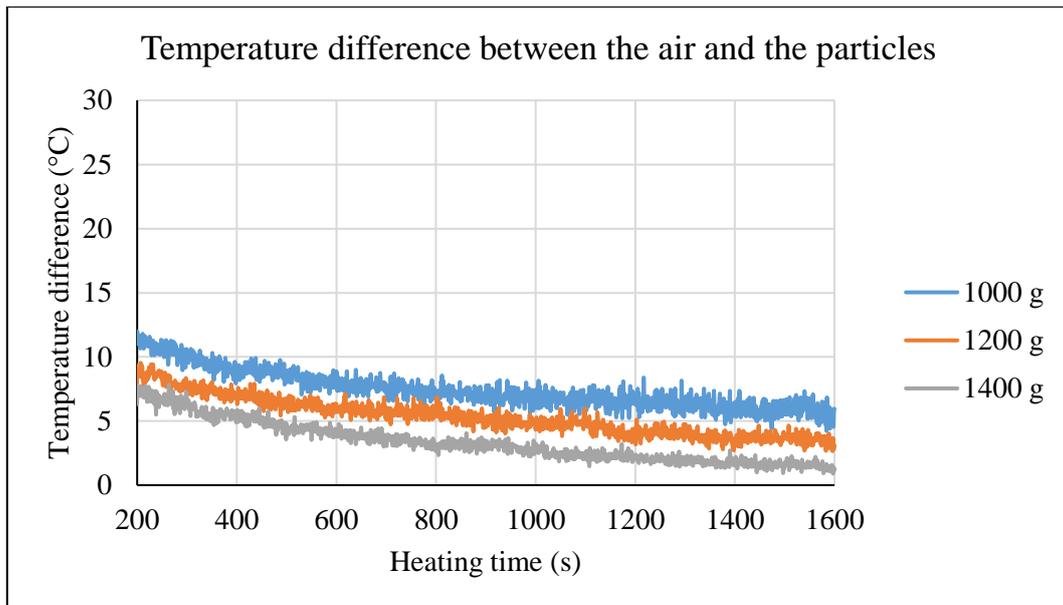
Figure 68. Effect of the loaded particle mass on the temperature difference between the air and the particles.

Figure 69 shows the temperature difference between the air (the average of the inlet air and the exit air temperatures) and the fluidized bed wall.
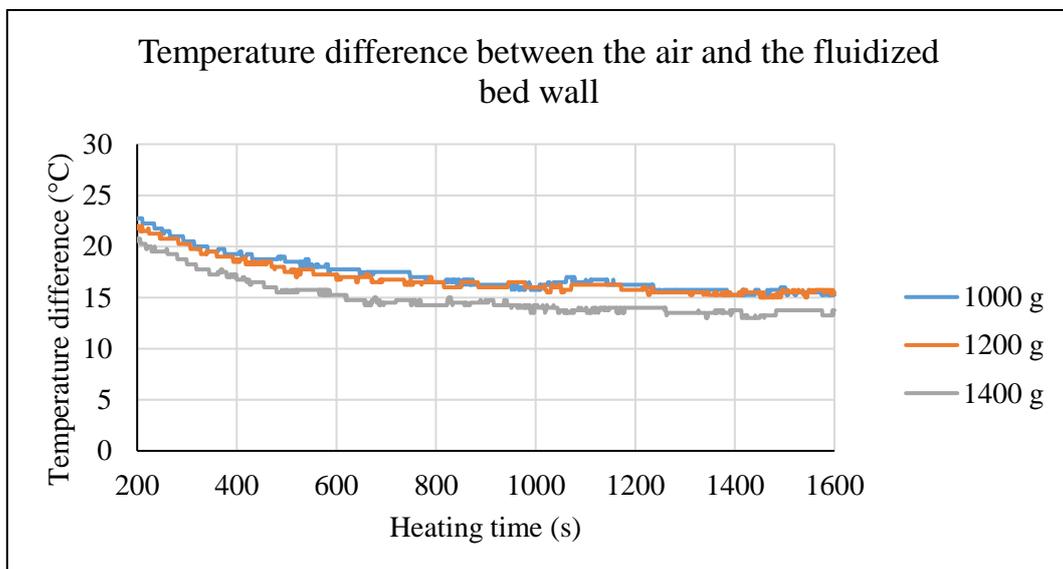
Figure 69. Effect of the loaded particle mass on the temperature difference between the air and the fluidized bed wall.

From the figure, it can be found that the temperature difference was decreased gradually with time. When the loaded particle mass was increased, at the same time, the temperature difference for the 1000 g loaded particle mass was slightly higher than the temperature difference for the 1200 g loaded particle mass, significantly

higher than the temperature difference for the 1400 g loaded particle mass. This indicates that higher loaded particle mass can accelerate the heating process of the fluidized bed wall.

Figure 70 shows the effect of the inlet air temperature on θ. From the figure, it can be found that θ was increased slowly due to the particle heating process. When the loaded particle mass was increased, θ was increased and the particle temperature was closer to the air temperature. This indicates that the higher loaded particle mass can accelerate the heating process of the particles more than the heating process of the fluidized bed wall.
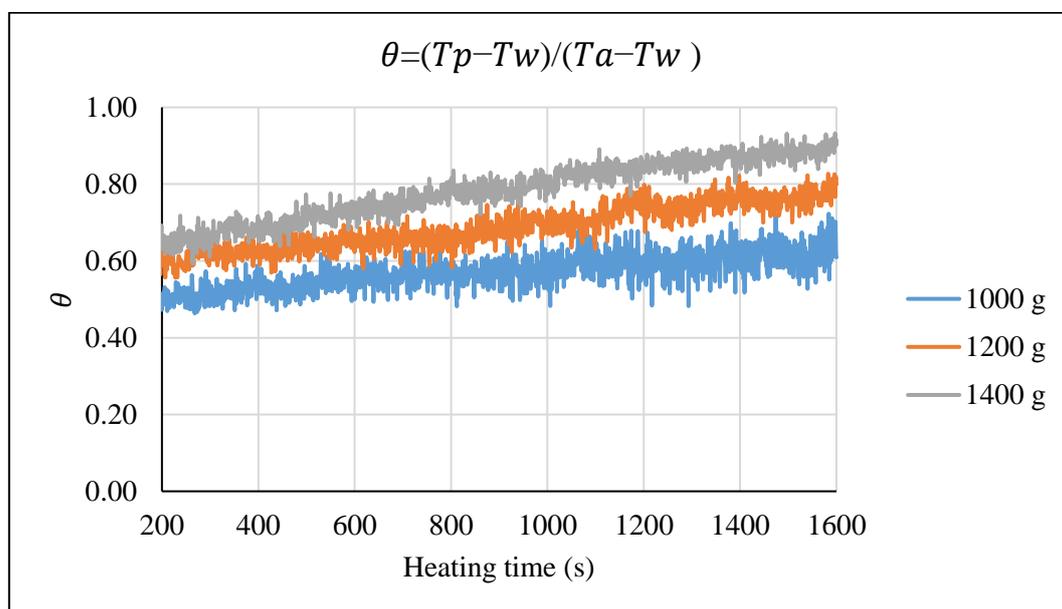
Figure 70. Effect of the loaded particle mass on θ.

6.4 Validation

Since the experiments were operated in the similar ambient environment, the heat transfer coefficient between the fluidized bed wall and the ambient should be a constant. Therefore, it can be used to validate the experimental results.

In order to estimate the heat transfer coefficient between the fluidized bed and the ambient, the energy balance was used:

$$E_{input} = E_p + E_w + E_{lost} \qquad \text{Eq. (57)}$$

Where E_{input} is the total energy input from the air to particles and the fluidized bed wall (J), E_p is the energy that increases the particle temperature (J), E_w is the energy that increases the fluidized bed wall temperature (J), and E_{lost} is the energy lost (J).

The overall energy balance from heating time 200 s to 1600 s was:

$$E_{input} = \int_{200}^{1600} \rho_a U_{in} A_{in} C_{p,a} [T_{in}(t) - T_{ex}(t)] dt \qquad \text{Eq. (58)}$$

$$E_p = m_p C_{p,p} [T_p(1600) - T_p(200)] \qquad \text{Eq. (59)}$$

$$E_w = m_w C_{p,w} [T_w(1600) - T_w(200)] \qquad \text{Eq. (60)}$$

$$E_{lost} = \int_{200}^{1600} h_{lost} A_{lost} [T_w(t) - T_{amb.}(t)] dt \qquad \text{Eq. (61)}$$

Where ρ_a is the density of the air (kg/m^3), U_{in} is the inlet air velocity (m/s), A_{in} is the cross-sectional area of fluidized bed air distributor (m^2), $C_{p,a}$ is the specific heat capacity of air $(J/kg \cdot K)$, t is the heating time (s), $T_{in}(t)$ is the inlet air temperature at the heating time t (K), $T_{ex}(t)$ is the exit air temperature at the heating time t (K), m_p is the loaded particle mass (kg), $C_{p,p}$ is the specific heat capacity of the particles $(J/kg \cdot K)$, $T_p(1600)$ is the particle temperature at the heating time 1600 s, $T_p(200)$ is the particle temperature at the heating time 200 s, m_w is the mass of fluidized bed wall (kg), $C_{p,w}$ is the specific heat capacity of the fluidized bed wall $(J/kg \cdot K)$, $T_w(1600)$ is the fluidized bed wall temperature at the heating time 1600 s, $T_w(200)$ is the fluidized bed wall temperature at the heating time 200 s, h_{lost} is the heat transfer coefficient between the fluidized bed wall and the ambient air $(W/m^2 \cdot K)$, A_{lost} is outside surface area of the fluidized bed wall (m^2), $T_w(t)$ is the fluidized bed wall temperature at the heating time t (K), $T_{amb.}(t)$ is the ambient temperature at the heating time t (K).

Then the h_{lost} was calculated to be $154 \pm 8\%$ $(W/m^2 \cdot K)$, which is approximately a constant. Therefore, it is validated that the experimental results are reliable.

6.5 Summary

In this chapter, during the particle heating process, the online temperature of the particles were measured by a thermal camera and the online temperatures of the inlet

air, the exit air, the fluidized bed wall and the fluidized bed ambient were measured by thermocouple probes.

By introducing $\theta = \frac{T_p - T_w}{T_a - T_w}$, the temperatures of the air (average of the inlet air and the exit air), the particles, and the fluidized bed wall can be compared. From the results, it was found that higher inlet air velocity can accelerate the heating process of the particles more than the heating process of the fluidized bed wall. Changing inlet air temperature did not change the relationship between the heating processes of the particles and the heating process of the fluidized bed wall significantly. It is found that higher loaded particle mass (1000 g, 1200 g, and 1400 g) can result in faster particle heating process. The reason may be that when there are more particles, the fluidization of the particles becomes worse and the particles are more likely to stay near the bottom of the fluidized bed.By assuming the heat transfer coefficient between the fluidized bed wall and the ambient was a constant, the measured temperatures were validated.

7 Heat transfer mechanism

7.1 Temperature steady state

7.1.1 Temperatures

In this chapter, $1000\ g$, $1200\ g$ and $1400\ g$ particles were loaded in the fluidized bed, respectively. The introduced inlet air velocity was 1.5, 2.0 and $2.5\ m/s$, respectively. At the beginning, temperature of the inlet air was $30°C$. When the temperatures of the exit air and the fluidized bed wall did not change over time, the inlet air temperature was increased to 50, 57 and $63°C$, respectively. The experimental parameters were illustrated in Figure 71.
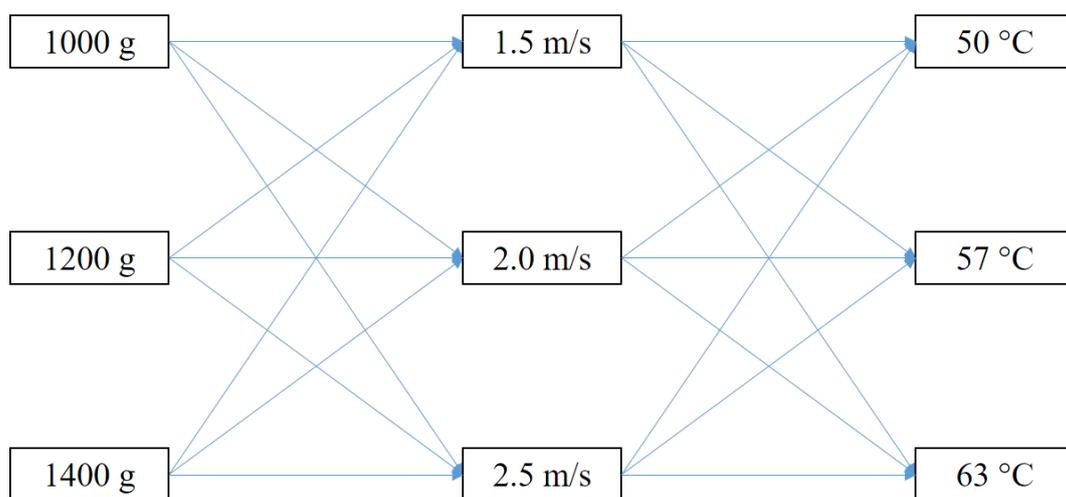
Figure 71. Parameters of the extended experiments.

When the online temperatures of the inlet air, the exit air, the particles, the fluidized bed wall, and the ambient were not changing significantly for $100\ s$, a temperature steady state was considered to be achieved.

The temperatures measured within the $100\ s$ were averaged, respectively. The results are shown in Table 1. Inlet air temperature in the parameter column is the set temperature on the control panel of the fluidized bed. The temperatures of inlet air, exit air, wall, and ambient were measured by thermocouple probes. The temperature of particle was measured by the thermal camera.

Table 1. Temperatures of the inlet air, the exit air, the particles, the fluidized bed wall, and the ambient at steady state.

Parameters			Inlet air	Exit air	Particle	Wall	Ambient
Loaded particle mass (g)	Inlet air velocity (m/s)	Inlet air temperature (°C)	(°C)				
1000	1.5	50	49.5	48.1	34.9	43.6	23.0
1000	2.0	50	50.0	49.0	37.2	45.0	24.5
1000	2.5	50	49.9	49.0	38.4	47.5	25.4
1000	1.5	57	56.5	55.0	37.9	47.4	22.5
1000	2.0	57	57.0	55.7	40.9	50.5	24.4
1000	2.5	57	56.5	55.0	41.4	52.9	25.0
1000	1.5	63	64.7	62.3	41.1	56.1	25.6
1000	2.0	63	64.8	63.2	44.5	59.3	26.5
1000	2.5	63	64.0	62.5	45.2	61.2	27.0
1200	1.5	50	50.1	48.5	36.4	43.4	26.0
1200	2.0	50	50.5	49.5	39.0	47.7	27.0
1200	2.5	50	50.4	49.5	39.5	49.2	27.0
1200	1.5	57	57.4	55.4	39.1	49.3	25.0
1200	2.0	57	57.5	55.7	41.1	52.9	25.5
1200	2.5	57	57.0	55.5	42.3	54.6	26.2
1200	1.5	63	64.6	62.4	41.1	55.9	25.5
1200	2.0	63	64.7	62.8	44.6	60.9	26.9
1200	2.5	63	64.0	62.0	45.6	61.4	26.5
1400	1.5	50	50.0	48.5	36.3	44.2	24.5
1400	2.0	50	50.2	49.0	38.5	47.9	26.1
1400	2.5	50	50.1	49.0	39.8	49.0	27.0
1400	1.5	57	57.2	55.0	39.6	50.0	25.6
1400	2.0	57	57.5	55.9	43.2	55.1	27.1
1400	2.5	57	57.3	55.6	43.9	56.0	27.8
1400	1.5	63	65.1	62.2	43.3	56.6	27.1
1400	2.0	63	64.9	62.5	46.3	60.7	27.5
1400	2.5	63	64.5	62.5	46.7	61.8	28.0

7.1.2 Bed height

From the thermal images, the average distance between the identified particles and the bottom of the thermal image can be obtained in the unit of pixels (Figure 72).
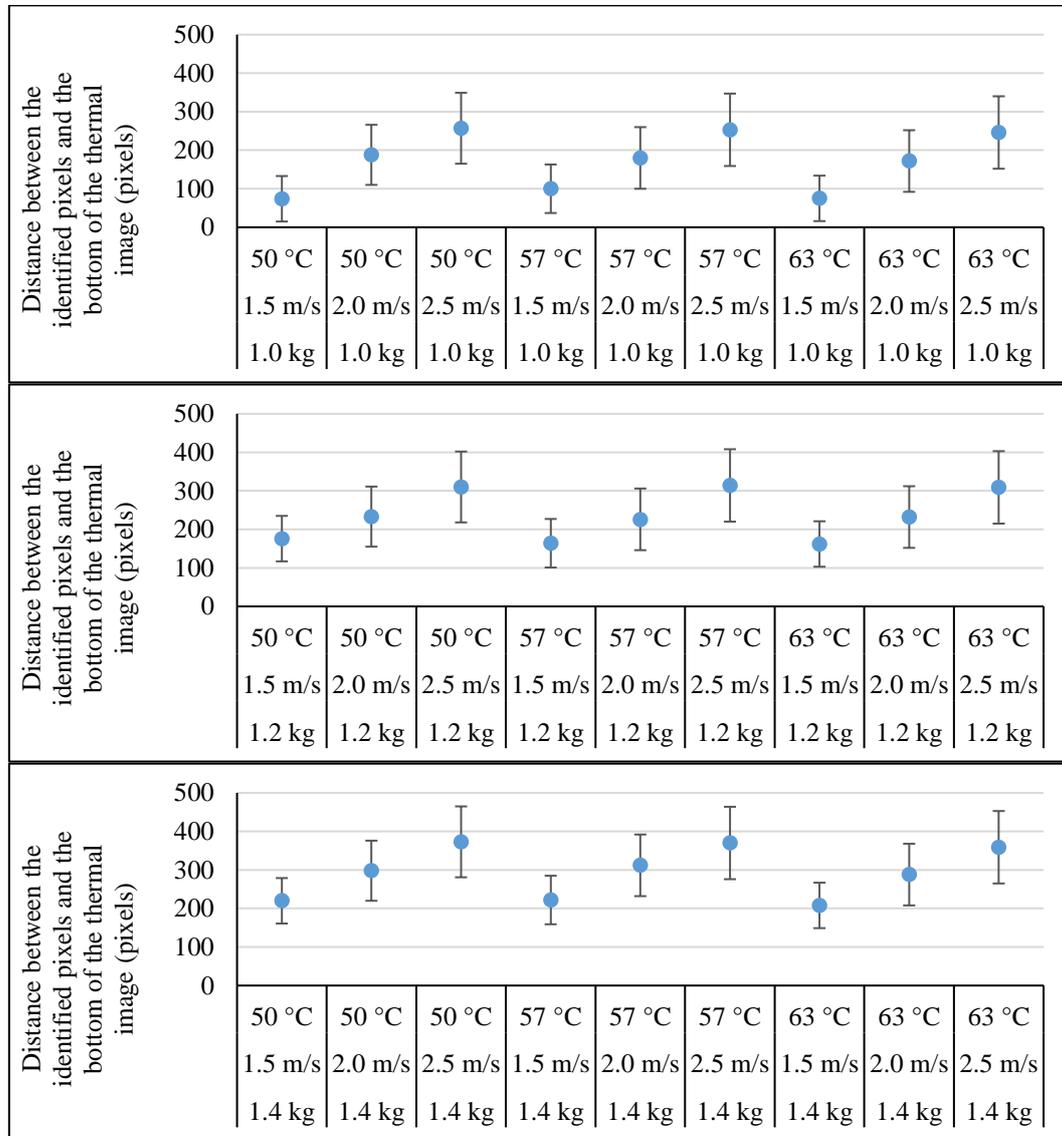
Figure 72. Distance between the identified particles and the bottom of the thermal image (pixels).

Since the pixel size (l_{pixel}) was $0.15\ mm = 0.15 \times 10^{-3}\ m$, the distance between the bottom of the thermal image and the bottom of the fluidized bed ($H_{image-distributor}$) was $37 \times 10^{-3}\ m$. The unit of the distance between the identified particles and the thermal image bottom can be converted from pixels to meter (Figure 73).
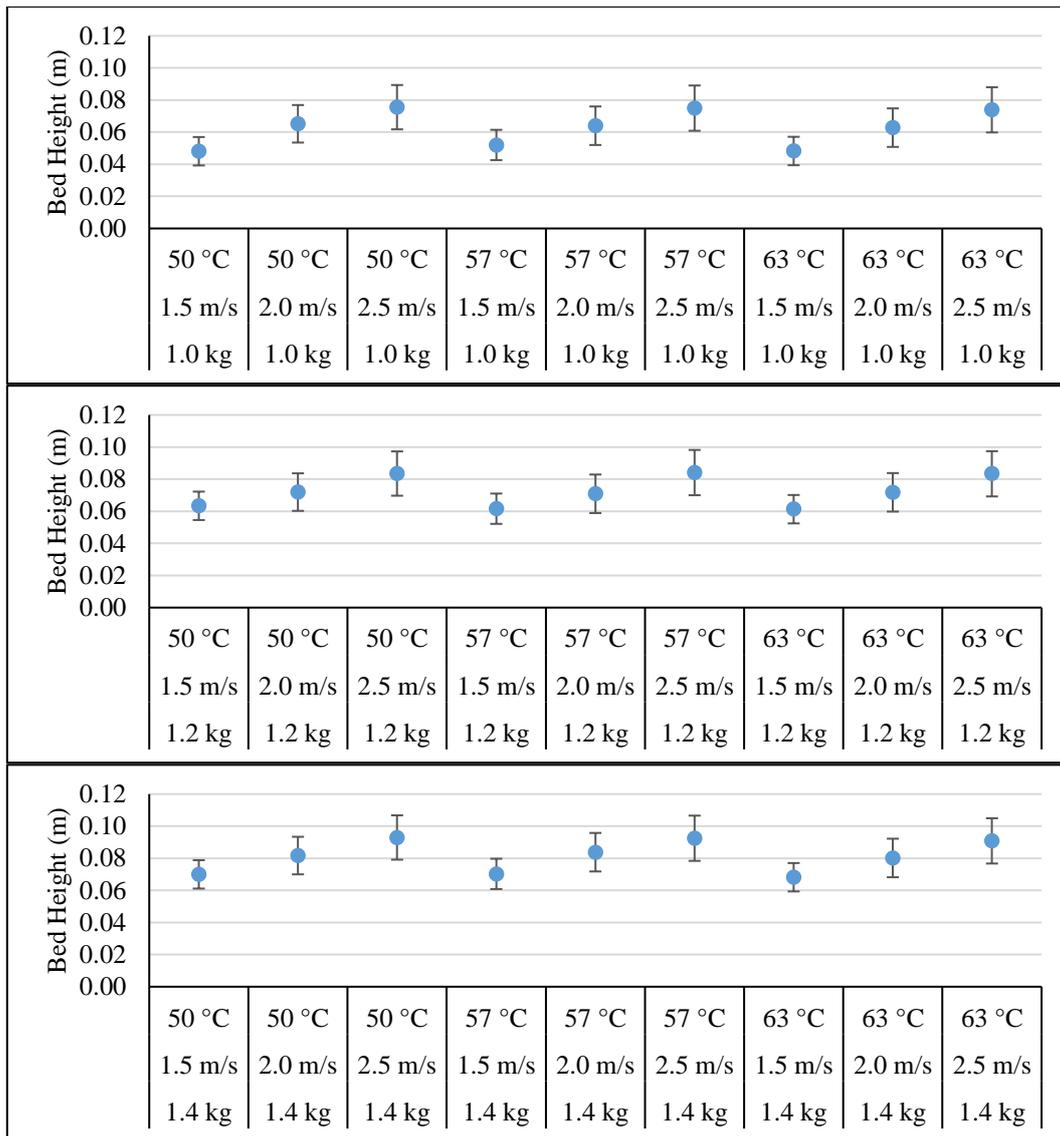
Figure 73. Bed height (mm).

From the results, it can be observed that when the inlet air velocity or the loaded particle mass was increased, the bed height was increased, while the effect of the inlet air temperature on the bed height was negligible.

In this thesis, when the inlet air velocity is increased, the average height of the identified particles in the thermal images is increased as well.

7.1.3 Wall area and void fraction of the fluidized bed

The fluidized bed wall area is the area of the particles in contact with the fluidized bed wall. The void fraction of the fluidized bed is the ratio of the air volume in the particle bed and the total volume of the particle bed.

In order to calculate them from the bed height, following geometric model was used (Figure 74). It is assumed that the particles were uniformly distributed between the bottom of the fluidized bed and the height of the identified particles.
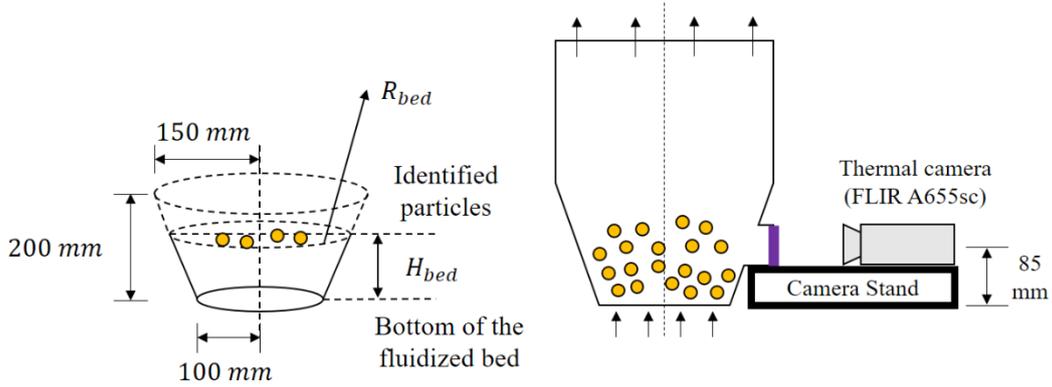
Figure 74. Geometric model.

As shown in the figure, the fluidization area of the particles is a frustrated cone (top radius is $150\ mm$, bottom radius is $100\ mm$, and height is $200\ mm$). When H_{bed} is the average height of the identified particles (m), it can be calculated that:

$$R_{bed} = 0.1 + \frac{H_{bed}}{4} \qquad \text{Eq. (62)}$$

The contact area between the particles and the Fluidized bed wall can be calculated as:

$$A_{bed} = \varepsilon \pi R_{bed} \left(R_{bed} + \sqrt{(0.4 + H_{bed})^2 + R_{bed}^2} \right) - 0.19 \qquad \text{Eq. (63)}$$

The total volume of the particle bed can be calculated as:

$$V_{bed} = \pi R_{bed}^2 \frac{0.4 + H_{bed}}{3} - 0.0042 \qquad \text{Eq. (64)}$$

Figure 75 shows the calculated fluidized bed wall area and Figure 76 shows the calculated total volume of the particle bed.

Since the particle density was $2600 \ kg/m^3$, the volume of the particles can be calculated as:

$$V_{particles} = \frac{m_{particles}}{2600 \ kg/m^3}$$

Eq. (65)

Where $m_{particles}$ is the loaded particle mass (kg).

Then the void fraction of the particle bed can be calculated using:

$$\varepsilon = 1 - \frac{V_{particles}}{V_{bed}}$$

Eq. (66)

The calculated void fractions are shown in Figure 77.

From the results, it can be found that when the inlet air velocity was increased, the void fraction was increased. When the loaded particles mass was increased, the effect of the inlet air velocity on the void fraction was less significant.
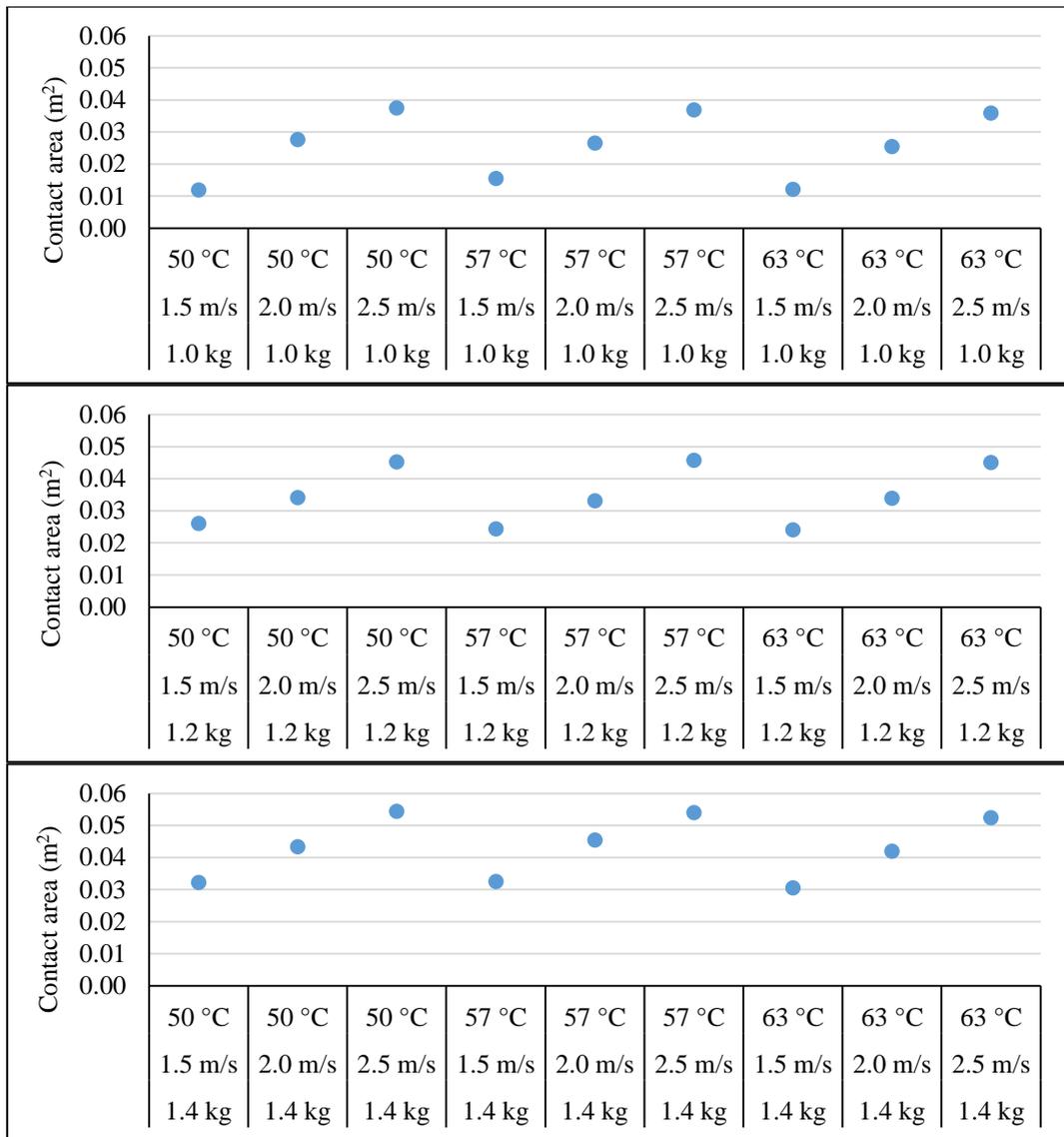
Figure 75. Contact area between the particles and the Fluidized bed wall (m^2).
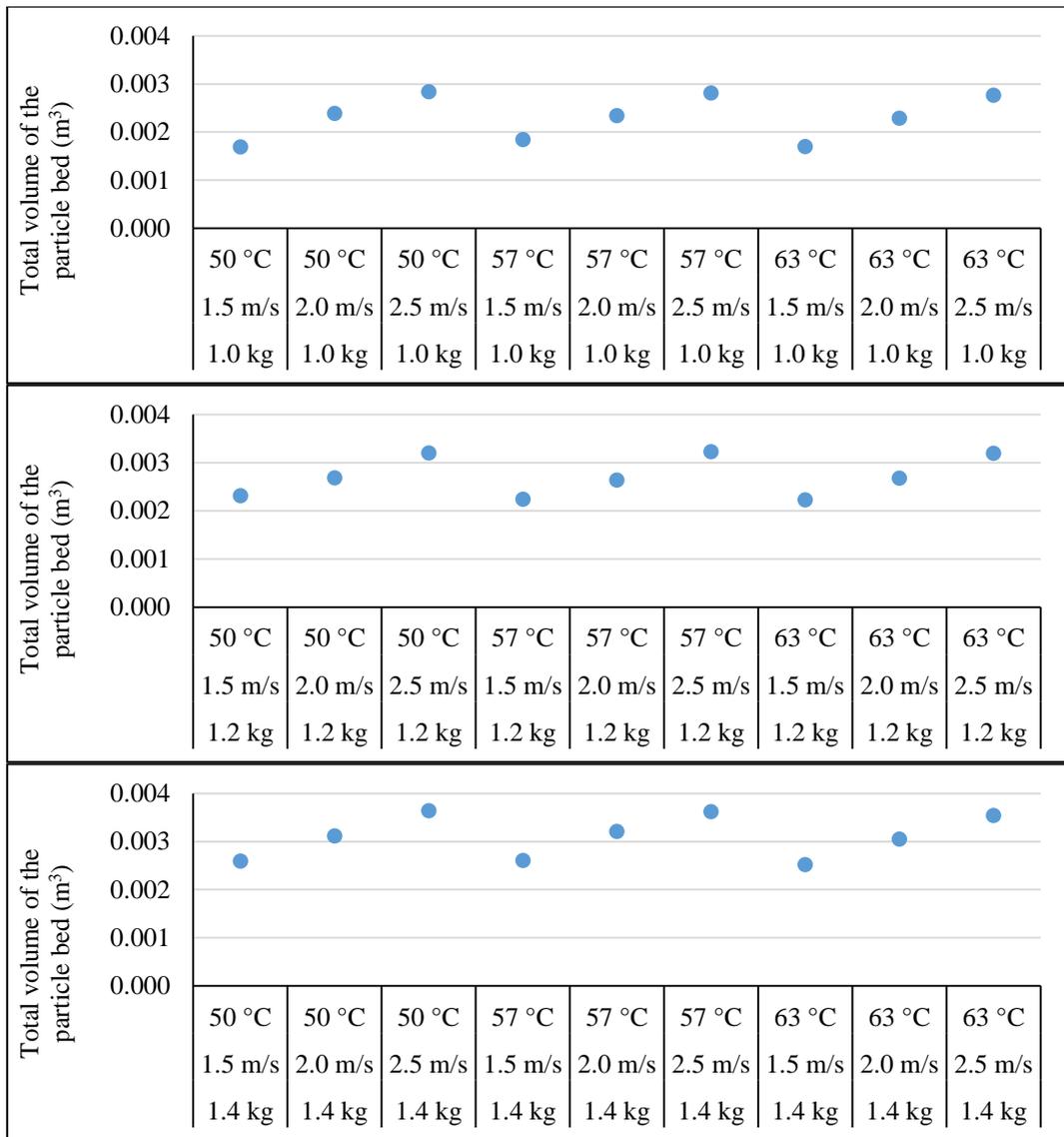
Figure 76. Total volume of the particle bed (m^3).
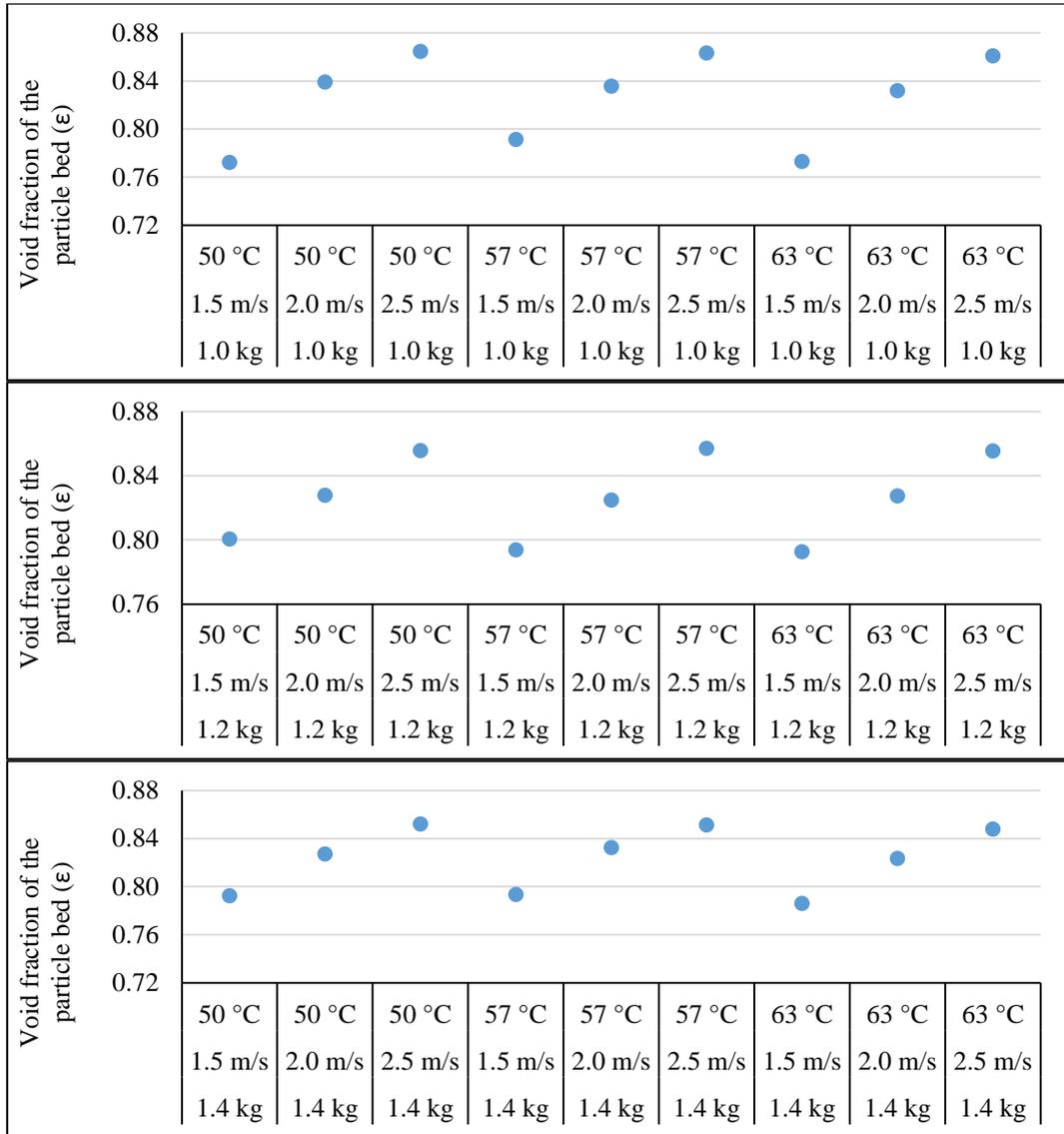
Figure 77. Void fraction of the particle bed.

7.2 Overall heat transfer coefficient

When the particle temperature does not change over time, it is considered that a temperature steady state is reached. At this state, the overall heat transferred from the air to the particles equals to the overall heat transferred from the particles to the fluidized bed wall.

The heat transferred from the air to the particles can be expressed as:

$$q_{ap} = h_{ap}A_{ap}\Delta T_{ap} \qquad \text{Eq. (67)}$$

Where q_{ap} is the overall heat flux from the air to the particles (W), h_{ap} is the heat transfer coefficient between the air and the particles $(W/m^2 \cdot K)$, A_{ap} is the contact

110

area between the air and the particles (m^2), ΔT_{ap} is the mean temperature difference between the air and the particles (K).

The heat transfer from the particles to the fluidized bed wall can be expressed as:

$$q_{pw} = h_{pw}A_{bed}\Delta T_{pw}$$

Eq. (68)

Where q_{pw} is the overall heat flux from the particles to the fluidized bed wall (W), h_{pw} is the heat transfer coefficient between the particles and the fluidized bed wall $(W/m^2 \cdot K)$, A_{bed} is the fluidized bed contact area (m^2), ΔT_{pw} is the mean temperature difference between the particles and the fluidized bed wall (K).

At the temperature steady state:

$$q_{ap} = q_{pw}$$

Eq. (69)

Which can be rewrite as:

$$h_{ap}A_{ap}\Delta T_{ap} = h_{pw}A_{bed}\Delta T_{pw}$$

Eq. (70)

Therefore, the ratio between the heat transfer coefficient from the air to a single particle and the heat transfer coefficient from the particles to the fluidized bed wall can be calculated as:

$$\eta = \frac{h_{ap}}{h_{pw}} = \frac{A_{bed}\Delta T_{pw}}{A_{ap}\Delta T_{ap}}$$

Eq. (71)

This ratio can be used to indicate the heat transfer performance of the fluidized bed.

A_{ap} is calculated as (Gunn, 1978):

$$A_{ap} = \frac{6(1-\varepsilon)}{D_{mean}}V_{bed}$$

Eq. (72)

Where ε is the void fraction of the particle bed, and D_{mean} is the mean particle diameter (m).

A_{bed} was calculated in the section 7.1.3.

Using the Eq. (71), the ratio between the heat transfer coefficient from the air to a single particle and the heat transfer coefficient from the particles to the fluidized bed wall can be calculated. The results are shown in Figure 78.

From the figures, it can be observed that η is significantly affected by the inlet air velocity, while the effect of the inlet air temperature and the loaded particle mass on η is not clear.
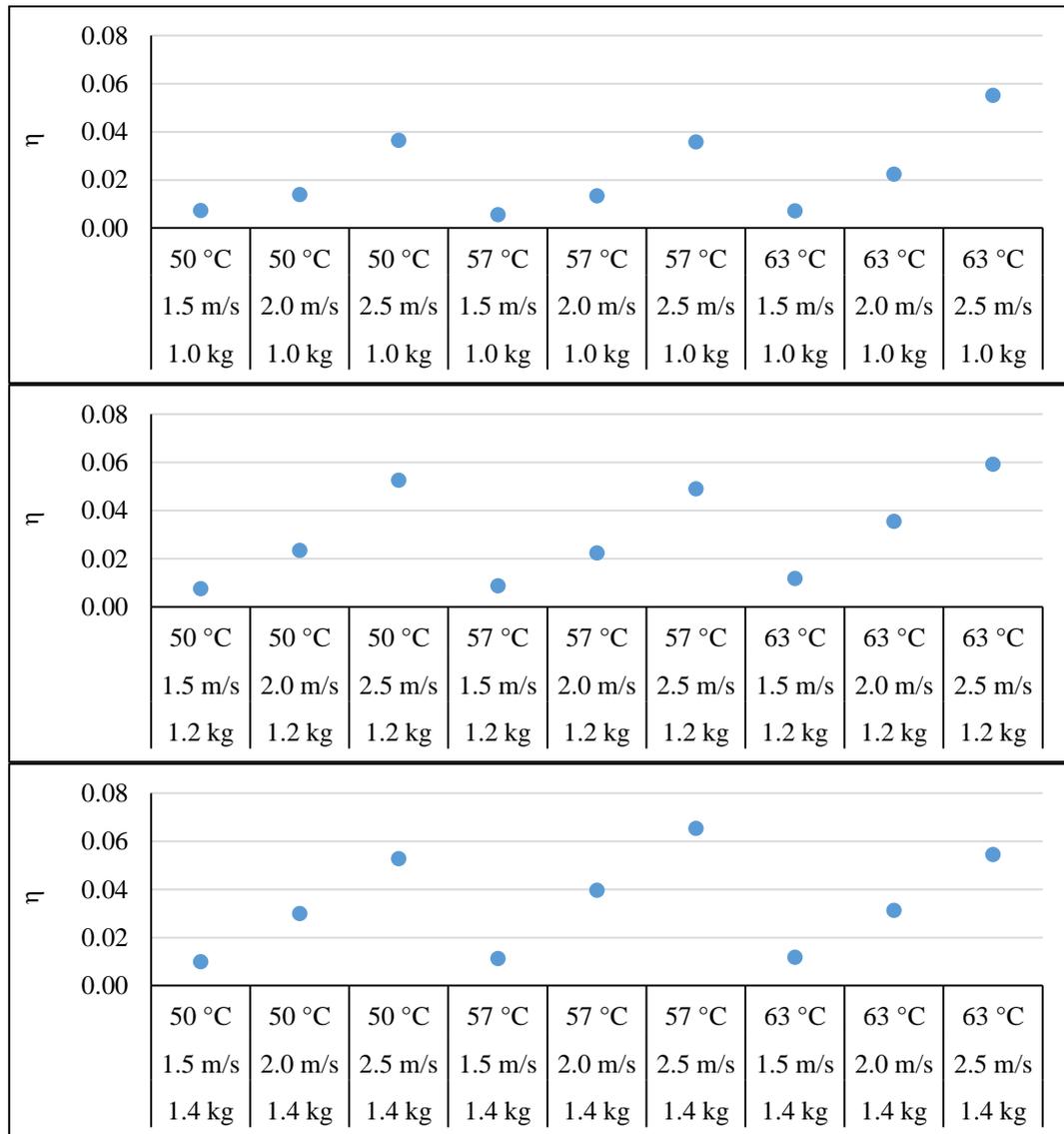
Figure 78. Calculated η.

In Figure 79, η is plotted against the void fraction of the particle bed ε. From the figure, it can be observed that generally, increase bed void fraction can optimize the particle heating process. It can also be seen that when the loaded particles mass was higher (1.0 kg, 1.2 kg, and 1.4 kg), the η was less affected by the void fraction (ε).

112

Figure 79. η and ε.
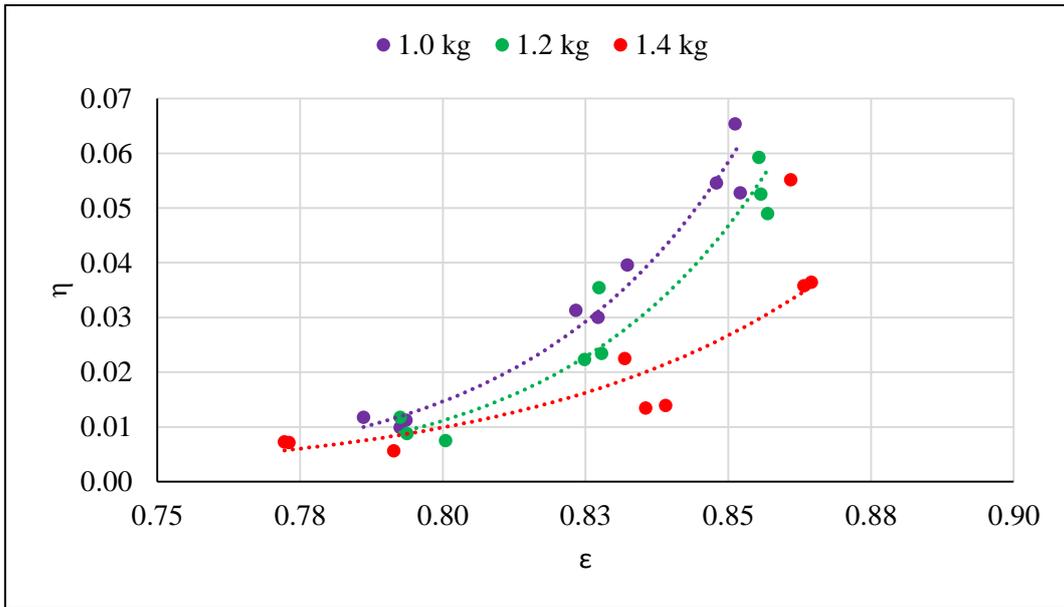
7.3 Two-compartment model

In order to correlate the heat transfer process between the air and the particles, and between the particles and the fluidized bed wall, a two-compartment model is developed.

In this model, particles are considered to circulate between a cold zone (closer to the fluidized bed wall) and a hot zone (away from the fluidized bed wall). In each zone, the particles are well-mixed.

At the beginning, a single particle is considered.

$$m_p^* C_{p,p} \frac{\Delta T}{dt} = h_H^* A_H^* \ (T_H - T^*) \qquad m_p^* C_{p,p} \frac{\Delta T}{dt} = h_C^* A_C^* (T^* - T_C)$$
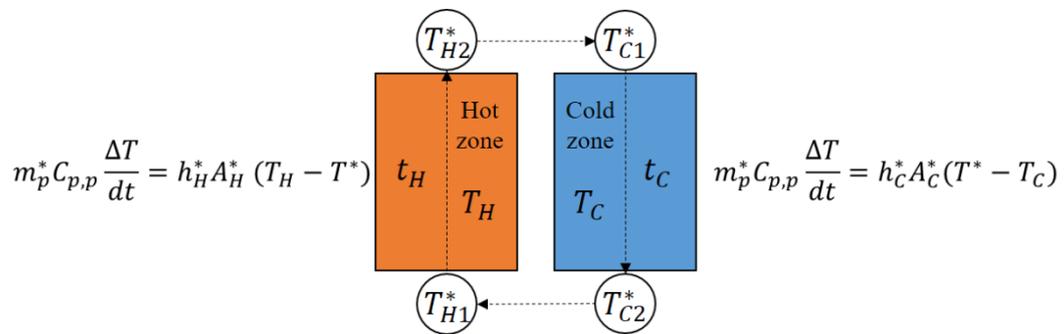
Figure 80. Two compartment model (single particle).

113

As shown in Figure 80, the temperature of the hot zone and the cold zone is denoted as T_H and T_C, respectively.

A particle enters the hot zone with temperature T_{H1}^* and leaves the hot zone with temperature T_{H2}^*. The time it spent in the hot zone is t_H. Then the temperature changing rate $\frac{\Delta T}{dt}$ of the particle within the hot zone can be expressed as:

$$m_p^* C_{p,p} \frac{\Delta T}{dt} = h_H^* A_H^* (T_H - T^*) \qquad \text{Eq. (73)}$$

Where m_p^* is the particle mass (kg), $C_{p,p}$ is the specific heat capacity of the particle $(J/kg \cdot K)$, h_H^* is the heat transfer coefficient between the hot zone and the particle $(W/m^2 \cdot K)$, A_H^* is the heat transfer area between the hot zone and the particle (m^2), T^* is the instantaneous particle temperature (K).

A particle enters the cold zone with temperature T_{C1}^* and leaves the hot zone with temperature T_{C2}^*. The time it spent in the hot zone is t_C. Then the temperature changing rate $\frac{\Delta T}{dt}$ of the particle within the hot zone can be expressed as:

$$m_p^* C_{p,p} \frac{\Delta T}{dt} = h_C^* A_C^* (T^* - T_C) \qquad \text{Eq. (74)}$$

Where m_p^* is the particle mass (kg), $C_{p,p}$ is the specific heat capacity of the particle $(J/kg \cdot K)$, h_C^* is the heat transfer coefficient between the hot zone and the particle $(W/m^2 \cdot K)$, A_C^* is the heat transfer area between the hot zone and the particle (m^2), T^* is the instantaneous particle temperature (K).

Integrating Eq. (73) and Eq. (74) separately, following expression can be obtained:

$$\begin{cases} \dfrac{T_{H2}^* - T_H}{T_{H1}^* - T_H} = e^{-t_H / \left(\frac{m_p^* C_{p,p}}{h_H^* A_H^*} \right)} \\[4mm] \dfrac{T_{C2}^* - T_C}{T_{C1}^* - T_C} = e^{-t_C / \left(\frac{m_p^* C_{p,p}}{h_C^* A_C^*} \right)} \end{cases} \qquad \text{Eq. (75)}$$

Which is,

$$\begin{cases} \dfrac{t_H}{\left(\dfrac{m_p^* C_{p,p}}{h_H^* A_H^*}\right)} = -\ln\left(\dfrac{T_{H2}^* - T_H}{T_{H1}^* - T_H}\right) \\[4mm] \dfrac{t_C}{\left(\dfrac{m_p^* C_{p,p}}{h_C^* A_C^*}\right)} = -\ln\left(\dfrac{T_{C2}^* - T_C}{T_{C1}^* - T_C}\right) \end{cases}$$

Eq. (76)

By comparing these two expression, following relationship can be obtained:

$$\frac{t_H}{t_C}\frac{h_H^*}{h_C^*}\frac{A_H^*}{A_C^*} = \frac{\ln\left(\dfrac{T_{H2}^* - T_H}{T_{H1}^* - T_H}\right)}{\ln\left(\dfrac{T_{C2}^* - T_C}{T_{C1}^* - T_C}\right)}$$

Eq. (77)

If following items are defined:

$$\kappa_t = \frac{t_H}{t_C}$$

Eq. (78)

$$\kappa_h = \frac{h_H^*}{h_C^*}$$

Eq. (79)

$$\kappa_A = \frac{A_H^*}{A_C^*}$$

Eq. (80)

$$\xi = \frac{\ln\left(\dfrac{T_{H2}^* - T_H}{T_{H1}^* - T_H}\right)}{\ln\left(\dfrac{T_{C2}^* - T_C}{T_{C1}^* - T_C}\right)}$$

Eq. (81)

ξ is originally defined in this thesis to integrate the temperatures of the hot zone, the cold zone, and the particles. It is a value that can be measured experimentally and can be used to indicate the heat transfer processes in the hot zone and in the cold zone.

Then Eq. (77) can be rewrite as:

$$\kappa_t \kappa_h \kappa_A = \xi$$

Eq. (82)

When κ_A is higher, the contact area between the hot zone and the particle is larger than the contact area between the cold zone the particle. When κ_h is higher, the heat transfer coefficient between the hot zone and the particle is higher than the heat transfer coefficient between the cold zone and the particle. When κ_t is higher, the time that the particle spent in the hot zone is longer than the time that the particle

spent in the cold zone. When ξ is increased, the heat transfer performance between the hot zone and the particle is improved more than the heat transfer performance between the cold zone and the particle.

Ideally, the values of the items in Eq. (82) are different for different particles in the fluidized bed. For any particle denoted as $particle_i$:

$$\kappa_t(particle_i)\kappa_h(particle_i)\kappa_A(particle_i) = \xi(particle_i) \qquad \text{Eq. (83)}$$

For simplification, it is assumed that there is a particle exist that can be used to represent all particles. When the particle reaches a temperature steady state, following relationship is obtained:

$$\begin{cases} T_{H1}^* = T_{C2}^* \\ T_{H2}^* = T_{C1}^* \\ T_{H1}^* < T_{H2}^* \\ T_{C1}^* > T_{C2}^* \end{cases} \qquad \text{Eq. (84)}$$

At a temperature steady state, within the $100\ s$ measurement time, the average particle temperature and the standard deviation were denoted as T_{avg}^* and T_{std}^*, respectively. Since the measured particles included the particles in the hot zone and the particles in the cold zone, it is assumed that the particle was heated from $(T_{avg}^* - T_{std}^*)$ to $(T_{avg}^* + T_{std}^*)$ in the hot zone and cooled from $(T_{avg}^* + T_{std}^*)$ to $(T_{avg}^* - T_{std}^*)$ in the cold zone. Then, following expression was used:

$$\begin{cases} T_{H1}^* = T_{C2}^* = T_{avg}^* - T_{std}^* \\ T_{H2}^* = T_{C1}^* = T_{avg}^* + T_{std}^* \end{cases} \qquad \text{Eq. (85)}$$

Then Eq. (81) can be rewrite as:

$$\xi = \frac{\ln\left(\dfrac{T_{avg}^* + T_{std}^* - T_H}{T_{avg}^* - T_{std}^* - T_H}\right)}{\ln\left(\dfrac{T_{avg}^* - T_{std}^* - T_C}{T_{avg}^* + T_{std}^* - T_C}\right)} \qquad \text{Eq. (86)}$$

When it is assumed that hot zone is in the air and cold zone is on the fluidized bed wall, T_H and T_C is the inlet air temperature and the fluidized bed wall temperature, respectively. In Figure 81, the calculated ξ is plotted against the void fraction ε.

Figure 81. ξ and ε.
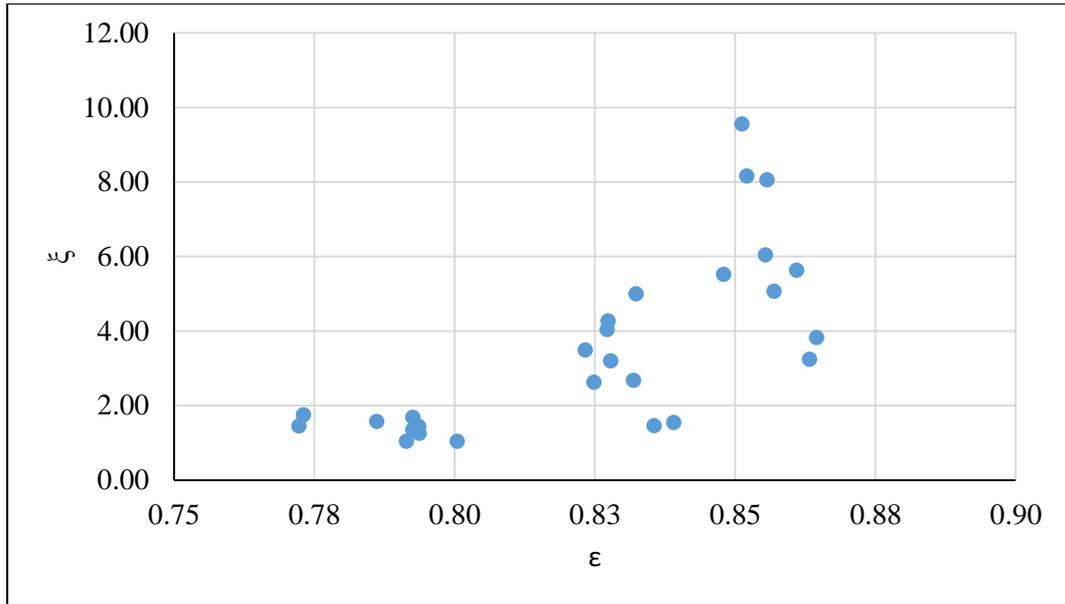
From the figure, it can be found that generally increase the void fraction of the particle bed can improve heat transfer between the hot zone and the particles.

In the section 7.2, the ratio of the overall heat transfer coefficients between the particles and the air, and between the particles and the fluidized bed wall was calculated. In the literature, there are many models for calculating the two heat transfer coefficients. From the Eq. (82), it is known that when the different value of κ_h is used, the product of κ_A and κ_t is also different. This is because that the value of κ_h, κ_A, and κ_t depend on the particle fluidization. In this thesis, ξ is compared with four different values of κ_h (κ_{h1}, κ_{h2}, κ_{h3}, and κ_{h4}).

κ_{h1} is the ratio of the overall heat transfer coefficients calculated in the section 7.2:

$$\kappa_{h1} = \eta \qquad \text{Eq. (87)}$$

In terms of κ_{h2}, the heat transfer model between the air and the particles used is the model suggested by Ranz (Ranz & Marshall, 1952). Patil et al., (2015) developed a model and tried different the heat transfer coefficient between the particles and the fluidized bed wall. They found that 350 $(W/m^2 \cdot K)$ can give the best fit between their experimental data and modelling results. Then the value of κ_{h2} is calculated as:

$$\kappa_{h2} = \frac{\frac{2 + 1.8 Re_p^{1/2} Pr^{1/3}}{D} k_a}{350}$$

<div align="right">Eq. (88)</div>

In terms of κ_{h3}, the heat transfer model between the air and the particles used is the model suggested by Ranz (Ranz & Marshall, 1952), the heat transfer model between the particles and the fluidized bed used is the model suggested by Kunii and Levenspiel, (1991).

$$\kappa_{h3} = \frac{2 + 1.8 Re_p^{1/2} Pr^{1/3}}{(1 - \varepsilon)(5.0 + 0.05 Pr Re_p)}$$

<div align="right">Eq. (89)</div>

In terms of κ_{h4}, the heat transfer model between the air and the particles used is the model suggested by Gunn (1978), the heat transfer model between the particles and the fluidized bed used is the model suggested by Kunii and Levenspiel, (1991).

$$\kappa_{h4} = \frac{(7 - 10\varepsilon + 5\varepsilon^2)\left(1 + 0.7 Re_p^{0.2} Pr^{\frac{1}{3}}\right) + (1.33 - 2.4\varepsilon + 1.2\varepsilon^2) Re_p^{0.7} Pr^{1/3}}{(1 - \varepsilon)(5.0 + 0.05 Pr Re_p)}$$

<div align="right">Eq. (90)</div>

Figure 82, Figure 83, Figure 84, and Figure 85 compares ξ with κ_{h1}, κ_{h2}, κ_{h3}, and κ_{h4}, respectively.
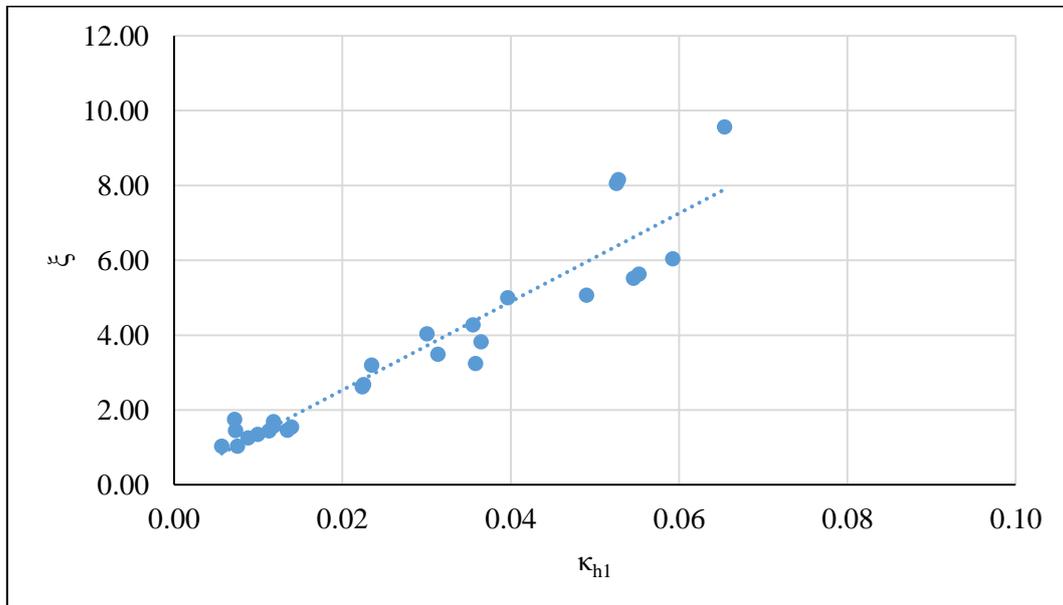
Figure 82. Compare ξ and κ_{h1}.
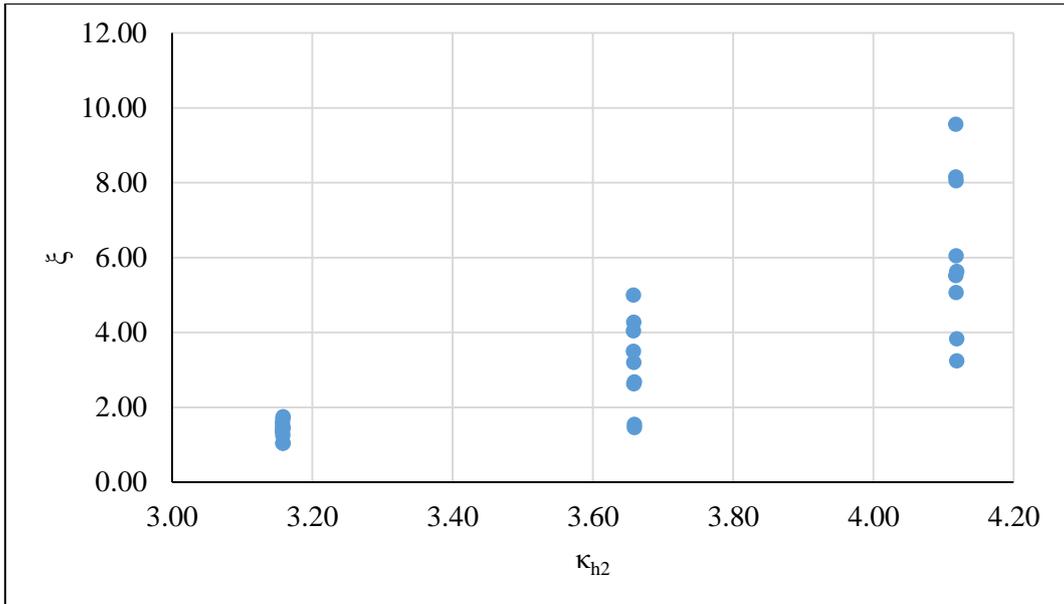
Figure 83. Compare ξ and κ_{h2}.
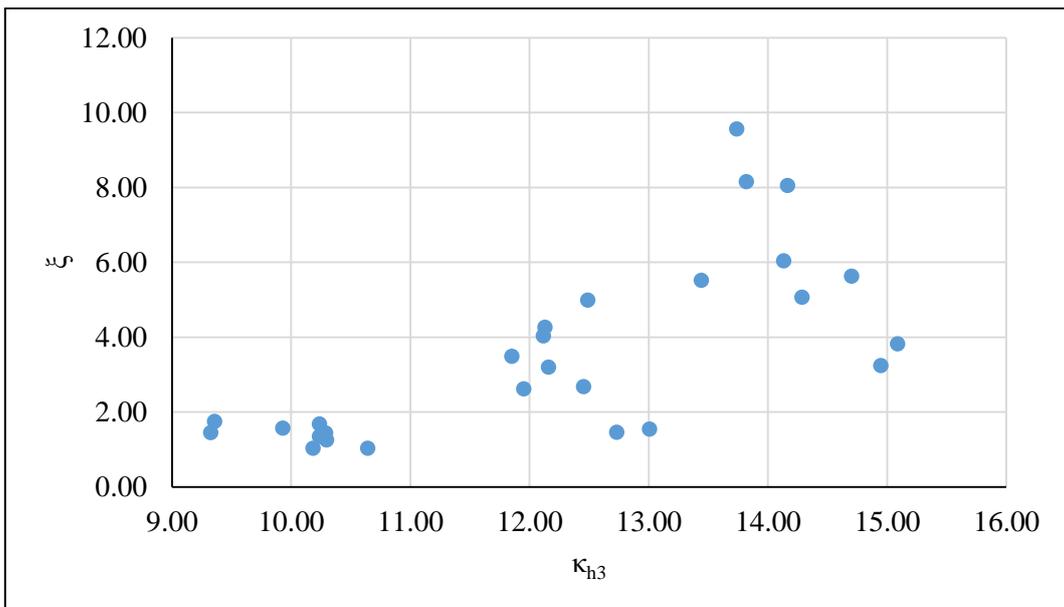
Figure 84. Compare ξ and κ_{h3}.
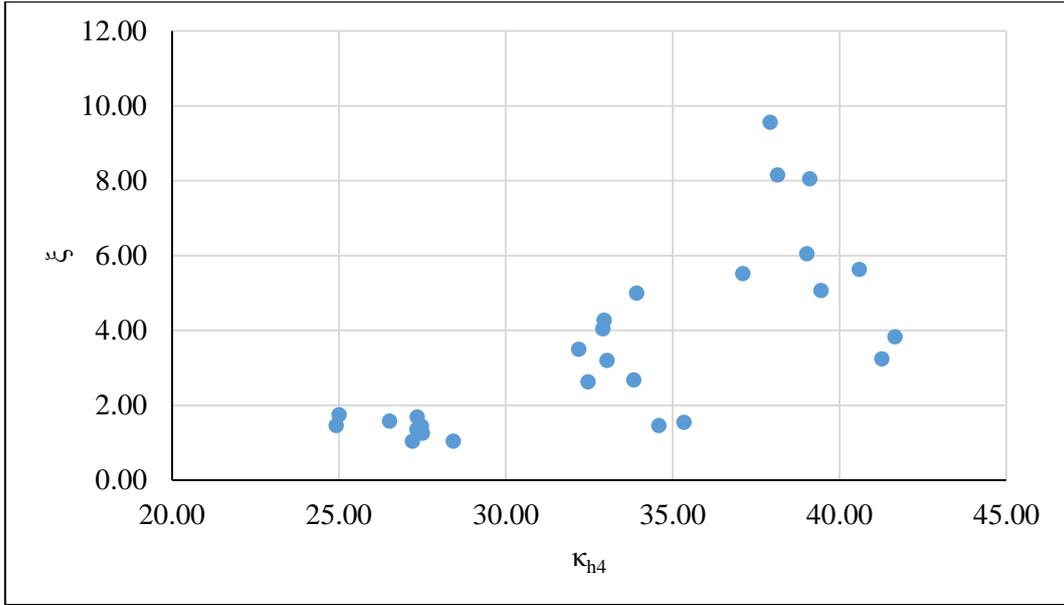
Figure 85. Compare ξ and κ_{h4}.

From the figures, it can be observed that when κ_{h1}, κ_{h2}, κ_{h3}, and κ_{h4} is increased respectively, ξ is increased as well.

From the Eq. (82), it is known that:

$$\kappa_h = \frac{\xi}{\kappa_A \kappa_t}$$

Eq. (91)

It is expected that when a particle is contacted with other particles, its contact area between the hot zone and the particle will be decreased. The contact area between the fluidized bed wall and the particle should be only affected by the particle itself and can be assumed as a constant. From the equation used by Gunn (1978) ($A_{ap} = \frac{6(1-\varepsilon)}{D_{mean}} V_{bed}$), it is known that $(1 - \varepsilon)$ is correlated to the particle diameter (D_{mean}) in the same order, then it is deduced that $(1 - \varepsilon)^2$ is correlated to the (κ_A) in the same order. Since the particle fluidization is affected by the inlet air velocity, it is assumed that the time ratio κ_t is correlated to the particle Reynold number (Re_p) in the same order.

Then the value of κ_h can be estimated as:

$$\kappa_{h0} = \frac{\xi}{(1 - \varepsilon)^2 Re_p}$$

Eq. (92)

120

Figure 86, Figure 87, and Figure 88 compares the calculated κ_{h0} with κ_{h1}, κ_{h2}, κ_{h3}, and κ_{h4} respectively.
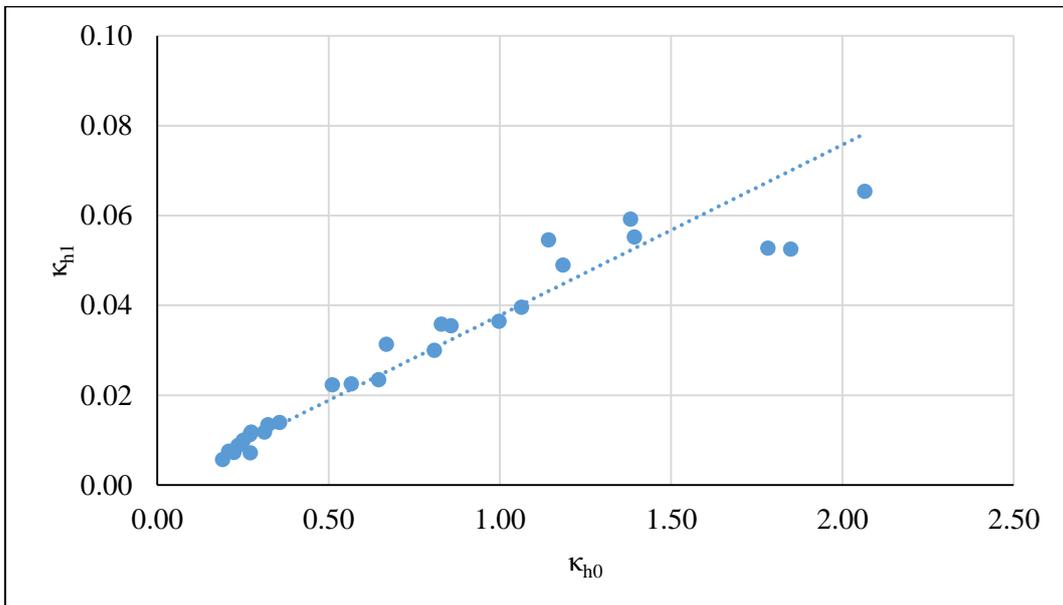
Figure 86. κ_{h0} and κ_{h1}.
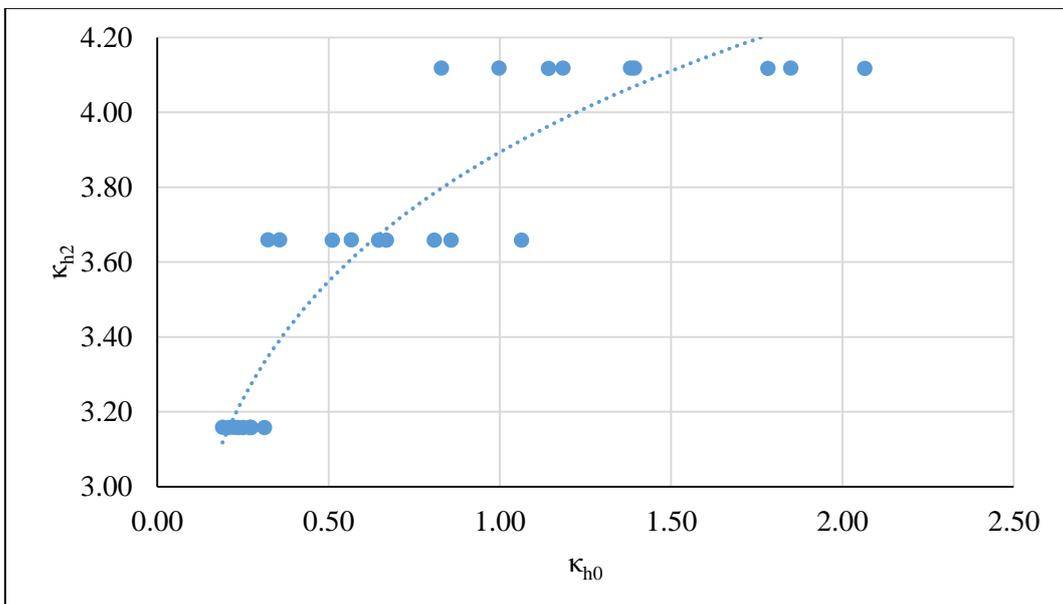
Figure 87. κ_{h0} and κ_{h2}.

Figure 88. κ_{h0} and κ_{h3}

Figure 89. κ_{h0} and κ_{h4}
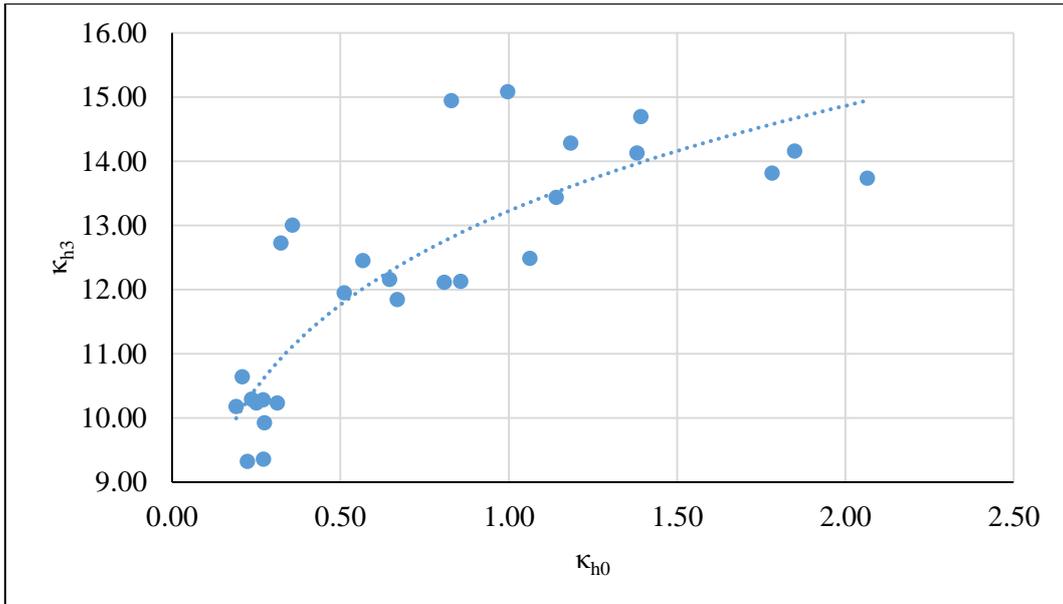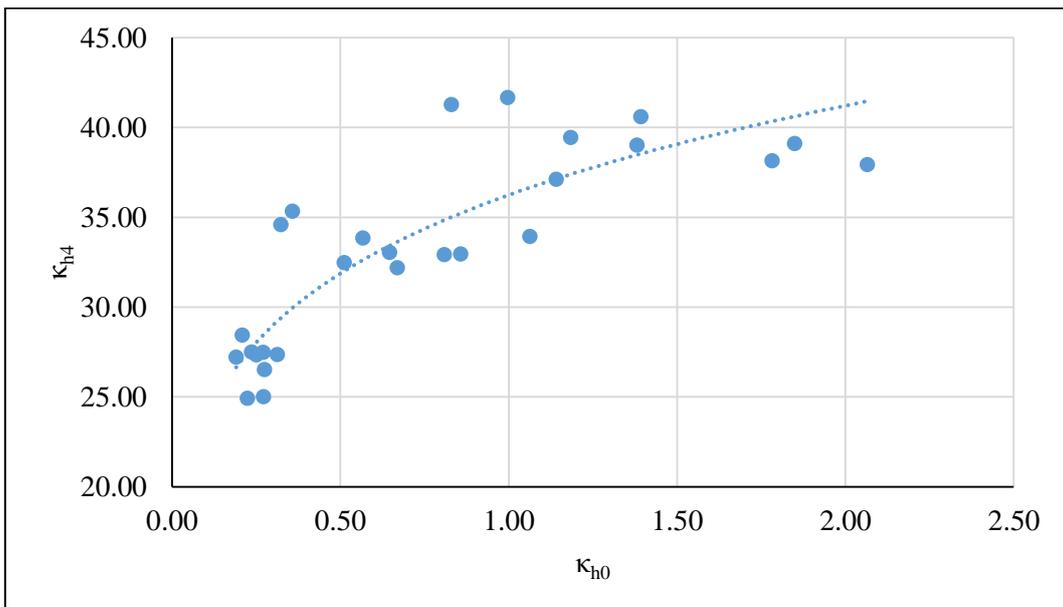
From the figures, it can be observed that the relationships between κ_{h0} and κ_{h1}, between κ_{h0} and κ_{h2}, between κ_{h0} and κ_{h3}, and between κ_{h0} and κ_{h4} can be fitting using one form:

$$y = ax^b \qquad \text{Eq. (93)}$$

Where a, b represents the consideration of the void fraction and the particle Reynolds number.

The fitting curve can be obtained as:

$$\begin{cases} \kappa_{h0} = \dfrac{\xi}{(1-\varepsilon)^2 Re_p} = 0.03\kappa_{h1}^{0.85} \\[2mm] \kappa_{h0} = \dfrac{\xi}{(1-\varepsilon)^2 Re_p} = 4.08\kappa_{h2}^{0.13} \\[2mm] \kappa_{h0} = \dfrac{\xi}{(1-\varepsilon)^2 Re_p} = 13\kappa_{h3}^{0.17} \\[2mm] \kappa_{h0} = \dfrac{\xi}{(1-\varepsilon)^2 Re_p} = 35\kappa_{h4}^{0.18} \end{cases} \qquad \text{Eq. (94)}$$

Therefore, it is concluded that when the void fraction and the particle Reynolds number is given, the heat transfer coefficients between the hot zone (the air) and the particles and between the particles and the cold zone (the fluidized bed wall) are correlated. The relationship between them is depends on how the void fraction and the particle Reynolds number are related to the contact area between the particle and the zones (hot and cold) and the time that the particle spent in the zones.

7.4 Summary

In this chapter, temperatures of the inlet air, the exit air, the particles, the fluidized bed wall, and the ambient at a several temperature steady states were online measured.

The bed height, the contact area between the particles and the fluidized bed wall, and the void fraction of the particle bed was calculated respectively. It was seen from the results that when the inlet air velocity or the loaded particle mass was increased, the bed height was increased, while the effect of the inlet air temperature on the bed height was negligible. When the inlet air velocity was increased, the void fraction of the particle bed was increased, while the effect of the inlet air temperature and the loaded particle mass on the void fraction was negligible.

By calculation, it was found that increase the void fraction of the particle bed can increase the ratio between the overall heat transfer coefficient from the air to the particles and the overall heat transfer coefficient from the particles to the fluidized bed wall.

By suggesting that at the temperature steady state, the particles are circulating between a hot zone and a cold zone, a two-compartment model is developed. By comparing the heat transfer coefficients between the hot zone and the cold zone with the overall heat transfer coefficients and the heat transfer coefficients calculated from the models in the literature, it was found that the two heat transfer coefficients are correlated. The relationship between them is depends on how the void fraction and the particle Reynolds number are related to the contact area between the particle and the zones (hot and cold) and the time that the particle spent in the zones.

8 Conclusion

In the experimental setup, a thermal camera was used to online monitor the temperature of the particles in a cylindrical 3D fluidized bed, while previous researchers used a flat pseude-2D fluidized bed.

In the conversion of the thermal images to the particle temperature, it was found that the focus of the thermal camera and the movement of the particles can affect the measured particle temperature. It was also found that when the air temperature is lower than 75 °C, the measured particle temperature will not be affected. Therefore, in the particle identification, the size and shape of the particles were calibrated using an offline method and were used to identify the clear particles in the thermal images (region-based image segmentation), while previous researchers didn't use image segmentation or used threshold-based image segmentation (the output is difficult to be evaluated).

In the particle temperature calibration, previous researchers used two methods: placing the particles on a hot plate outside the fluidized bed and using a thermocouple probe to measure the particle temperature, or fixing a particle directly on the tip of a thermocouple probe inside the fluidized bed. However, it is concerned that the measured temperature of the particles can be affected by the air surrounding the particles. Therefore, in addition to the two methods, a new calibration method was introduced in this thesis: particles were fluidized inside a thermal insulated fluidized bed, then at temperature steady state, the particle temperature was same as the temperatures of the air and the fluidized bed wall.

In the experimental work, this thesis distinguished the temperatures of the air, the particles, the fluidized bed wall and the ambient in the particle heating process and studied the effect of the inlet air velocity, the inlet air temperature, and the loaded particle mass on the particle heating process. Due to the improved particle identification and particle temperature calibration, the measured particle temperature is more accurate than previous researchers.

In the heat transfer mechanism, a two-compartment model was developed in this thesis to link the heat transfer between the particles and the air, and the heat transfer between the particles and the fluidized bed wall. In this model, it was proposed to use

the contact area between the particles and the two zones (hot and cold), the residence time of the particles in the two zones, and the heat transfer coefficients between the particles and the two zones to describe the temperature of the particles in a fluidized bed.

9 Future work

Using thermal cameras with higher frame rate, smaller detector size and shorter detector time constant are expected to improve the accuracy of the particle temperature measurement and to allow the investigation of the online particle temperature distribution.

After the particle temperature distribution can be measured accurately, the results can be used in the two-compartment to calculate the particle residence time in the hot and cold zones. For calculation, a numerical bootstrap algorithm developed by Prof. Hounslow can be used.

When a thermal camera with high resolution is used in the future, a particle in the thermal image can be represented by numerous pixels (for example, several thousand pixels). Then it will be possible to use a complex image segmentation to identify the pixels representing the particles in the thermal images based on the texture of the particle. This texture is related to the surface of the particle and can be calibrated offline. It is expected that the texture-based image segmentation can online identify particles within different size classes.

It is also interesting to develop a CFD-DEM model to predict the particle temperature. The modelling results can be compared with the measured particle temperature and the results calculated from the two-compartment model (numerical model). The advantage of using a CFD-DEM model is that the air flow and the particle collision can be considered in detail. The disadvantage of using a CFD-DEM model is that the amount of the particles and the processing time length are limited by the computer power. The advantage of using a numerical model is that it can be used predict a large amount of the particles and the processing time length can be long enough. The disadvantage of using a numerical model is that the air flow and the particle collision cannot be considered in detail. It is therefore necessary to compare the prediction results of the two models with the measured particle temperature distribution over time.

10 Reference

Baeyens, J., & Goossens, W. R. A. (1973). Some aspects of heat transfer between a vertical wall and a gas fluidized bed. *Powder Technology*, 8, 91–96.

Bao, Z., Duan, L., Wu, K., & Zhao, C. (2020). An investigation on the heat transfer model for immersed horizontal tube bundles in a pressurized fluidized bed. *Applied Thermal Engineering*, 170.

Borodulya, V. A., Teplitsky, Y. S., Markevich, I. I., Hassan, A. F., & Yeryomenko, T. P. (1991). Heat transfer between a surface and a fluidized bed: consideration of pressure and temperature effects. *International Journal of Heat and Mass Transfer*, 34(1), 47–53.

Brown, S. L., & Lattimer, B. Y. (2013). Transient gas-to-particle heat transfer measurements in a spouted bed. *Experimental Thermal and Fluid Science*, 44, 883–892.

Budzier, H., & Gerlach, G. (2011). *Thermal Infrared Sensors : Theory, Optimisation and Practice*. Chichester, UK: John Wiley & Sons, Incorporated.

Calderon De Anda, J., Wang, X. Z., & Roberts, K. J. (2005). Multi-scale segmentation image analysis for the in-process monitoring of particle shape with batch crystallisers. *Chemical Engineering Science*, 60(4), 1053–1065.

Canny, J. (1986). A Computational Approach to Edge Detection. *IEEE Transactions on Pattern Analysis and Machine Intelligence*, PAMI-8(6), 679–698.

Childs, P. R. N., Greenwood, J. R., & Long, C. A. (2000). Review of temperature measurement. *Review of Scientific Instruments*, 71(8), 2959–2978.

Chitester, D. C., Kornosky, R. M., Fan, L. S., & Danko, J. P. (1984). Characteristics of fluidization at high pressure. *Chemical Engineering Science*, 39(2), 253–261.

Chow, C. K., & Kaneko, T. (1972). Automatic boundary detection of the left ventricle from cineangiograms. *Computers and Biomedical Research*, 5(4), 388–410.

Cundall, P. A., & Strack, O. D. L. (1979). A discrete numerical model for granular assemblies. *Géotechnique*, 29(1), 47–65.

Davidson, J., & Harrison. (1971). *Fluidization*. London: Academic Press.

Decker, N., & Glicksman, L. R. (1983). Heat tranfer in fluidized beds of large particles. *International Journal of Heat and Mass Transfer*, 26(9), 1307–1320.

Ergun, S. (1952). Fluid flow through packed columns. *Chemical Engineering Science*.

Frei, M., & Kruis, F. E. (2020). Image-based size analysis of agglomerated and partially sintered particles via convolutional neural networks. *Powder Technology*, 360, 324–336.

Fu, K. S., & Mui, J. K. (1981). A survey on image segmentation. *Pattern Recognition*, 13(1), 3–16.

Ganzha, V. L., Upadhyay, S. N., & Saxena, S. C. (1982). A mechanistic theory for heat transfer between fluidized beds of large particles and immersed surfaces. *International Journal of Heat and Mass Transfer*, 25(10), 1531–1540.

Geldart, D. (1973). Types of gas fluidization. *Powder Technology*, 7(5), 285–292.

Gray, S. B. (1971). Local Properties of Binary Images in Two Dimensions. *IEEE Transactions on Computers*, C–20(5), 551–561.

Grewal, N. S., & Saxena, S. C. (1980). Heat transfer between a horizontal tube and a gas-solid fluidized bed. *International Journal of Heat and Mass Transfer*, 23(11), 1505–1519.

Gunn, D. J. (1978). Transfer of heat or mass to particles in fixed and fluidised beds. *International Journal of Heat and Mass Transfer*, 21(4), 467–476.

Gunn, D. J., & De Souza, J. F. C. (1974). Heat transfer and axial dispersion in packed beds. *Chemical Engineering Science*, 29(6), 1363–1371.

Gunn, D. J., & Khalid, M. (1975). Thermal dispersion and wall heat transfer in packed beds. *Chemical Engineering Science*, 30(2), 261–267.

Haider, A., & Levenspiel, O. (1989). Drag coefficient and terminal velocity of spherical and nonspherical particles. *Powder Technology*, 58(1), 63–70.

Han, J.-C. (2012). *Analytical heat transfer*. Boca Raton, Florida ; London, England ; New York; CRC Press.

Johnson, J. B. (1928). Thermal Agitation of Electricity in Conductors. *Physical Review*, 32(1), 97–109.

Kim, S. W., Ahn, J. Y., Kim, S. D., & Hyun Lee, D. (2003). Heat transfer and bubble characteristics in a fluidized bed with immersed horizontal tube bundle. *International Journal of Heat and Mass Transfer*, 46(3), 399–409.

Kittler, J., & Illingworth, J. (1986). Minimum error thresholding. *Pattern Recognition*, 19(1), 41–47.

Kloss, C., Goniva, C., Hager, A., Amberger, S., & Pirker, S. (2012). Models, algorithms and validation for opensource DEM and CFD-DEM. *Progress in Computational Fluid Dynamics, An International Journal*, 12(2/3), 140.

Kruse, P. W. (2001). *Uncooled Thermal Imaging Arrays, Systems, and Applications*. Bellingham, Washington USA: SPIE press.

Kudo, Y., Yasuda, M., & Matsusaka, S. (2020). Effect of particle size distribution on flowability of granulated lactose. *Advanced Powder Technology*, 31(1), 121–127.

Kunii, D., & Levenspiel, O. (1991). *Fluidization Engineering* (2nd ed.). London : Butterworths.

Leva, M. (1959). *Fluidization*. New York: McGraw-Hill.

Li, Z., Janssen, T. C. E., Buist, K. A., Deen, N. G., van Sint Annaland, M., & Kuipers, J. A. M. (2017). Experimental and simulation study of heat transfer in fluidized beds with heat production. *Chemical Engineering Journal*, 317, 242–257.

Litster, J., & Ennis, B. (2004). *The Science and Engineering of Granulation Processes* (Softcover, Vol. 15). Dordrecht Springer, 2004.

Malek, M. A., & Lu, B. C.-Y. (1964). Heat transfer in spouted beds. *The Canadian Journal of Chemical Engineering*, 42(1), 14–20.

Mickley, H. S., & Fairbanks, D. F. (1955). Mechanism of heat transfer to fluidized beds. *AIChE Journal*, 1(3), 374–384.

Modest, M. F. (2003). *Radiative heat transfer*. New York ; London : McGraw-Hill.

Morl, L., Heinrich, S., & Peglow, M. (2007). Fluidized bed spray granulation. In A. D. Salman, M. J. Hounslow, & J. P. K. Seville (Eds.), *Handbook of Powder Technology* (pp. 21–188). Oxford:Elsevier,2007.

Nakagawa, Y., & Rosenfeld, A. (1979). Some experiments on variable thresholding. *Pattern Recognition*, 11(3), 191–204.

Nyquist, H. (1928). Thermal Agitation of Electric Charge in Conductors. *Physical Review*, 32(1), 110–113.

Otsu, N. (1979). A Threshold Selection Method from Gray-Level Histograms. *IEEE Transactions on Systems, Man, and Cybernetics*, 9(1), 62–66.

Pal, N. R., & Pal, S. K. (1993). A review on image segmentation techniques. *Pattern Recognition*, 26(9), 1277–1294.

Pan, Z., & Atungulu, G. G. (2010). *Infrared Heating for Food and Agricultural Processing*. CRC Press LLC.

Park, J., & Mackay, S. (2003). *Practical data acquisition for instrumentation and control systems*. Amsterdam: London : Elsevier, 2003.

Park, R., Carroll, R., Burns, G., Desmaris, R., Hall, F., Herzkovitz, M., … Wang, T. (1993). *Manual on the Use of Thermocouples in Temperature Measurement* (Fourth Edi). ASTM International.

Patil, A. V., Peters, E. A. J. F., & Kuipers, J. A. M. (2015a). Comparison of CFD–DEM heat transfer simulations with infrared/visual measurements. *Chemical Engineering Journal*, 277, 388–401.

Patil, A. V., Peters, E. A. J. F., & Kuipers, J. A. M. (2015b). Comparison of CFD–DEM heat transfer simulations with infrared/visual measurements. *Chemical Engineering Journal*, 277, 388–401.

Patil, A. V., Peters, E. A. J. F., Sutkar, V. S., Deen, N. G., & Kuipers, J. A. M. (2015). A study of heat transfer in fluidized beds using an integrated DIA/PIV/IR technique. *Chemical Engineering Journal*, 259, 90–106.

Petrovic, L. J., Thodos, G., & Illinois, E. (1968). Effectiveness Factors for Heat Transfer in Fluidized Beds. *The Canadian Journal of Chemical Engineering*, 46, 114–118.

Planck, M. (1901). Ueber das Gesetz der Energieverteilung im Normalspectrum. *Annalen Der Physik*, 309(3), 553–563.

Pollock, D. D. (1971). *The Theory and Properties of Thermocouple Elements*. (D. Pollock,Ed.), *ASTM Special Technical Publication*. Philadelphia: ASTM International.

Rajab, M. I., Woolfson, M. S., & Morgan, S. P. (2004). Application of region-based segmentation and neural network edge detection to skin lesions. *Computerized Medical Imaging and Graphics*, 28(1–2), 61–68.

Ranz, W. E., & Marshall, W. R. (1952). Evaporation From Drops. *Chemical Engineering Progress*, 48(3), 141–146.

Rhodes, M. J. (2008). *Introduction to Particle Technology*. (M.J. Rhodes,Ed.) (2nd ed.). Hoboken, N.J. : Wiley ; Chichester : John Wiley distributor, 2008.

Saha, R., Bajger, M., & Lee, G. (2017). Circular shape constrained fuzzy clustering (CiscFC) for nucleus segmentation in Pap smear images. *Computers in Biology and Medicine*, 85(December 2016), 13–23.

Saxena, S. C., & Ganzha, V. L. (1984). Heat transfer to immersed surfaces in gas-fluidized beds of large particles and powder characterization. *Powder Technology*, 39(2), 199–208.

Serth, R. W., & Lestina, T. G. (2014). *Process Heat Transfer* (2nd ed.). Oxford, UK: Elsevier.

Sutkar, V. S., Deen, N. G., Patil, A. V., Peters, E. A. J. F., Kuipers, J. A. M., Salikov, V., … Heinrich, S. (2015). Experimental study of hydrodynamics and thermal behavior of a pseudo-2D spout-fluidized bed with liquid injection. *American Institute of Chemical Engineers*, 61(4), 1146–1159.

Taxt, T., Flynn, P. J., & Jain, A. K. (1989). Segmentation of document images. *IEEE Transactions on Pattern Analysis and Machine Intelligence*, 11(12), 1322–1329.

Tsuji, T., Miyauchi, T., Oh, S., & Tanaka, T. (2010). Simultaneous Measurement of Particle Motion and Temperature in Two-Dimensional Fluidized Bed with Heat Transfer. *KONA Powder and Particle Journal*, 28(28), 167–179.

Turton, R., & Clark, N. N. (1987). An explicit relationship to predict spherical particle terminal velocity. *Powder Technology*, 53(2), 127–129.

Valenzuela, J. A., & Glicksman, L. R. (1984). An experimental study of solids mixing in a freely bubbling two-dimensional fluidized bed. *Powder Technology*, 38(1), 63–72.

van Heerden, C., Nobel, A. P. P., & van Krevelen, D. W. (1953). Mechanism of Heat Transfer in Fluidized Beds. *Industrial & Engineering Chemistry*, 45(6), 1237–1242.

van Heerden, C., Nobel, P., & van Krevelen, D. W. (1951). Studies on fluidization. II—heat transfer. *Chemical Engineering Science*, 1(2), 51–66.

Wadke, P. M., Hounslow, M. J., & Salman, A. D. (2005). The 'smart' sphere: Experimental results. *Chemical Engineering Research and Design*, 83(11 A), 1298–1302.

Wen, C. Y., & Yu, Y. H. (1966). A generalized method for predicting the minimum fluidization velocity. *AIChE Journal*, 12(3), 610–612.

Williams, T. L. (2009). *Thermal Imaging Cameras: characteristics and performance*. London: Taylor & Francis.

Wong, A. K. C., & Sahoo, P. K. (1989). A gray-level threshold selection method based on maximum entropy principle. *IEEE Transactions on Systems, Man, and Cybernetics*, 19(4), 866–871.

Yanowitz, S. D., & Bruckstein, A. M. (1989). A new method for image segmentation. *Computer Vision, Graphics, and Image Processing*, 46(1), 82–95.

Yow, H. N., Pitt, M. J., & Salman, A. . (2005). Drag correlations for particles of regular shape. *Advanced Powder Technology*, 16(4), 363–372.

Zhou, Z. Y., Kuang, S. B., Chu, K. W., & Yu, a. B. (2010). Discrete particle simulation of particle–fluid flow: model formulations and their applicability. *Journal of Fluid Mechanics*, 661, 482–510.

11 Appendix

11.1 Monitoring particles from the top

11.1.1 Experimental setup and with binder sprayed

In this experiment, 1.6 kg small particles (calcium carbonate with diameter between 150-180µm) were used with liquid (PEG1000) sprayed. The inlet airflow rate from the bottom was 0.05 m³/s (about 7 times of the minimum flow rate), 25°C. Sprayed binder was 40°C. Window 2 and window 3 are used for monitoring. For window 3, thermal camera can be placed horizontally or with an angle, while for window 2, thermal camera can only be placed with an angle for focusing on particles (Figure 90).
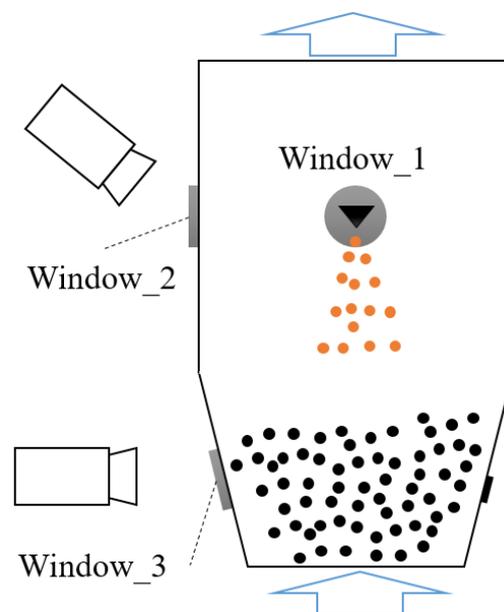
Figure 90: Thermal camera set-up

When a thermal camera was placed horizontally to monitor particles via window 3, before binder was sprayed and particles were stuck to the window, particulate flow can be observed. Figure 91 is an image captured by thermal camera with 50fps before binder was sprayed. In the figure, white background represents the steel wall and black objects are particles. It can be observed that particulate flow is clearly but individual particles cannot be distinguished by the thermal camera. After several minute particles were stuck to the window and nothing can be distinguished from the captured images. Form the experiment, it is also found that sprayed binder can accelerate the adhesion.

Figure 91: Monitor particles via window 3

When the position of thermal camera was changed from window 3 to window 2, before binder was sprayed and particles were stuck on the window, nothing can be distinguished from the captured images as shown in Figure 92, which is an image captured by thermal camera with 50fps. However, when binder was sprayed, particles with higher temperature can be observed, which is caused by contacting with binder droplets as shown in Figure 93.
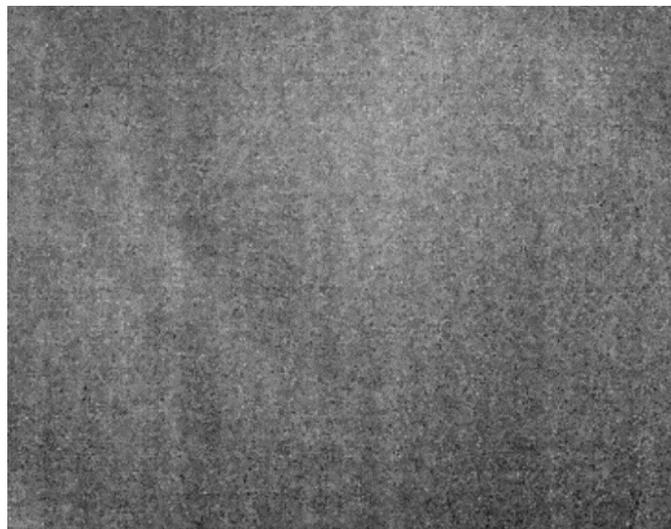
Figure 92: Monitor particles via window 2, before binder was sprayed.
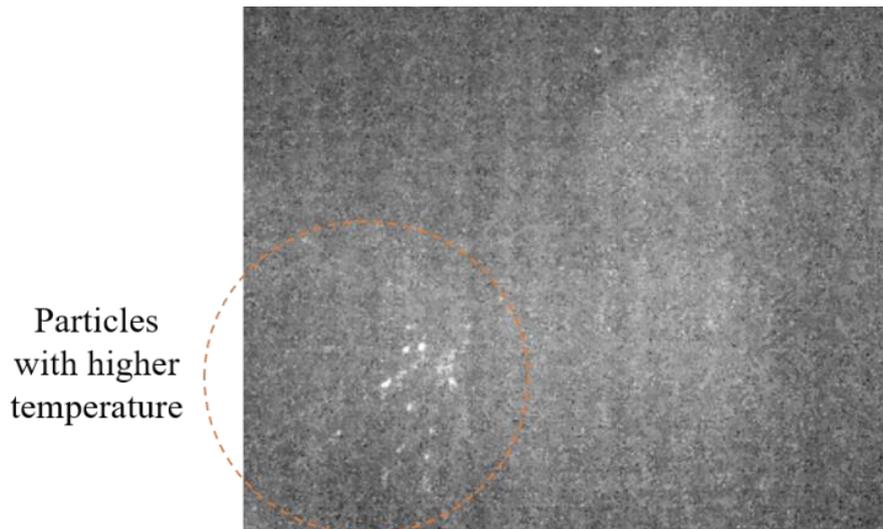
Figure 93: Monitor particles via window 2, after binder was sprayed.

After the binder was sprayed for several minutes, it was found that binder droplets stuck on the window was solidified and nothing can be distinguished from the captured images. Form this experiment, it is found that the particles and droplets prefer to stick on the window 3 rather than window 2. Therefore, window 2 is more suitable for monitoring. Since window 2 is chosen, while the particulate flow cannot be distinguished from the captured image Figure 92. It is necessary to investigate the viability to use temperature capture via window 2 to indicate particle temperature first.

11.1.2 Particles without liquid sprayed

In this monitoring, 1.6kg small particles (calcium carbonate, 150-180μm) were fluidized for 1h in advance to perform a stable condition at 30ºC and 40ºC inlet air temperature separately. The air flow rate used was 0.05m^3/s (about 7 times of the minimum flow rate). Temperatures of air at position b and c were measured by thermocouple probes every 5min. Temperature of particles was measured by thermal camera. Another two experiments without particles were conducted as well. The experiment set-up are shown in Figure 94.
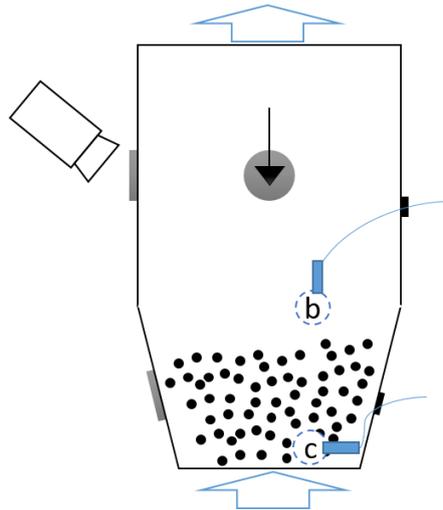
Figure 94: Monitor the temperature of air and particles without water sprayed

In Figure 95 and Figure 96, average temperature of particles was measured by thermal camera, while temperature air were measured by thermocouple probes. From Figure 95 and Figure 94, it is found that air temperature at position c was always higher than the air temperature at position b and the effect of particles can be neglected. It can also be observed that, the temperature difference between air and particles were smaller with lower inlet air temperature (Figure 95) than with higher inlet air temperature (Figure 96).

From this experiment, it is confirmed that reveal the effect of binder viscosity by air temperature only is not accurate, especially when the air temperature was measured off-line.
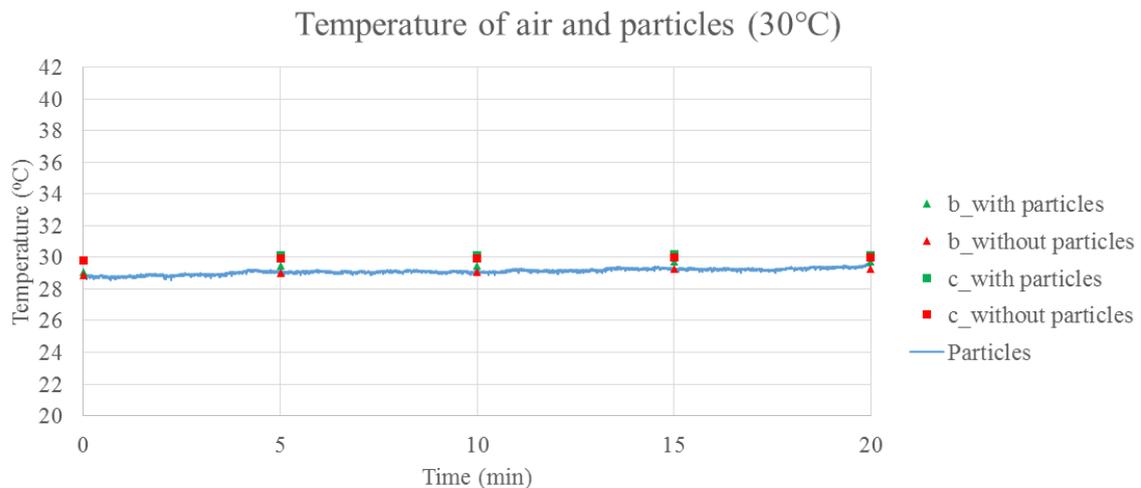
Figure 95: Temperature of air and particles at low temperature condition (30°C).

136
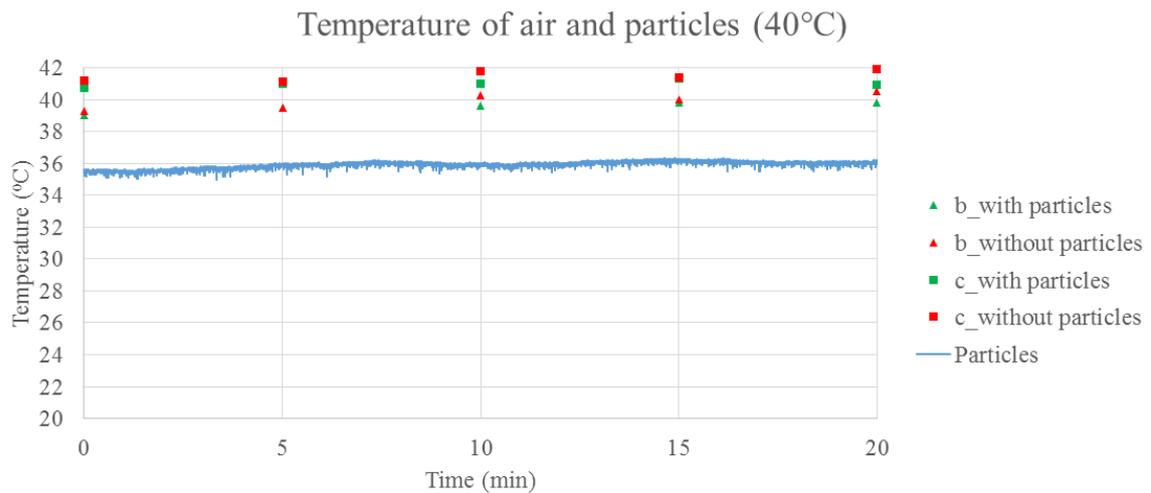
Figure 96: Temperature of air and particles at high temperature condition (40°C).

11.1.3 Particles with water sprayed

In this monitoring, 1.6 kg small particles (calcium carbonate, 150-180µm) were fluidized for 1h in advance to perform a stable condition. Air flow rate from the bottom was $0.05m^3$/s (about 7 times of the minimum flow rate) and 45°C. The experiment set-up is shown in Figure 97. Water (25°C) was sprayed from 0min and stopped at 2min. The air temperature at position a and b were measured by thermocouple probes every 2min. Two experiments were conducted with different water spray rate, the water spray rate of group_1 was 1g/min spray rate, while the water spray rate of group_2 was 3g/min spray rate. The average temperature of particles was measured by thermal camera.
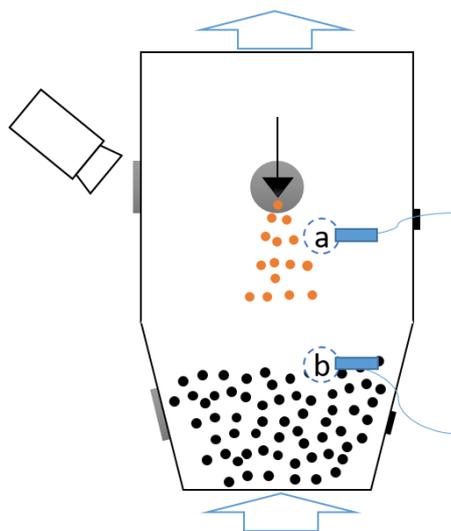
Figure 97: Monitor the temperature of small particles with water sprayed.

This monitoring was conducted three times. The results are shown in Figure 98. In this figure, "Group_1 Particles" and "Group_2 Particles" are the average temperature of particles in two experiments. "Group_1 air at Position a" is the temperature of air at position a. "Group_1 air at Position b" is the temperature of air at position b. "Group_2 air at Position a" is the temperature of air at position a. "Group_2 air at Position b" is the temperature of air at position b. From the figure, it is observed that higher spray rate (group_2, 3g/min) was associated with higher temperature decrease of air and particles. It can also be observed that, with same spray rate, the temperature of air at position a and b were both lower than particles.

It is therefore, concluded that:

- Thermal camera can distinguish the temperature difference of particles caused by different spray rate;
- Compared with particles, air temperature is easier to be affected by sprayed liquid.
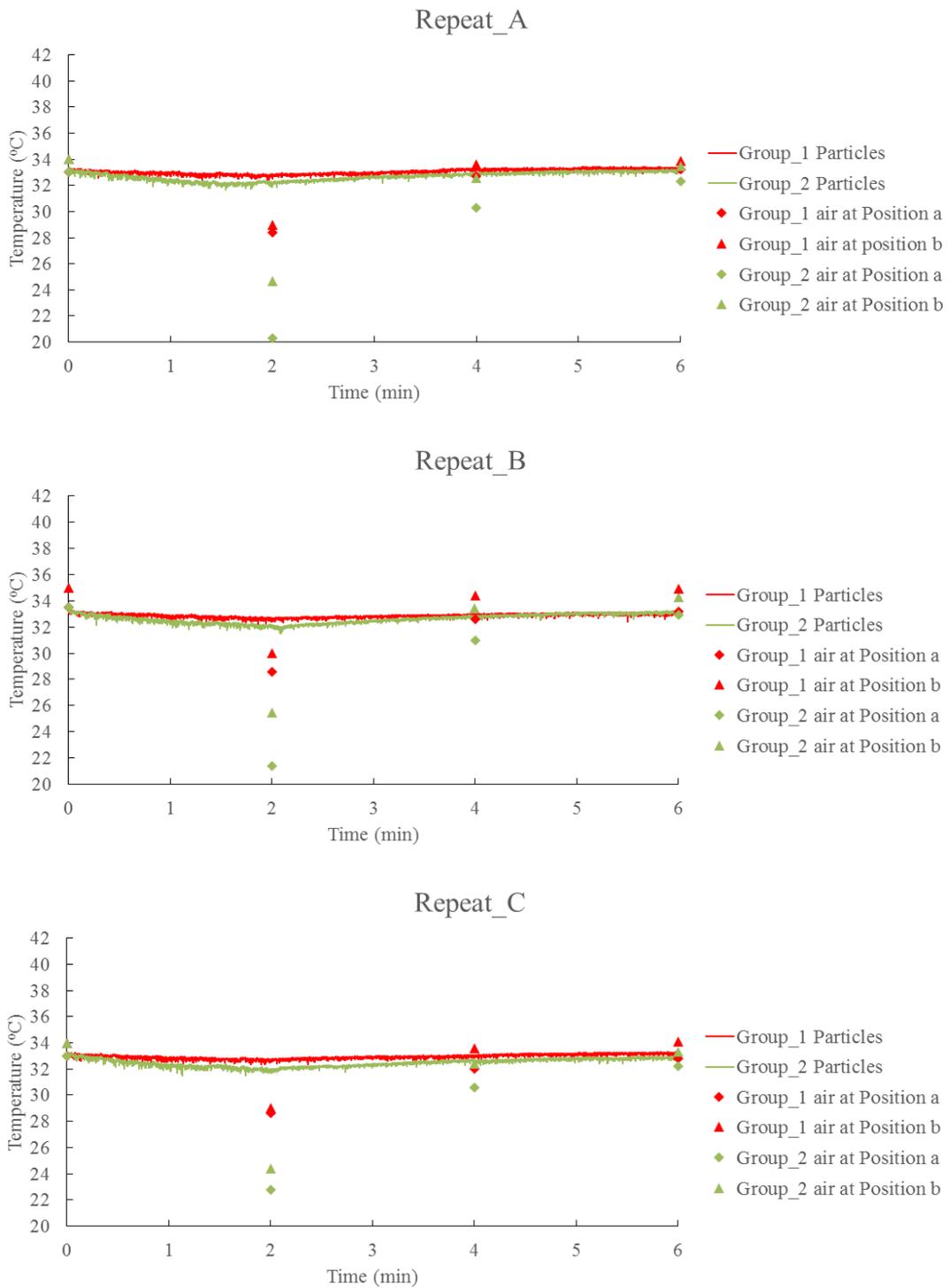
Figure 98. Temperature of particles and air with different water spray rate

11.1.4 Monitoring large particles with water sprayed

In this monitoring, 400g large particles (glass beads, 1.0-1.2mm) were fluidized for 1h
in advance to perform a stable condition. In order to monitor the contact between

particles and water droplets, particles were set to be moving in low velocity and fluidized bed was not fully fluidized, air flow rate from the bottom was $0.02m^3/s$ (about 0.25 times of the minimum flow rate) and 25°C. The experiment set-up is shown in Figure 99. Water (25°C) was sprayed from 2min. Two experiments were conducted, the spray rate of water were 1g/min and 3g/min separately. Air injected from the bottom was $0.02m^3/s$ and 25°C. The frame rate used by thermal camera was 100fps.
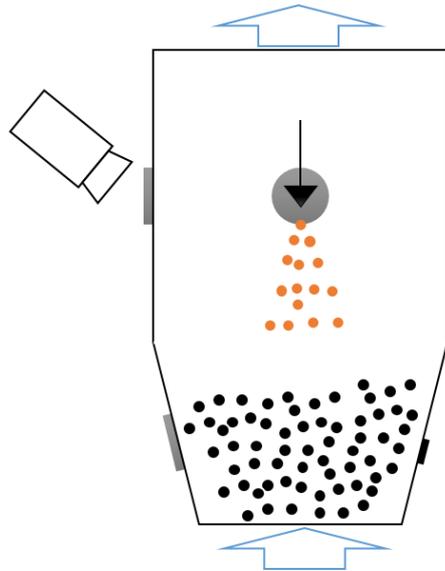
Figure 99. Monitor the temperature of large particles with water sprayed.

The captured images at 0min, 1min, 2min, 3min, 4min and 5min with two spray rates are shown in Figure 100. From the figure, it can be observed that, before water was sprayed (0min, 1min and 2min), nothing can be distinguished from the captured images, since the temperature between different objects in the images are similar. After water was sprayed (3min, 4min and 5min), the temperature of objects (including a thermocouple probe and large particles) contacted with water droplets were decreased more, which make them distinguishable by a thermal camera. It can also be observed that, lower spray rate generated more contacts between particles and droplets than higher spray rate (by comparing the number of black spots at 3min, 4min and 5min).

It is therefore concluded that when applying a thermal camera to monitor granulation process, number of contacts between particles and droplets can be distinguished.
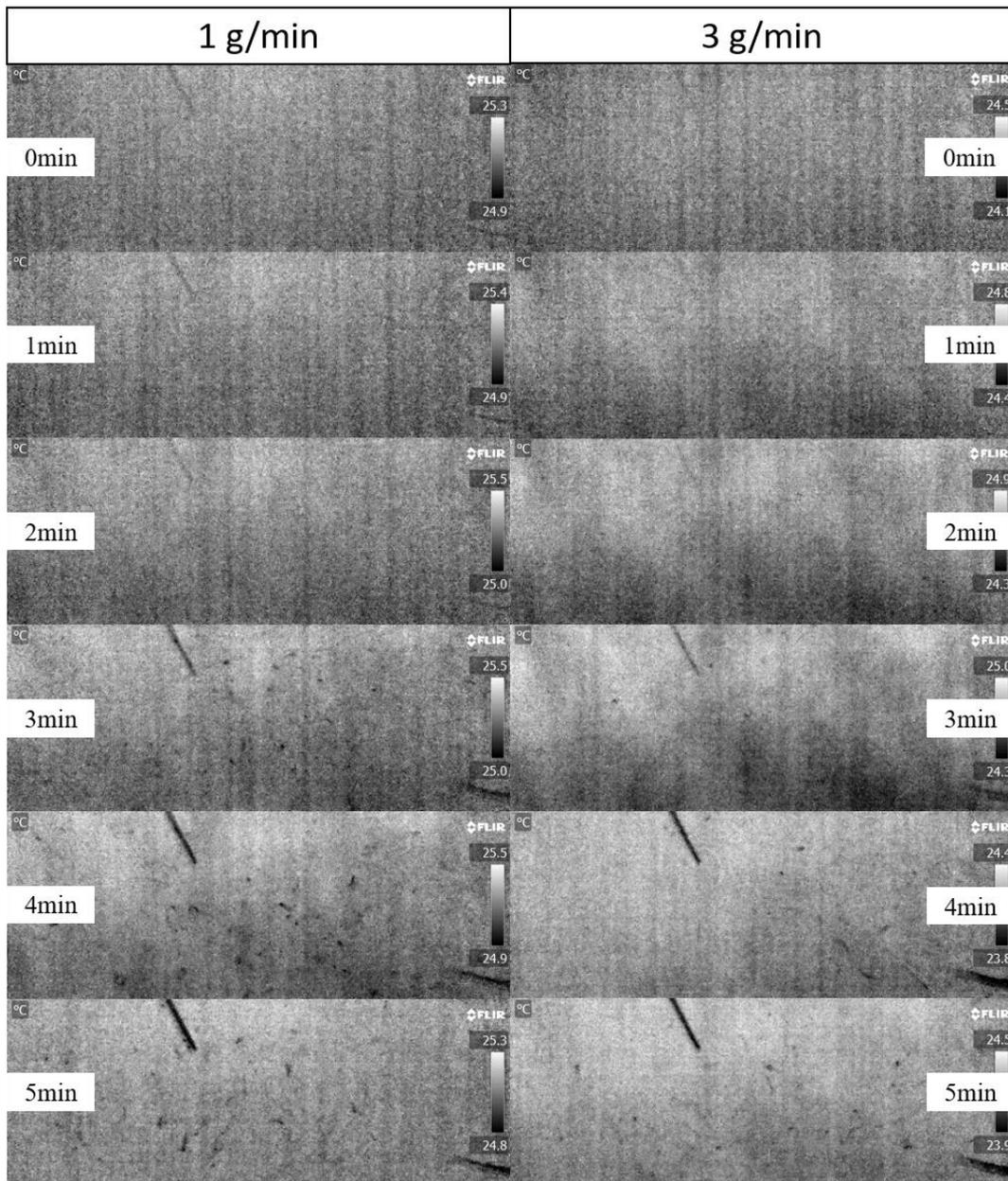
Figure 100. Comparison of the contact between particles and droplets with two different spray rates.

11.2 CFD-DEM modelling

In terms of modelling the particle heating process, continuum and discrete models are applicable. Continuum models treat moving solid phase as a "fluid", while discrete models treat moving solid phase as individual particles. In terms of modelling gas phase, computational fluid dynamics models are generally used, which analyse fluid based on finite meshed cells. In terms of modelling granule growth, population balance models are widely used, which considers the change of granule size distribution during granulation.

The advantages of modelling fluidized bed granulator with CFD-DEM (computational fluid dynamics – discrete element method) model are: the collision between individual particles can be considered, the temperature of individual particles can be calculated.

There are three basic models for DEM considering particle collision: soft-sphere model, hard-sphere model and hybrid of soft and hard sphere model. Hard-sphere model treats individual particles as rigid body and the collision only occurs instantaneously between two particles, while soft-sphere model treats individual particles as deformable body and more than two particles can be contacted at the same time. The hybrid model treats individual particles as deformable body but the collision limited to two particles only. Since in granulation, more than two particles are agglomerated, soft-sphere model is more suitable.

Soft-sphere model was originally proposed by Cundall & Strack (1979). In normal direction, they used "spring" to describe the elastic repulsion force and "dashpot" to describe the energy dissipation. In tangential direction, "spring" and "dashpot" were used to represent the static friction and "frictional slider" was used to represents the dynamic friction. In calculation, a definition "overlap", which indicates the intensity of the contact between two particles is first introduced.

By assuming particles i and j in contact are still spheres, the force acting on the particle i causing deformation when contacting with another particle can be written as (Kloss, Goniva, Hager, Amberger, & Pirker, 2012):

$$
\begin{aligned}
\vec{F} &= \left(\text{Normal elastic force}\overrightarrow{f_{cn,ij}} - \text{Normal damping force}\overrightarrow{f_{dn,ij}}\right) + \\
&\quad \left(\text{Tangential elastic force}\overrightarrow{f_{ct,ij}} - \text{Tangential damping force}\overrightarrow{f_{dt,ij}}\right) \\
&= \left(k_n\delta_n\vec{n} - \gamma_n\overrightarrow{v_{n,ij}}\right) + \left(k_t\vec{\delta_t} - \gamma_t\overrightarrow{v_{t,ij}}\right)
\end{aligned} \tag{95}
$$

$$
k_n = \tfrac{4}{3}Y^*\sqrt{R^*\delta_n}: \qquad \text{Elastic constant for normal contact} \tag{96}
$$

Effective Young's modulus: $Y^* = \left(\dfrac{(1-v_i^2)}{Y_i} + \dfrac{(1-v_j^2)}{Y_j}\right)^{-1}$ (97)

Y: Young's modulus (Pa). v: Poisson ratio.

Effective Radius: $R^* = \left(\dfrac{1}{R_i} + \dfrac{1}{R_j}\right)^{-1}$ (98)

R: particle radius (m)

$\delta_n = d - \left(R_i + R_j\right)$:   Overlap distance of two spherical particles (99)

d is the distance between the centre of two particles (m).

$\vec{n}$: Unit vector from particle i to particle j.

$$\gamma_n = -2\sqrt{\frac{5}{6}}\beta\sqrt{S_n m^*} \geq 0: \quad \text{Viscoelastic damping constant for normal} \tag{100}$$

contact

Constant: $\beta = \frac{\ln(e)}{\sqrt{\ln^2(e)+\pi^2}}$ (101)

e: Coefficient of restitution.

$$S_n = 2Y^*\sqrt{R^*\delta_n} \tag{102}$$

$\overrightarrow{v_{n,ij}}$: Normal component of the relative velocity of the two particles (m/s).

$$k_t = 8G^*\sqrt{R^*\delta_n} \qquad \text{Elastic constant for tangential contact} \tag{103}$$

Effective shear modulus: $G^* = \left(\frac{2(2-v_i)(1+v_i)}{Y_i} + \frac{2(2-v_j)(1+v_j)}{Y_j}\right)^{-1}$ (104)

$\overrightarrow{\delta_t}$: Tangential displacement vector between two spherical particles which is truncated to satisfy a frictional yield criterion.

$$\gamma_t = -2\sqrt{\frac{5}{6}}\beta\sqrt{S_t m^*} \geq 0 \qquad \text{Viscoelastic damping constant for} \tag{105}$$

tangential contact

$$S_t = 8G^*\sqrt{R^*\delta_n} \tag{106}$$

Effective mass: $m^* = \left(\frac{1}{m_i} + \frac{1}{m_j}\right)^{-1}$ (107)

m: particle mass (kg)

$\overrightarrow{v_{t,ij}}$: Tangential component of the relative velocity of the two particles (m/s)

When$(|\overrightarrow{\delta_t}| \geq \delta_{t,max})$ (Zhou, Kuang, Chu, & Yu, 2010), $\overrightarrow{f_{ct,ij}} - \overrightarrow{f_{dt,ij}}$ should be replaced by $\overrightarrow{f_{t,ij}}$

Coulomb friction force:

$$\overrightarrow{f_{t,ij}} = -\mu_s|\overrightarrow{f_{cn,ij}}|\widehat{\delta_t}, \text{ where } \widehat{\delta_t} = \overrightarrow{\delta_t}/|\overrightarrow{\delta_t}|, \delta_{t,max} = \mu_s((2-v)/2(1-v))\delta_n \tag{108}$$

μ_s: Particle-particle/wall sliding friction.

Rolling friction torque:

$$\overrightarrow{M_{r,ij}} = \mu_r|\overrightarrow{f_{n,ij}}|\widehat{\omega_{ij}}^n, \text{ where } \widehat{\omega_{ij}}^n = \overrightarrow{\omega_{ij}^n}/|\overrightarrow{\omega_{ij}^n}| \tag{109}$$

Where $\overrightarrow{f_{n,ij}}$ is the normal force between two particles (N), μ_r is the Particle-particle/wall rolling friction, $\overrightarrow{\omega_{ij}^n}$ is the relative angular velocity between two particles (rad/s).

Torque by tangential forces:

$$\overrightarrow{M_{t,ij}} = \overrightarrow{R_{ij}} \times \left(\overrightarrow{f_{ct,ij}} + \overrightarrow{f_{dt,ij}}\right) \tag{110}$$

$$\overrightarrow{v_{ij}} = \overrightarrow{v_j} - \overrightarrow{v_i} + \overrightarrow{\omega_j} \times \overrightarrow{R_j} - \overrightarrow{\omega_i} \times \overrightarrow{R_i}, \overrightarrow{v_{n,ij}} = \left(\overrightarrow{v_{ij}} \cdot \vec{n}\right) \cdot \vec{n}, \overrightarrow{v_{t,ij}} = \left(\overrightarrow{v_{ij}} \times \vec{n}\right) \times \vec{n} \tag{111}$$

In terms of describing gas phase only, volume-averaged conservation equations for mass and momentum can be used and written as (A. V. Patil, Peters, & Kuipers, 2015b):

$$\frac{\partial}{\partial t}\left(\varepsilon\rho_g\right) + \nabla \cdot \left(\varepsilon\rho_g\overrightarrow{u_g}\right) = 0 \tag{112}$$

$$\frac{\partial}{\partial t}\left(\varepsilon\rho_g\overrightarrow{u_g}\right) + \nabla \cdot \left(\varepsilon\rho_g\overrightarrow{u_g}\overrightarrow{u_g}\right) = -\varepsilon\nabla p - \nabla \cdot \left(\varepsilon\vec{\tau}_g\right) + \vec{S}_p + \varepsilon\rho_g\vec{g} \tag{113}$$

Where t is the time (s), ε is the gas volume fraction, ρ_g is gas density (kg/m^3), $\overrightarrow{u_g}$ is the gas velocity (m/s), p is the gas pressure (Pa), $\vec{S}_p$ represents the source term for momentum originating from the particle phase.

When a particle is moving in gas phase, three types of forces are exerted on it: steady state drag force, unsteady state force and body force. Steady state drag force represents the force caused by different velocity between the particle and fluid. Unsteady state force containing virtual mass force and basset force, represents the force caused by the acceleration of particle with respect to fluid. There are three terms in body force, pressure gradient force is caused by the pressure of fluid exerted on the particle, shear force is caused by the viscosity of fluid and gravitational force is caused by the gravity. With respect to the forces, coupling of CFD and DEM are basically classified as three types: one-way (forces on fluid), one-way (forces on particles) and two-way (forces on both fluid and particles). Since in fluidized bed granulation, the effects of fluid on particles and particles on fluid are both important, two-way coupling method is more suitable.

In uniform fluid, drag force exerted on a particle is $\overrightarrow{f_{d,\iota}}$
= steady state drag force + unsteady state forces + Body force
= steady state drag force + (virtual mass force + Basset force) + (Pressure gradient force + shear force+ gravitational force)

Steady state drag force: $\overrightarrow{F_D} = C_D\frac{1}{2}\rho_p(\vec{u} - \vec{v})|\vec{u} - \vec{v}|\pi R^2 \tag{114}$

Where ρ_p is the particle density (kg/m^3), $\vec{u}$ is the velocity of fluid and $\vec{v}$ is the velocity of particle (m/s).

Particle Reynolds number $Re_r = \frac{\rho_p D|\vec{u}-\vec{v}|}{\mu} \tag{115}$

Where D is the diameter of the particle (m), ρ_p is the particle density (kg/m^3) and μ is the fluid viscosity $(Pa \cdot s)$.

Drag coefficient C_D are varied with different Re_r in different models. Normally virtual mass force and Basset force are neglected.

Pressure gradient force: $\overrightarrow{F_p} = -\int_{cv} \overrightarrow{\nabla p}dV \tag{116}$

Where p is the gas pressure (Pa) surrounding the particle and V is the particle volume (m^3).

Shear force: $\overrightarrow{F_\tau} = \int_{cs} \overrightarrow{\nabla \tau}dV \tag{117}$

$$\tau = \mu_g[(\nabla\vec{u}) + (\nabla\vec{u})^{-1}] \tag{118}$$

Where μ_g is the viscosity of the fluid $(Pa \cdot s)$

Gravitational force: $\overrightarrow{\boldsymbol{F_g}} = m\overrightarrow{\boldsymbol{g}}$ (119)

Where m is the mass of the particle (kg) and $\overrightarrow{\boldsymbol{g}}$ is the gravitational acceleration with direction (m/s^2).

In order to build a CFD-DEM to describe the granulation within a FBG, a soft-sphere model for DEM and two-way coupled with laminar model for CFD was initially built. The software used to simulate the model were LIGGGHTS (Kloss et al., 2012) for DEM, OpenFOAM (OpenFOAM, 2014) for CFD and CFDEM-Coupling (Kloss et al., 2012) for coupling between LIGGGTS and OpenFOAM. The parameters used in Table 2 are referenced from the model used by Zhou et al. (2010), The distance, in which forces between particles are calculated, was 1mm. Time step used by CFD and DEM were both 1.0×10^5s.

Table 2 Parameters for the CFD-DEM model

Number of particles	15000
Particle diameter	4mm
Particle density	2500kg/m^3
Particle-particle/wall sliding friction	0.4
Particle-particle/wall rolling friction	0.04
Particle-particle/wall restitution coefficient	0.3
Particle Young's modulus	1.0×10^7 Pa
Particle Poisson ratio	0.3
Gas density	1.2kg/m-3
Gas viscosity	1.8×10^{-5}Pa·s

In this model, the geometry of the fluidized bed used was similar to it is in reality but without the distributor at the bottom. The generated mesh cells were fixed cube with 0.01m in edge. Flow rate used was 0.10m^3/s, 0.08m^3/s and 0.06m^3/s separately.
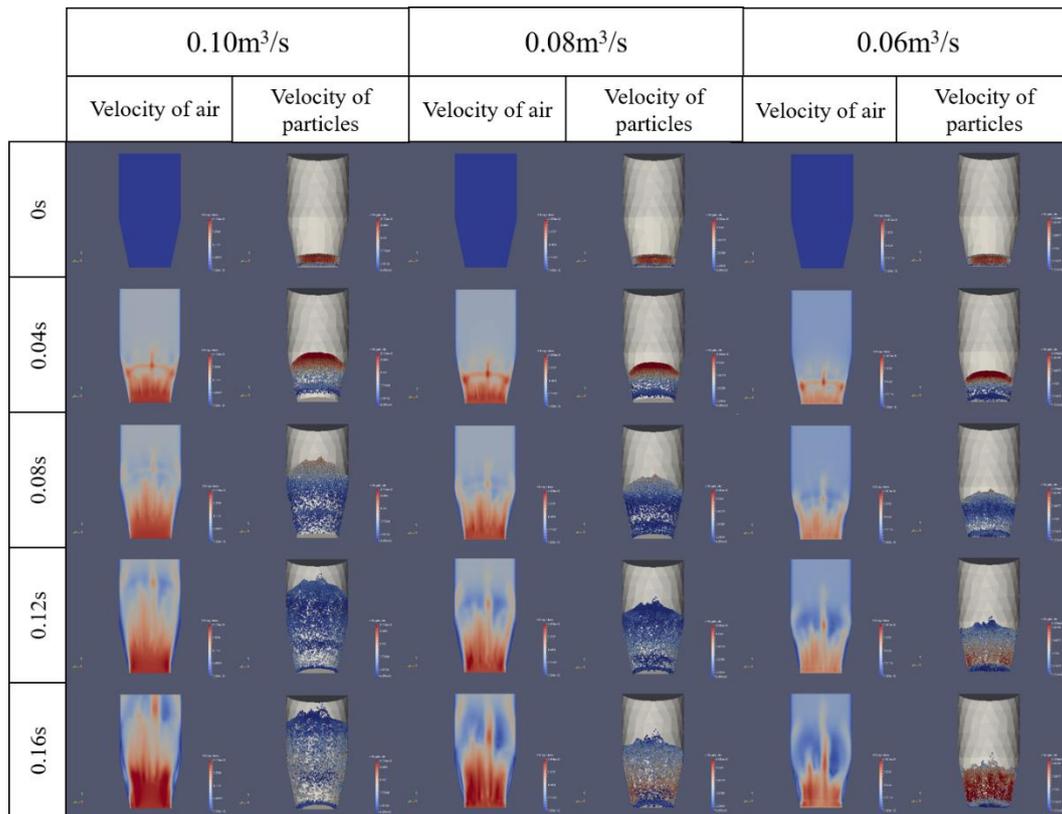
Figure 101. CFD-DEM Simulation of fluidized bed (future work).

From the results in Figure 101, the effect of air flow rate on the movement of particles can be observed. It is found that higher air flow rate is associated with longer circulation interval and higher bed height. It is also found that at the bottom of the fluidized bed, there is an air layer preventing particles falling down. However, in reality, there is an air distributor at the bottom, which can minimise the formation of the air layer. It is therefore, concluded that the air distributor needs to be built in the fluidized bed geometry to perform an accurate simulation.

11.3 Temperature distributions of the particles at steady state

In the experiment introduced in the section 7.1, temperature distribution of the particles can also be obtained. However, limited by the image segmentation technique and the specification of the thermal camera, the temperature distribution is not accurate enough to be used.

In order to compare the particle temperature, the air temperature and the fluidized bed

wall temperature, $\theta = \frac{T_p - T_w}{T_a - T_w}$ was used to present the results. The results are shown in

Figure 102, Figure 103, and Figure 104.

Figure 102 shows the distribution of the θ for 1000 g particles.
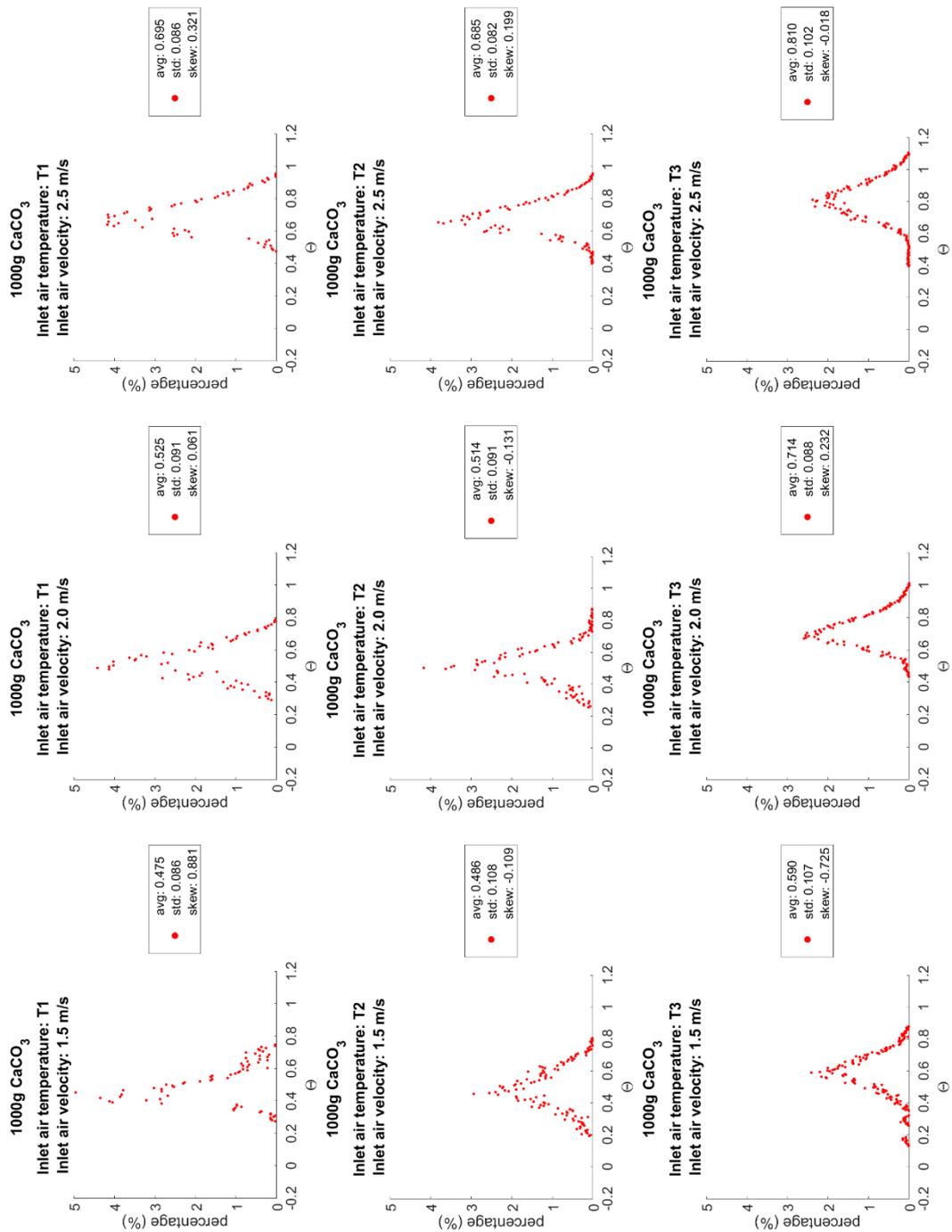
Figure 102. Distribution of the θ for 1000 g particles.

Figure 103 shows the distribution of the θ for 1200 g particles.
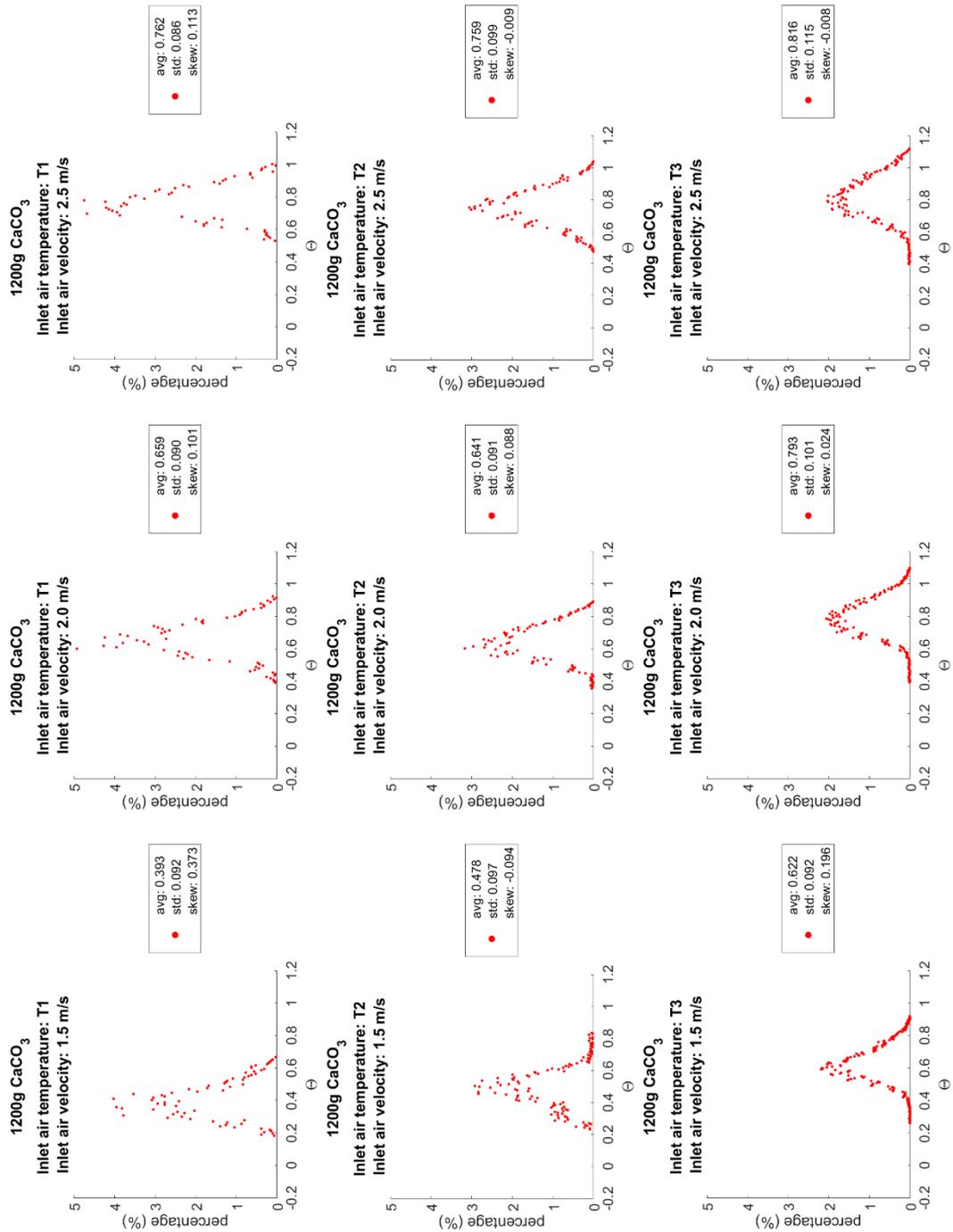
Figure 103. Distribution of the θ for 1200 g particles.

Figure 104 shows the distribution of the θ for 1400 g particles.
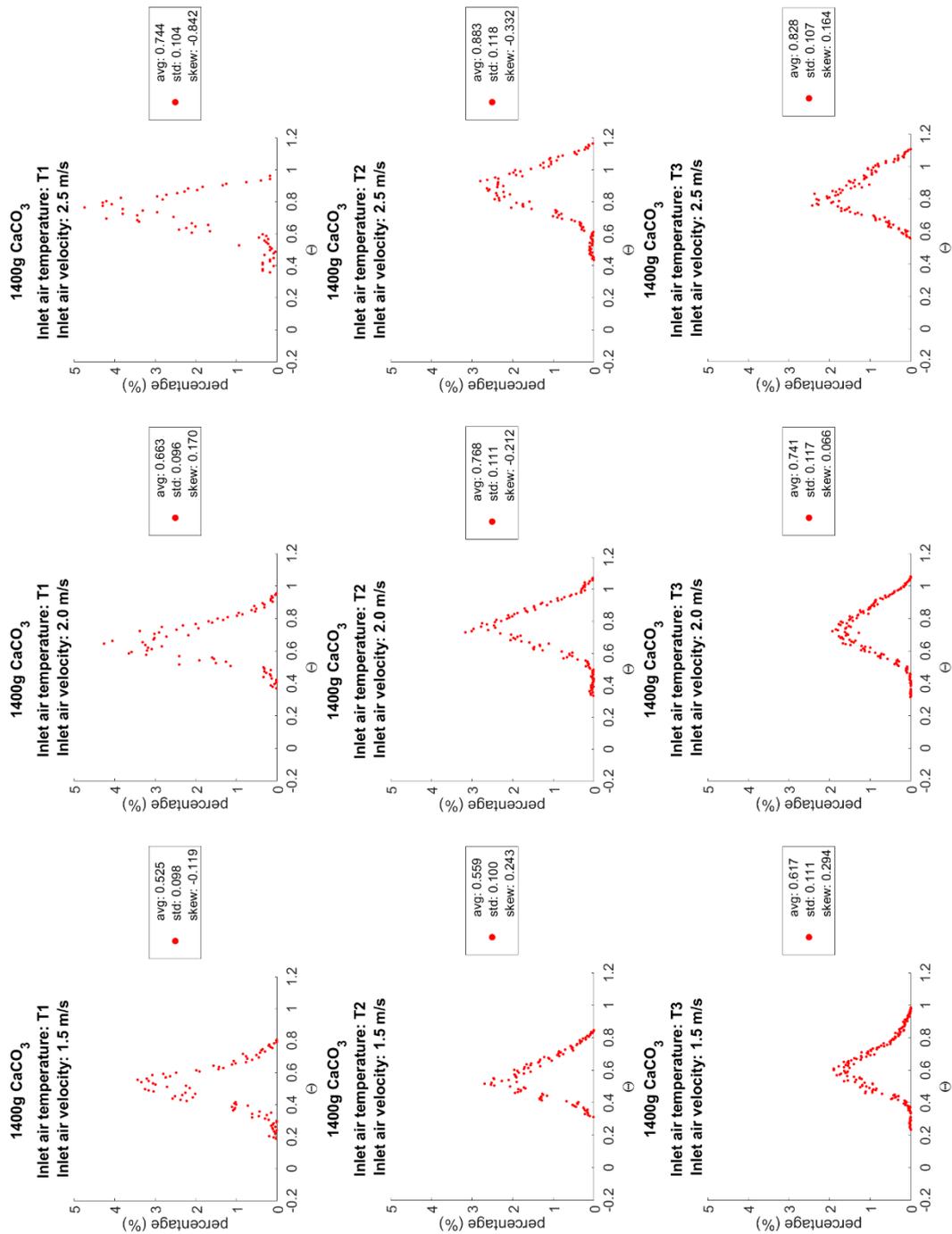
Figure 104. Distribution of the θ for 1400 g particles.